NOVEL SCANNING PROBE MICROSCOPE INSTRUMENTATION WITH APPLICATIONS IN NANOTECHNOLOGY

by

Martin James Humphry B.Sc.

Thesis submitted to the University of Nottingham for the degree of Doctor of Philosophy,

October 2000

Contents

Abstract

A versatile scanning probe microscope controller has been constructed. Its suitability for the control of a range of different scanning probe microscope heads has been demonstrated. These include an ultra high vacuum scanning tunnelling microscope, with which atomic resolution images of Si surfaces was obtained, a custom-built atomic force microscope, and a custom-built photon emission scanning tunnelling microscope. The controller has been designed specifically to facilitate data acquisition during molecular manipulation experiments.

Using the controller, the fullerene molecule C_{60} has been successfully manipulated on Si(100)-2x1 surfaces and detailed data has been acquired during the manipulation process. Evidence for two distinct modes of manipulation have been observed. A repulsive mode with success rates up to 90% was found to occur with tunnel gap impedances below 2GΩ, while between 2GΩ and 8GΩ attractive manipulation events were observed, with a maximum success rate of ~8%. It was also found that the step size between feedback updates had a significant effect on tip stability, and that dwell time of the STM tip at each data point had a critical effect on manipulation probability.

A multi-function scanning probe microscope head has been developed capable of operation as a scanning tunnelling microscope and an atomic force microscope in vacuum and a magnetic field of 7T. The custom-built controller also presented here was used to control the head. A three-axis inertial sliding motor was developed for the head, capable of reproducible step sizes of <1000Å. In addition, an optical fibre interferometer was constructed with a sensitivity of $0.2\,\text{Å}/\sqrt{Hz}$. Preliminary development of a magnetic resonance force microscope mode has also been performed, with initial results showing such a system to be feasible.

Acknowledgements

I would like to thank my supervisor Prof. Peter Beton for his patience and help throughout my studies, and my co-supervisor Prof. Richard Bowtell for his helpful input. I would also like to thank Dr. Philip Moriarty for his endless enthusiasm for physics and Dr. Michael Hunt for his excellent physical insights and intelligent conversation. I am also grateful to EPSRC and Oxford Instruments for funding me throughout my research.

Thanks must go to my friends and colleagues, past and present, within the physics department – Andy, Martin, Ron, Brad, Matt, Mike, John, and Dave, who have helped make my life more entertaining. Last but not least, I would like to thank Nicola for always being there for me, and my family – Mum, Dad, and Jilly, for their continuous support and encouragement.

Chapter 1
Introduction

In this chapter the principles of various scanning probe microscopes are presented. Particular attention is paid to scanning tunnelling microscopy and scanning force microscopy. Future directions of scanning probe microscopy are also discussed with respect to applications in nanotechnology.

1.1 Scanning Tunnelling Microscopy

The scanning tunnelling microscope (STM) was the first to be developed in a range of closely related imaging techniques, collectively termed scanning probe microscopes (SPMs). In less than 20 years, they have revolutionised nanometre-scale measurement and analysis. This is mainly because they utilise highly localised interactions between a surface and probe, allowing the properties of single atoms and molecules to be investigated. Other surface analysis techniques generally probe large numbers of atoms (10^{10}-10^{11}) and so cannot provide the localised data produced by SPMs.

1.1.1 Tunnel junctions

The STM employs the principle of quantum mechanical tunnelling; If two conducting surfaces are positioned sufficiently close together it is possible for electrons to tunnel through the barrier between them. Figure 1.1 illustrates this for the case of an atomically sharp metal tip and a sample surface in vacuum. The wavefunctions of electrons in the tip and sample decay exponentially into the vacuum, so if the tip-sample separation is reduced to ~10Å, the two wavefunctions overlap. Consequently, if a small bias (typically 1mV-4V) is applied, electrons can tunnel through the barrier resulting in a current of typically 0.1-10nA.

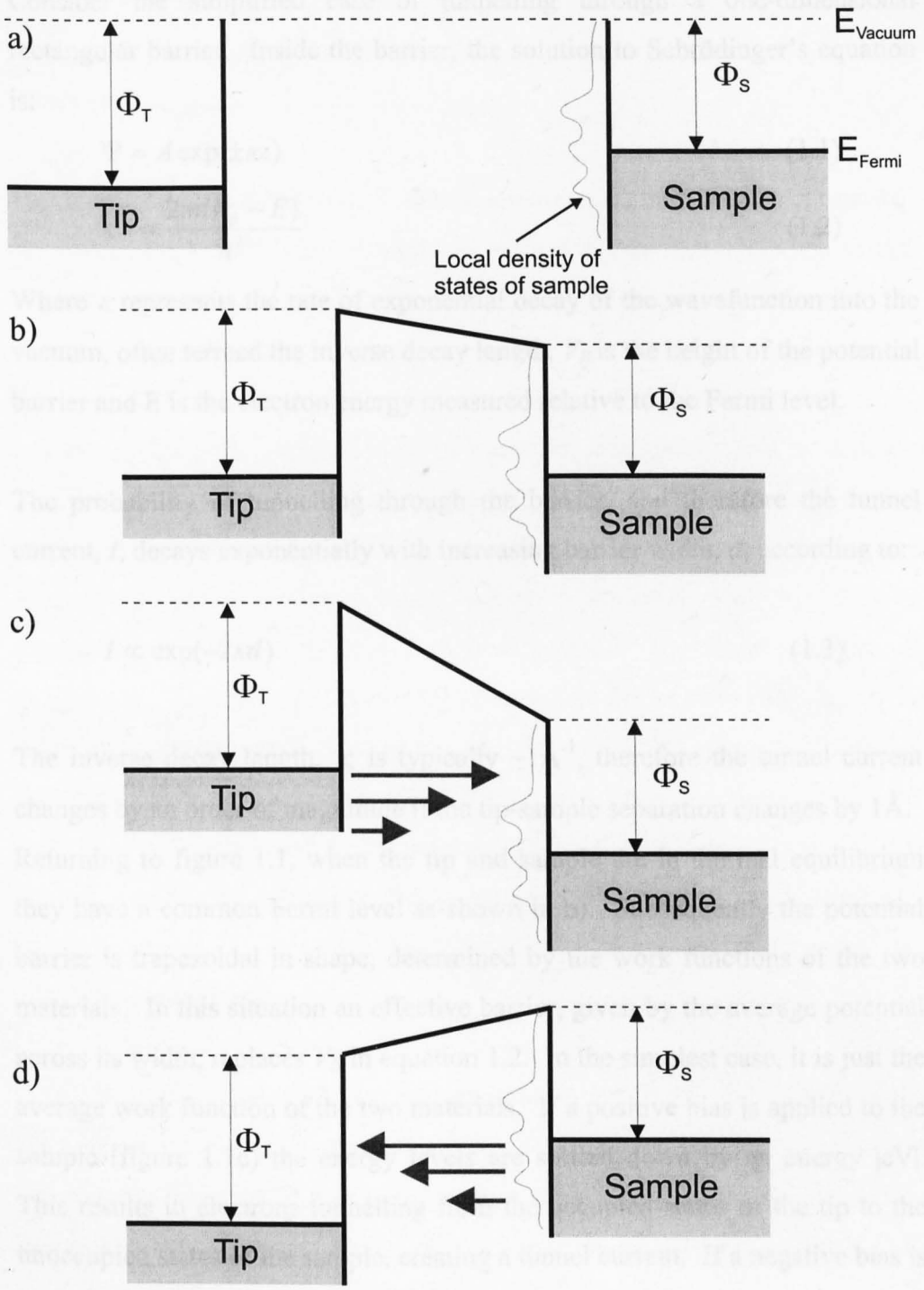

Figure 1.1 *Schematic diagrams of the tip-sample system. a) Non-interacting tip and sample. b) Tip and sample in thermal equilibrium. c) Positive sample bias d) Negative sample bias.* Φ_T *and* Φ_S *are the work functions of the tip and sample respectively. The arrows indicate the states involved in tunnelling.*

Consider the simplified case of tunnelling through a one-dimensional rectangular barrier. Inside the barrier, the solution to Schrödinger's equation is:

$$\Psi = A\exp(\pm\kappa z) \tag{1.1}$$

$$\kappa^2 = \frac{2m(V_B - E)}{\hbar^2} \tag{1.2}$$

Where κ represents the rate of exponential decay of the wavefunction into the vacuum, often termed the inverse decay length, V_B is the height of the potential barrier and E is the electron energy measured relative to the Fermi level.

The probability of tunnelling through the barrier, and therefore the tunnel current, I, decays exponentially with increasing barrier width, d, according to:

$$I \propto \exp(-2\kappa d) \tag{1.3}$$

The inverse decay length, κ, is typically $\sim 1\text{Å}^{-1}$, therefore the tunnel current changes by an order of magnitude if the tip-sample separation changes by 1Å. Returning to figure 1.1, when the tip and sample are in thermal equilibrium they have a common Fermi level as shown in b). Subsequently the potential barrier is trapezoidal in shape, determined by the work functions of the two materials. In this situation an effective barrier, given by the average potential across its width, replaces V_B in equation 1.2. In the simplest case, it is just the average work function of the two materials. If a positive bias is applied to the sample (figure 1.1c) the energy levels are shifted down by an energy |eV|. This results in electrons tunnelling from the occupied states of the tip to the unoccupied states of the sample, creating a tunnel current. If a negative bias is applied to the sample, the reverse occurs; the sample energy levels are shifted up by |eV|, and electrons tunnel from filled states in the *sample* to empty states in the tip.

1.1.2 Principles of STM

Binnig, Rohrer et al invented the scanning tunnelling microscope in 1982 [1,2], for which they were subsequently awarded the Nobel Prize for physics

in 1986. It utilises the exponential dependence of tunnelling probability with barrier width discussed in the previous section to produce an extremely sensitive local probe.

Figure 1.2 shows a schematic of STM operation. A sharp metal tip, typically W, Au or Pt/Ir alloy, is scanned across a surface by two piezoelectric elements aligned parallel to the surface (P_x and P_y). A third piezoelectric element, mounted perpendicular to the surface, controls the vertical position of the tip. A bias is applied to the sample relative to the tip, causing a tunnel current, I_T, to flow. In the most common mode of operation, constant current mode, the z height is adjusted by a feedback system to maintain a constant tunnel current while the tip is raster scanned over the surface. By recording the voltage applied to the z piezo, a "topographic" image is produced. However, for sub-nanometre scale images it is not necessarily a true representation of topography. Tersoff and Hamann [3] showed that for an ideal metallic tip the current at any position is actually proportional to the local density of states at the Fermi level. So a "topography" image is actually a convolution of the local density of states and the true topography of the surface. The situation is complicated further if the tip differs significantly from an ideal atomically sharp metal one. In this case, the local density of states of the tip can also affect the tunnel current.

It will be useful in later sections on molecular manipulation to be aware of the relationship between I, V and d, which are the tunnel current, sample bias and tip-sample separation respectively. Since $\kappa \sim 1 Å^{-1}$, a change in tunnel current of an order of magnitude results in a change in tip-sample separation of ~1Å. The effect of variations in V on the tip-sample separation is more complex, as the tunnel current is also related to the local density of states. As a rough approximation a uniform density of states would result in the tip-sample separation having a dependence of $V^{-1/2}$ on the sample bias.

An alternative mode of operation, termed constant height mode, employs a much slower feedback response, and a much faster scan rate. This results in

the tip height staying roughly constant during a scan. Instead of the z piezo voltage, the tunnel current is used to create an image.

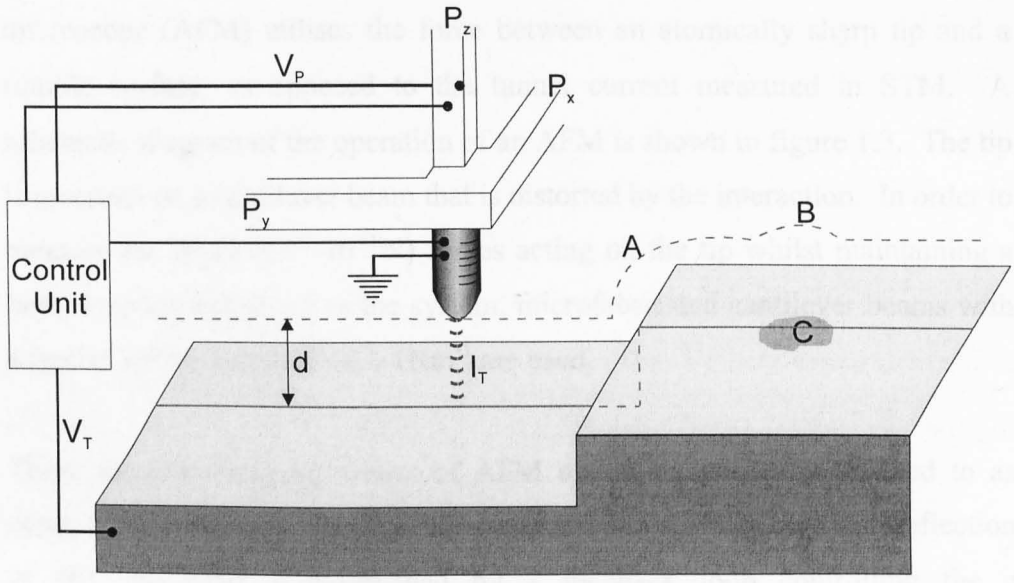

Figure 1.2 *Schematic of a STM. Piezoelectric elements P_x and P_y scan the metal tip over the surface. The control unit modulated the voltage applied the the z piezo to maintain a constant tunnel current, I_T, for a given sample bias V_T. Dashed red line indicates path of tip, whilst traversing a step edge (A), and a region with lower work function (B and C).*

1.2 Scanning Force Microscopy

While STM is capable of resolving individual atoms on conducting surfaces, it cannot be used on insulating surfaces. The related technique of scanning force microscopy (SFM) was developed to address this problem. It is now possible to image both conducting and non-conducting surfaces with SFM with a resolution approaching that of a STM. Utilising a range of different probes, SFM has become one of the most widely used SPM techniques, with applications as diverse as surface science and metallurgy to biology and biochemistry.

1.2.1 Atomic force microscopy

The atomic force microscope was the first SFM to be developed, by Binnig, Quate and Gerber in 1986 [4]. Similar in operation to STM, the atomic force microscope (AFM) utilises the force between an atomically sharp tip and a sample surface, as opposed to the tunnel current measured in STM. A schematic diagram of the operation of an AFM is shown in figure 1.3. The tip is mounted on a cantilever beam that is distorted by the interaction. In order to measure the small (10^{-6}-10^{-10}N) forces acting on the tip whilst maintaining a high resonant frequency of the system, microfabricated cantilever beams with a typical spring constant ~0.1-1Nm^{-1} are used.

There are two common modes of AFM operation, generally referred to as contact and non-contact modes. In contact mode AFM, a constant deflection of the cantilever is maintained by a feedback loop controlling the z piezoelectric element, similar to constant current STM operation. The cantilever is raster scanned across the surface, and the voltage applied to the z piezo is stored to form an image. The image represents a surface of constant force, which is generally repulsive in nature and caused by Coulombic interactions (i.e. the tip is in physical contact with the surface).

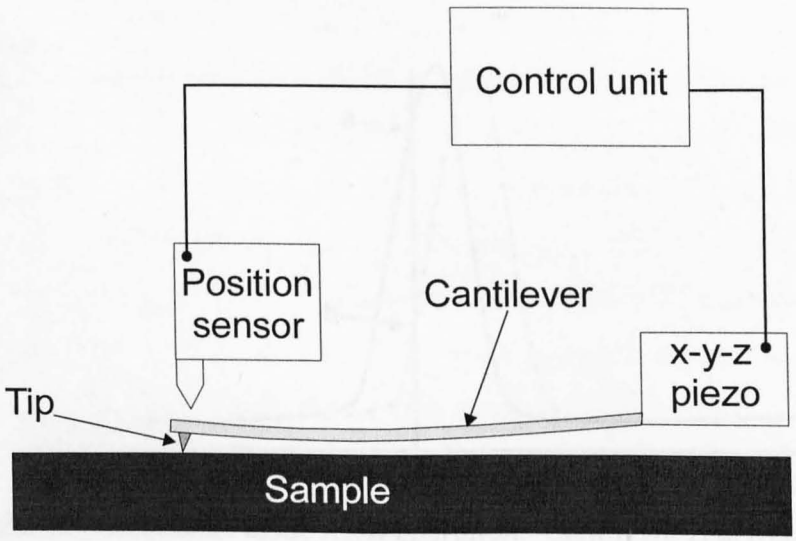

Figure 1.3 *Schematic diagram of an atomic force microscope. The tip is raster scanned over a surface while a constant deflection of the cantilever is maintained.*

In non-contact AFM force *gradients* are measured through changes in the resonant frequency of the cantilever. In this mode, the tip is positioned ~50Å from the surface, and driven into oscillation close to its natural resonant frequency. The presence of a force gradient modifies the effective spring constant of the cantilever, k_{eff}, according to:

$$k_{eff} = k_0 - F' \tag{1.4}$$

Where $F' = \delta F_z/\delta z$ is the force gradient and k_0 is the spring constant of the cantilever without the presence of F'. Since the resonant frequency, ω, is given by

$$\omega = \left(\frac{k_{eff}}{m}\right)^{1/2} = \omega_0\left(1 - \frac{F'}{k_0}\right)^{1/2} \tag{1.5}$$

where m is an effective mass and ω_0 is the natural resonant frequency, the cantilever resonance will consequently be shifted in frequency by the presence of a force gradient. If driven near to the cantilever natural resonant frequency, the presence of a force gradient will change the amplitude of oscillation, as shown in figure 1.4.

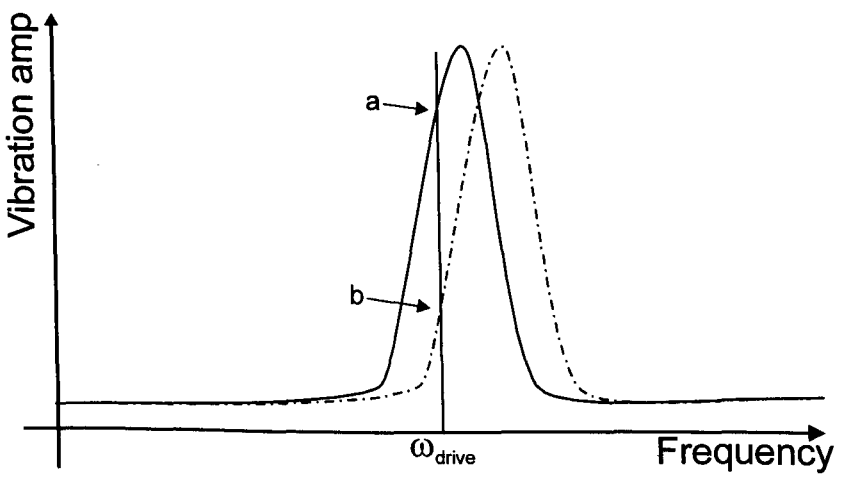

Figure 1.4 *Non contact mode AFM operation. Cantilever is driven at a frequency ω_{drive}. With no force gradient the cantilever oscillates with an amplitude marked by the letter "a". In the presence of a force gradient, the resonance peak shifts, resulting in a change in cantilever oscillation amplitude, marked "b".*

An image of constant force gradient can be obtained by raster scanning the tip across the surface whilst maintaining constant cantilever vibration amplitude with feedback loop control as for other modes. Using this method it is possible to record both the repulsive forces employed in contact mode and considerably weaker long-range attractive forces due to Van der Waals interactions.

Measurement of cantilever deflection was initially measured using a tunnelling sensor [4], however more recently optical techniques such as optical beam deflection [5] and optical interferometry [6,7, section 5.4] have superseded tunnelling. These techniques produce minimal effects on the cantilever at room temperature, whereas a tunnelling sensor can significantly modify the effective spring constant of the cantilever.

1.2.2 Other scanning force microscopes

Since the invention of the AFM, scanning force microscopy has expanded to include numerous other interaction forces, such as magnetic [8], electrostatic [9], frictional forces [10], and can in principle be adapted to measure virtually any force in the range 10^{-7}-10^{-10}N.

In magnetic force microscopy (MFM) a magnetic tip (e.g. Co, Fe or Ni), mounted on a microfabricated cantilever as in AFM, is located ~100-5000Å above a magnetic sample surface. Interactions between the stray magnetic fields from the sample and the tip exert a force on the cantilever. Operation in both constant deflection mode (similar to contact mode AFM) and non-contact mode are possible. A tip with sufficiently small magnetic domain at the apex can be approximated as a point dipole with total magnetic moment $\boldsymbol{m}$ [14] and the force on the cantilever is given by:

$$\mathbf{F} = (\boldsymbol{m} \cdot \nabla)\, \mathbf{B}_s \qquad (1.6)$$

Where $\mathbf{B}_s$ is the sample stray field. This indicates that the images produced are related to the field gradient rather than the field itself. However, if the

domain at the tip apex is long, the interaction with the sample stray field can be approximated to a monopole interaction due to magnetic charge q_m:

$$\mathbf{F} = q_m \mathbf{B}_s \qquad (1.7)$$

In this case, the images represent the stray field and not the field gradient. It has been found that the tip material determines the type of image produced, e.g. Co results in dipole interactions and therefore images related to the stray field gradient, whilst Ni and Fe produce monopole interactions creating images related to the field itself [15].

Electrostatic force microscopy (EFM) can be used to study the distribution of electrical charge on a surface by probing the long-range electrostatic Coulomb forces. It has been used to monitor charge decay on a surface [11], contact electrification [12] and domains in ferroelectrics [13]. Operated in a.c. mode, the system is capable of single charge-carrier sensitivity [11]. An oscillating voltage is applied to between the tip and an electrode behind a dielectric sample at frequency ω_2, chosen to be much higher than the feedback frequency and much lower than then cantilever resonance frequency, ω_1. This induces an oscillating charge on the tip due to the oscillating charge on the electrode, Q_e. Any additional charge on the surface of the sample, Q_s, will induce an image charge on the tip. The total charge on the tip is therefore $Q_t = -(Q_e + Q_s)$. Terris et al [16] proved that for an uncharged surface, the force gradient experienced by the tip is modulated at $2\omega_2$, whereas for a charged surface it oscillates at ω_2. This charge-related signal can be detected with a lock-in amplifier, with the phase of the signal indicating the sign of the charge.

Frictional force microscopes require a modified deflection measurement system. When scanning a single beam AFM cantilever across a surface in contact mode, lateral forces are also present due to friction, which result in torsion of the cantilever. Use of optical beam deflection and a quadranted photo detector allow deflections in two perpendicular directions to be recorded, and therefore the torsion of the cantilever can be measured

simultaneously with the deflection. Feedback control of the torsion in a similar manner to other SFMs produces an image that represents a surface of constant frictional force. This technique has been used in frictional studies on an atomic scale – something not previously possible. Experiments on graphite [10] and mica [17] have shown a non-uniform frictional force, with the same spatial periodicity as the surface.

Another significant SFM technique is magnetic resonance force microscopy (MRFM). This recently developed technique (discussed in detail in section 5.8) utilises the precession of spins in a magnetic field to produce an oscillatory force on a magnetic tip. While still in the early stages of development, MRFM has the potential to produce fully three-dimensional maps of nuclear spins in a sample. Its applications range from structural identification of complex biological molecules (e.g. proteins) to quantum computing. The non-invasive nature of nuclear magnetic resonance means that it is should also be possible to produce sub-surface images using MRFM.

1.3 Other SPM techniques

A number of other scanning probe microscopes have been developed that employ the techniques used in STM and SFM. These methods generally probe an interaction other than electron tunnelling or cantilever deflection due to a force. Examples of other SPMs include scanning capacitance microscopy [18] (in which an electrode is scanned across a conducting or semiconducting surface while the capacitance between the probe and the sample is maintained at a constant value), scanning Hall probe microscopy [19,20] (where a hall probe is scanned across a sample to measure local magnetic fields), scanning thermal profiler [21] (in which a heated thermal probe is approached to a sample, the decrease in temperature of the probe due to thermal coupling is then measured). Many other SPMs exist, including scanning near-field optical microscopy, scanning near-field acoustic microscopy, scanning electrochemical microscopy and scanning noise microscopy. It is clear that

the principle of scanning a probe relative to a sample using piezoelectric transducers can be applied to a vast range of interactions. Undoubtedly more forms of SPM will be developed in the future.

1.4 Future directions of SPM

The advent of SPM has enabled characterisation of surfaces on an atomic scale. Such ability has led to direct observation of novel quantum mechanical effects, and an increased understanding of surface physics. It has also opened up an entirely new, and rapidly expanding, field of research – nanotechnology. The constant drive for smaller and smaller electronic devices means that eventually these devices will approach nanometer dimensions. Fundamental physical processes such as the electron mean free path have a similar length scale, and so have a significant effect on the operation of the device. SPM provides a set of tools for the investigation of these fundamental processes and how nanometer-scale structures behave.

The use of SPM as an analysis tool on a nanometer scale is extremely useful, however SPM has proved to be of far greater significance. SPMs have also been used to *modify* surfaces on the atomic scale. Eigler and Schweizer [22] demonstrated controlled manipulation of individual Xe atoms to form arbitrary structures at low temperature. In other experiments nanometer-scale mounds of material (typically gold) have been deposited in a controlled manner through electric field-induced evaporation with an STM tip [23]. Individual atoms have been selectively desorbed from surfaces [24], charge has been stored reversibly on nitride-on-silicon samples on a nanometer scale [25] and magnetic properties of a sample have been modified with near-atomic precision [26].

So SPM clearly has the potential to produce structures on the nanometer scale, and the ability to characterise the structures formed. This places SPM in a uniquely significant position in the development of the electronic circuits of

the future. Nanotechnology is not simply a scientific novelty; it is of major industrial importance, highlighted by the recent announcement of the American National Nanotechnology Initiative. President Clinton announced that 500 million dollars of government funding was to be invested in nanotechnology in the year 2001 alone [27]. However, for it to be a viable technology, numerous problems must be overcome.

With the discovery of carbon nanotubes [28], sheets of graphite wrapped to form molecular tubes, nanotechnology has taken considerable steps forward. The combination of SPM and nanotubes has resulted in the creation of molecular devices such as a nanotube transisitor [29]. So it seems that the aim of molecular-scale electronic circuits is within our reach. However, for industrial nanotechnology to become a reality, it is essential that speed and reliability of circuit formation be optimised. A single SPM moving atoms or molecules one-by-one is not suitable for mass production of devices. Instead, it is possible that large arrays of microfabricated SPMs working in parallel will be constructed. Prototypes of such systems have already been built consisting of an array of STMs on independently controlled bimorphs [30]. However the field develops, it is clear that SPM has an important role in nanotechnology, and will be developed as an industrial tool to be used in the construction of future generations of electronic circuits.

1.5 Summary

A brief description of the principles used in scanning tunnelling microscopy, scanning force microscopy, and other related techniques have been presented, including brief descriptions of the instrumentation used. A discussion of nanotechnology and the future role of SPM in nanotechnology have also been given. This discussion explains the motivation for much of the work presented in this thesis, and what future instrumentation development is possible.

1.6 References

1. G. Binnig, H. Rohrer, Ch. Gerber and E. Weibel, Phys. Rev. Lett. **49**, 57 (1982)
2. G. Binnig, H. Rohrer, Ch. Gerber and E. Weibel, Phys. Rev. Lett. **50**, 120 (1983)
3. J. Tersoff and D. R. Hamann, Phys. Rev. B **31**, 805 (1985)
4. G. Binnig, C. F. Quate and Ch. Gerber, Phys. Rev. Lett. **56**, 930 (1986)
5. G. Meyer and N. M. Amer, Appl. Phys. Lett. **53**, 1045 (1988)
6. R. Erlandsson, G. M. McClellend, C. M. Mateand S. Chiang, J. Vac. Sci. Technol. A **6**, 266 (1988)
7. D. Rugar, H. J. Mamin, R. Erlandsson, J. E. Stern and B. D. Terris, Rev. Sci. Instrum. **59**, 2337 (1988)
8. Y. Martin and H. K. Wickramasinghe, App. Phys. Lett. **50**, 1455 (1987)
9. Y. Martin, D. W. Abraham and H. K. Wickramasinghe, App. Phys. Lett. **52**, 1103 (1988)
10. C. M. Mate, G. M. McClelland, R. Erlandsson and S. Chiang, Phys. Rev. Lett. **59** 1942 (1987)
11. C. Schönenberger and S. F. Alvarado, Phys. Rev. Lett. **65**, 3162 (1990)
12. B. D. Terris, J. E. Stern, D. Rugar and H. J. Mamin, Phys. Rev. Lett. **63**, 2669 (1989)
13. F. Surenbach and B. D. Terris, Appl. Phys. Lett. **56**, 1703 (1990)
14. H. J. Mamin, D. Rugar, J. E. Stern, B. D. Terris and S. E. Lambert, Appl. Phys. Lett. **53**, 1563 (1988)
15. Schönenberger and S. F. Alvarado, Z. Phys. B **80**, 373 (1990)
16. B. D. Terris, J. E. Stern, D. Rugar and H. J. Mamin, J. Vac. Sci. Technol. A **8**, 374 (1990)
17. R. Erlandsson, G. Hadziioannou, C. M. Mate, G. M. McClelland and S. Chiang, J. Chem. Phys. **89**, 5190 (1988)
18. J. R. Matey and J. Blanc, J. Appl. Phys. **57**, 1437 (1985)
19. H. F. Hess, R. B. Robinson and J. V. Waszczak, Physica B **169**, 422 (1991)

20. A. Oral, S. J. Bending and M. Henini, J. Vac. Sci. Technol. B **14**, 1202 (1996)
21. C. C. Williams and H. K. Wickramasinghe, Appl. Phys. Lett. **49**, 1587 (1986)
22. D. M. Eigler and E. K. Schweizer, Nature **344**, 524 (1990)
23. H. J. Mamin, S. Chiang, H. Birk, P. H. Guethner and D. Rugar, J. Vac. Sci. Technol. B **9**, 1398 (1991)
24. I. –W. Lyo and Ph. Avouris, J. Chem. Phys. **93**, 4479 (1990)
25. R. C. Barrett and C. F. Quate, J. Appl. Phys. **70**, 2725 (1991)
26. R. Wiesendanger, I. V. Schvets, D. Bürgler, G. Tarrach, H. –J. Güntherodt and J. M. D. Coey, Z. Phys. B **86**, 1 (1992)
27. W. J. Clinton, press release at http://www.nano.gov/press.htm (2000)
28. S. Iijima, Nature 354, 56 (1991).
29. S.J. Tans, A.R.M. Verschueren and C. Dekker, Nature **393,** 49
30. S. Akamine, T. R. Albrecht, M. J. Zdeblick and C. F. Quate, IEEE Electron. Device. Lett. **10**, 490 (1989)

Chapter 2
Experimental methods

The following chapter describes the commercial apparatus and experimental techniques used during the experiments in this thesis. Methods used to prepare samples are described along with the Si(100)-2x1 surface reconstruction and a discussion of C_{60}. A description of the ultra-high vacuum system and commercial UHV STM is presented. However, much of the work in this thesis utilises custom-built equipment, which will not be discussed here as it is presented elsewhere (chapters 3 and 5).

2.1 Description of UHV system

Some of the experiments in this thesis, such as those described in chapter 4, require the surface of a sample to be clean on an atomic scale. This can be obtained in an ultra high vacuum (UHV) system, where the number of gas atoms or molecules incident on a surface is small compared to atmospheric pressure. Such a vacuum, with a pressure $<10^{-8}$ Torr, can be achieved with an arrangement of stainless steel chambers attached to suitable pumps. However, even in pressures as low as 10^{-10} Torr a sample can become coated in a monolayer of adsorbates in a period of 5 hours due to the residual gas atoms in the system interacting with the sample surface.

A commercially supplied UHV system [1] was used for all experiments requiring such conditions. It consisted of three connected stainless steel chambers pumped by ion pumps, plus a load-lock for the exchange of samples between air and UHV. The chambers are highlighted on figure 2.1, with the load-lock shown in green, the sample preparation chamber in blue, the STM chamber in yellow, and the analysis chamber in red. Pressures $\sim 10^{-11}$ Torr are routinely achieved inside the UHV chambers after the system has been heated to 150°C for a period of 12-15 hours. This baking procedure desorbs

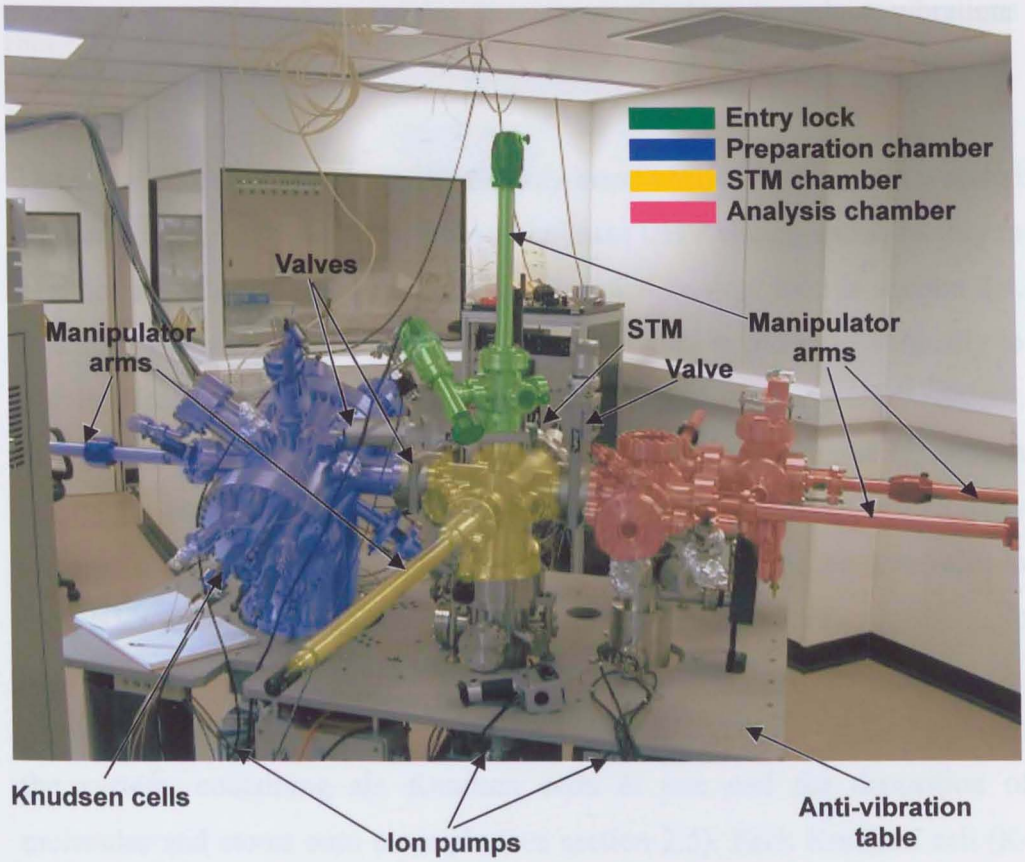

Figure 2.1 *Photograph of UHV STM system. False colour highlights indicate the different chambers.*

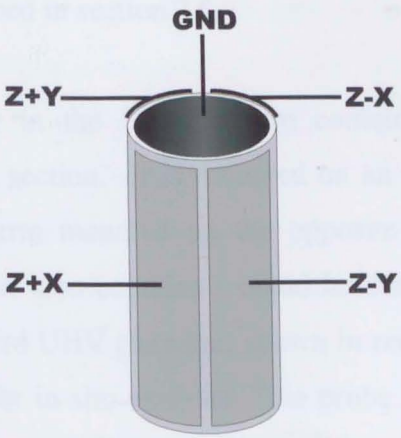

Figure 2.2 *Standard signal connections to a piezoelectric scan tube*

molecules that are adsorbed on the chamber walls. The entire UHV system is mounted on a table supported by four pneumatic legs to reduce vibrations coupling to the system.

The entry lock consists of a small six-way-cross chamber with a viton-sealed door and a gate valve to isolate it from the main UHV chambers. A facility to heat tips is included in the entry lock, which will be described in section 2.4. In addition, a magnetically coupled manipulator arm is mounted vertically to enable transfer of tips and samples between the load-lock and UHV system. The chamber is pumped down from atmospheric pressure initially using a diaphragm pump and subsequently with a turbo molecular pump, with a base-pressure of $\sim 10^{-8}$ Torr. At this pressure, it is possible to open the gate valve to the UHV system in order to transfer samples.

The sample preparation chamber (shown in blue in figure 2.1) is the largest in the system, containing six Knudsen cells at one end for deposition of molecules and atoms onto a sample (see section 2.5). Each Knudsen cell (K-cell) points towards the centre of the chamber and has a shutter to enable precise control of the duration of deposition. A manipulator arm is mounted on the side of the chamber to transfer samples to and from the rest of the system, and to position the sample for deposition. The chamber also contains an electrical feedthrough, used to resistively heat the sample during preparation, as described in section 2.6.

The central chamber in the UHV system contains the UHV STM head described in the next section. It is mounted on an 8 inch flange at one end with a manipulator arm mounted on the opposite end for tip and sample transfer. The chamber also contains a metal holder, used to store spare tips and samples. The third UHV chamber, shown in red in figure 2.1, contains a UHV sample probe for in-situ analysis. The probe system is currently under development, and was not used during the experiments described in this thesis.

2.2 Description of Oxford Instruments UHV STM head

Figure 2.3 shows a photograph and schematic of the commercial UHV STM head, manufactured by Oxford instruments. Attached to a vertically mounted 8 inch flange, the head consists of a stage suspended by stainless steel springs. The springs contain thin pieces of viton to damp any motion, and are arranged to oppose movement of the stage in all three dimensions. The stage can also be rigidly clamped to facilitate sample and tip transfer.

A piezoelectric scan tube, mounted on a set of inertial sliding motors (see next section), is located at the centre of the stage. There are four electrodes on the outer surface of the tube, and a single electrode on the inner surface, as shown in figure 2.2. These allow voltages, typically up to ~150V, to be applied to the tube in order to create controlled distortion. On application of the combinations of signals shown in figure 2.2, bending can be produced in two perpendicular directions (X and Y) in addition to an overall expansion or contraction (Z direction) of the tube. Tip nuts containing tungsten tips (see section 2.4) can be screwed into a threaded metal tube that is attached to, but electrically isolated from, the end of the scan tube. An electrical connection from the metal tube to a feedthrough on the STM flange is made at the back of the tube, and runs through the inside of the scan tube.

Positioned close to the piezoelectric scan tube on the STM stage is a sample mounting-block. The block contains a circular hole into which the sample holder, shown in figure 2.4, can be inserted. Once inserted, the sample is positioned close enough to the STM tip to be viewed through a binocular optical microscope via a suitably positioned mirror. The tip can then be moved to the desired location on the sample and approached towards the surface using the inertial sliding motors.

The sample holder consists of a machinable glass body with a two-part phosphor-bronze rear. Mounted in the centre of the front face, electrical connections to the sample are made via two tantalum clips, which are also connected to the phosphor-bronze segments at the rear. The sample can be

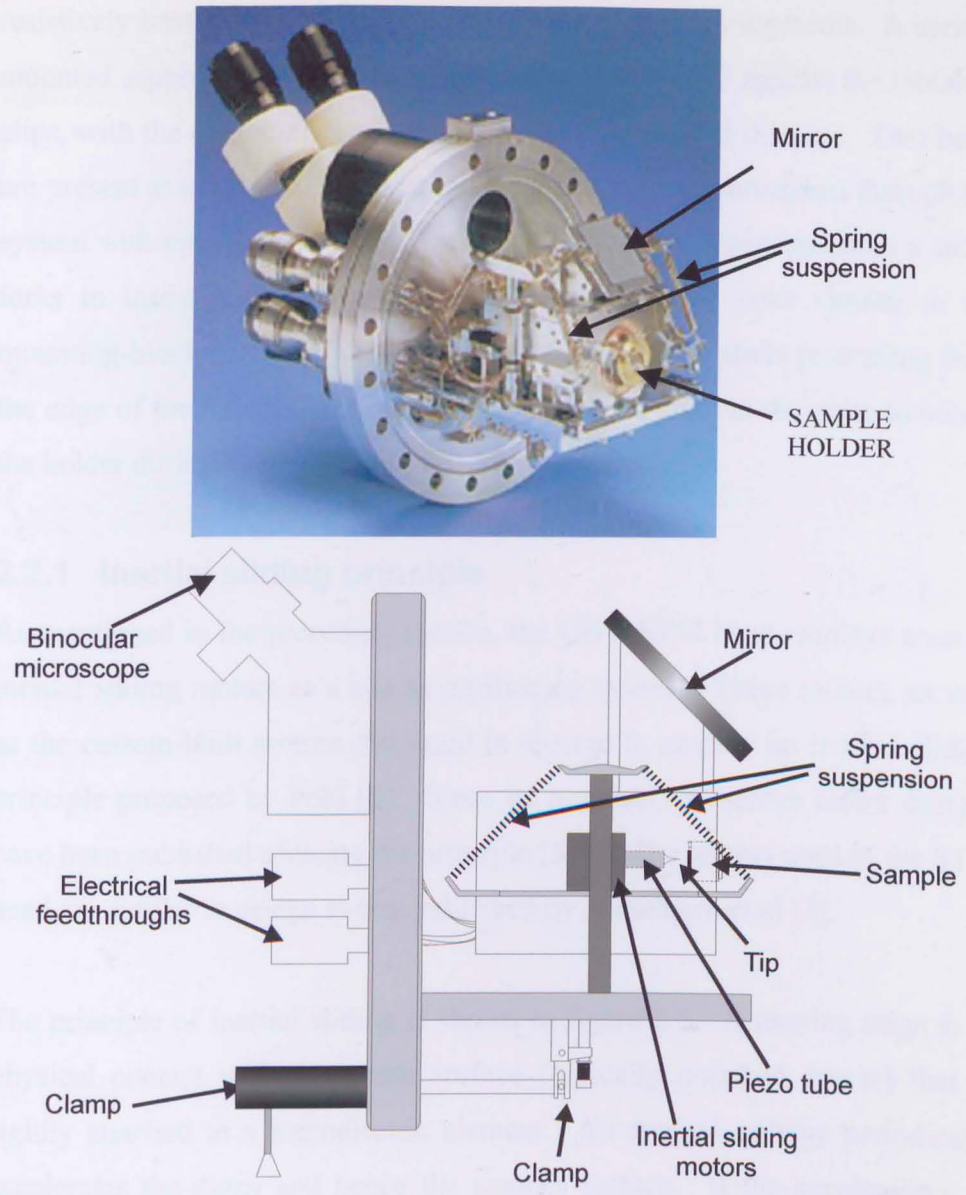

Figure 2.3 *Photograph and schematic of the Oxford Instruments UHV STM head*

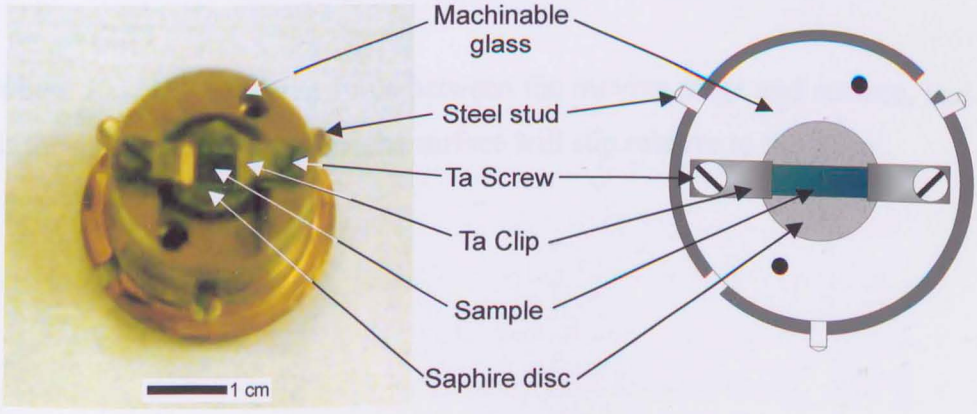

Figure 2.4 *Photograph and schematic of sample the holder.*

resistively heated by applying a voltage between the two segments. A spring-mounted sapphire disc is used to hold the sample firmly against the tantalum clips, with the degree of clamping adjusted by a screw at the rear. Two holes are present at the rear of the sample holder to facilitate movement through the system with manipulator arms. Each manipulator arm contains either a set of forks to insert into the sample holder, or a circular yoke similar to the mounting-block on the STM head. Three stainless steel studs protruding from the edge of the holder connect with corresponding slots in the yoke to secure the holder during manipulation.

2.2.1 Inertial sliding principle

As mentioned in the preceding section, the UHV STM head employs a set of inertial sliding motors as a coarse positioning system. These motors, as well as the custom-built motors discussed in chapter 5, employ an inertial sliding principle proposed by Pohl [2]. Since its proposal, numerous motor designs have been published utilising the principle [3-5]. The motors used in the STM head are similar in design to that published by Woodburn et al [3].

The principle of inertial sliding is shown in figure 2.5. A moving stage is in physical contact with a smooth surface (typically polished quartz) that is rigidly attached to a piezoelectric element. An applied voltage periodically accelerates the piezo and hence the smooth surface. If the acceleration, a, overcomes the ratio

$$a > \frac{F_{frict}}{m} \qquad (2.1)$$

where F_{frict} is the friction force between the moving stage and surface, and m is the mass of the stage, then the surface will slip relative to the stage.

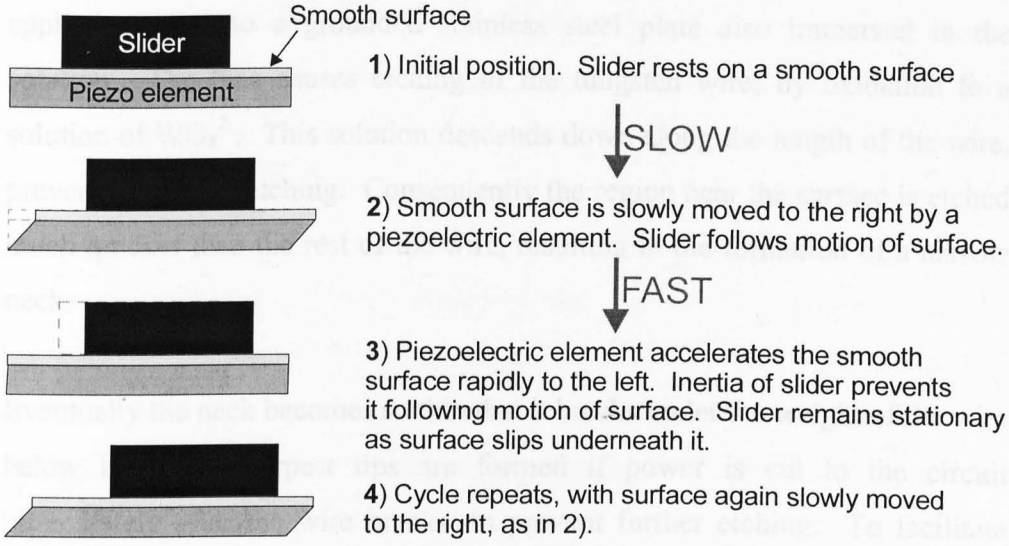

Figure 2.5 *Inertial sliding principle for horizontal motion with no clamping.*

A net displacement of the sliding stage can be achieved if the piezoelectric element is moved back and forth with an acceleration in one direction that exceeds the ratio in equation 2.1, while the acceleration in the opposite direction does not. Sawtooth [2], exponential [3], and cycloidal [4] driving waveforms have all been used in inertial sliding motors.

Inertial sliding motors are ideal for STM applications as they exhibit reproducible step sizes in the range 100Å-3μm [4 and chapter 5] and can be built with a range of travel >10mm. Such motors are routinely used under both UHV and low temperature experimental conditions [5,4].

2.3 Tip preparation

An electrochemical method for producing high quality tungsten tips has been developed by past members of our group from previously reported methods [6,7], and is used to prepare all tips used with the UHV STM system. A length of 0.5mm diameter tungsten wire is inserted into a tantalum tip nut, such that ~5mm protrudes from the end of the nut. A 3 molar aqueous solution of NaOH is then used to electrochemically etch the tip. The tungsten wire is immersed to a depth of ~3mm into the solution, and a +9V bias is

applied relative to a grounded stainless steel plate also immersed in the solution. The bias causes etching of the tungsten wire, by oxidation to a solution of WO_4^{2-}. This solution descends down along the length of the wire, preventing further etching. Consequently the region near the surface is etched much quicker than the rest of the wire, resulting in the formation of a narrow neck.

Eventually the neck becomes so thin that it breaks under the weight of the wire below it. The sharpest tips are formed if power is cut to the circuit immediately after the wire breaks, to prevent further etching. To facilitate this, the power supply has a current sensing circuit that turns off the applied voltage when the current drops below a threshold. When the wire breaks, the current drops significantly as the electrode is much smaller, consequently the power supply automatically is switched off.

After etching, the tip is inserted into the entry lock of the UHV system, which is then pumped down as described in section 2.2. At a sufficiently low pressure, the tip is heated by electron bombardment to ~1000°C for ~5 minutes in order to clean it. A hot tungsten filament is mounted inside the entry lock as a source of electrons. When a bias of ~1kV is applied to the tip, which is positioned near to the hot filament, electrons from the filament are attracted to the tip, which consequently gets hot.

2.4 Knudsen cell description and operation

The C_{60} molecules used in chapter 4 were deposited using a Knudsen cell (K-cell), which is a form of UHV evaporator. If the mean free path of the evaporated molecules is long compared to the aperture dimensions, the resulting flow is known as Knudsen or molecular flow. The K-cells attached to the UHV system consist of a pyrolytic boron nitride (pBN) crucible and heater. The charge (in this case C_{60}) is placed at the bottom of the 100mm long crucible inside an electrically insulated heater filament. The temperature

of the crucible is monitored using a tungsten/rhenium thermocouple attached to a Eurotherm temperature controller. A constant temperature in the crucible can be maintained by an intelligent feedback loop in the controller connected to the heater power supply.

Before use, the K-cell was outgassed for several hours slightly below operating temperature to ensure pressures below $3x10^{-10}$ Torr were maintained during deposition. Accurate control of deposition duration was achieved through the use of a pneumatic shutter located in front of the K-cell that blocked the molecular flow when shut.

2.5 Si(100)-2x1

The Si(100) surface is widely used as a substrate in the semiconductor industry, and is therefore of considerable technological importance. Like most semiconductors, under UHV conditions a clean Si(100) surface can undergo *reconstruction*; the top layers of the crystal re-arrange to minimise the free energy of the surface by reducing the number of dangling bonds. The reconstructed surface has a periodicity that is different to the bulk material and is expressed in Woods notation as multiples of the surface lattice vectors (e.g. 2x1 for Si(100)).

A schematic of the Si(100)-2x1 surface is shown in figure 2.6. After reconstruction, the top layer atoms are paired together as dimers, arranged in rows. The distance between dimers within a row is $a_0/\sqrt{2}$ = 3.84Å, and the separation of the rows is $a_0\sqrt{2}$ = 7.68Å, where a_0 is the bulk lattice constant = 5.43Å.

Figure 2.7 shows STM images of the surface (obtained using a custom-built controller that will be described in chapter 3). Image a) demonstrates the rotation of the dimer rows by 90° between terraces. Characteristic buckling of the dimers can also be seen. It has been proposed that the dimer oscillates

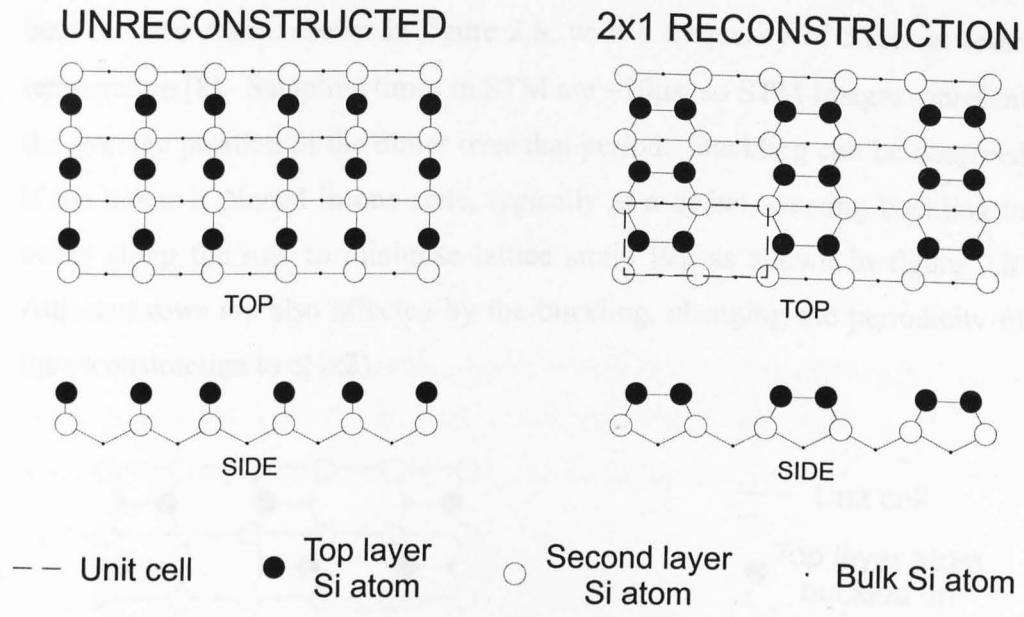

Figure 2.6 *Schematic of the Si(100)-2x1 surface reconstruction. Reconstructed surface exhibits rows of dimers.*

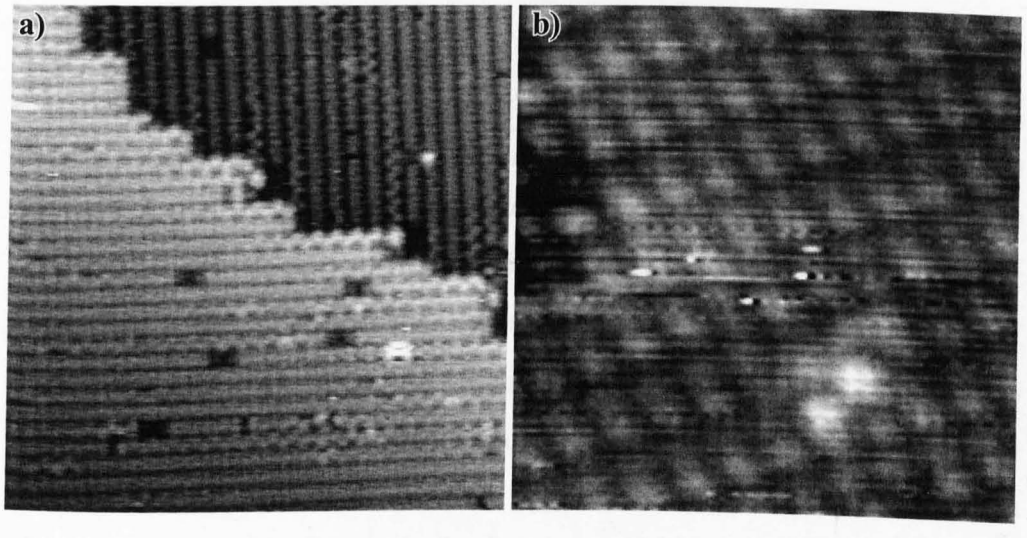

Figure 2.7 *STM images of Si(100)-2x1. a) 200x200Å^2 filled states image. Scan parameters: -3.0V, 0.2nA b)35x35Å^2 empty states image. Scan parameters: +3.5V, 0.2nA*

between two states, shown in figure 2.8, with a frequency of 5THz at room temperature [8]. Sampling times in STM are ~10μs, so STM images represent the average position of the dimer over that period. Buckling can be observed if the dimer is pinned in one state, typically at a defect, causing buckling to occur along the row to minimise lattice strain [9], as shown in figure 2.8. Adjacent rows are also affected by the buckling, changing the periodicity of the reconstruction to c(4x2).

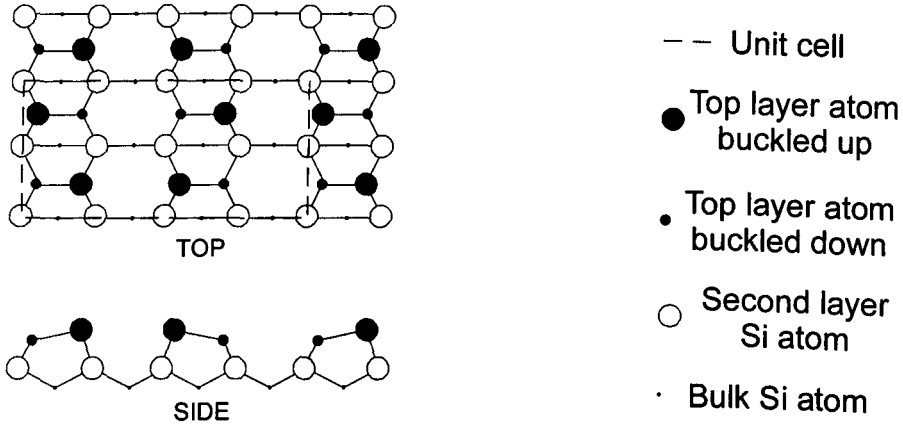

Figure 2.8 *Schematic of the Si(100)-c(4x2). Dimers are alternately buckled up and down along the row, and mirrored in adjacent rows.*

To prepare a sample of Si(100)-2x1, a 5x3 mm^2 section of Si(100) was cut from a single crystal wafer and mounted on the sample holder described in section 2.3 after blowing with N_2 gas to remove particulates. The sample was then inserted into the UHV system and resistively heated to ~600°C overnight to outgas. It was then flash annealed to ~1200°C (measured using an optical pyrometer) for ~1 minute after which it was held at 800°C for a further 5 minutes to produce the 2x1 reconstruction with a low (~1%) defect density. The samples of Si(111)-7x7 used to test the STM controller described in chapter 3 were prepared in a similar manner, with the omission of a 5 minute anneal at 800°C.

2.6 C_{60} - Buckminsterfullerene

C_{60}, or Buckminsterfullerene, is the most abundant member of a family of recently discovered carbon molecules [10,11], referred to as fullerenes. A fullerene is defined as a closed cage carbon molecule containing 12 pentagonal faces and any number of hexagonal faces, of which C_{60} has 20. The hexagons are arranged around each pentagon such that no two pentagons are adjacent. This results in a truncated icosahedron structure, similar to a football, with a cage diameter of 7.1Å, shown in figure 2.9.

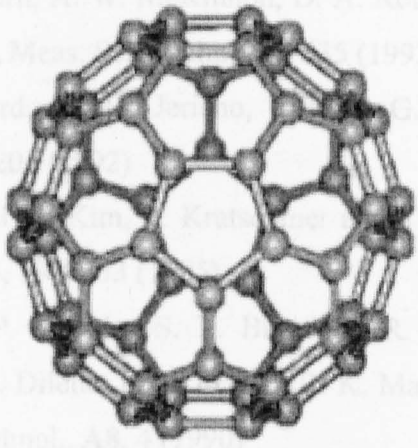

Figure 2.9 *Ball-and-stick representation of C_{60}*

C_{60} was first produced by laser vaporisation of graphite into a He carrier gas [10], however this only resulted in minute quantities. An alternative method of production [12] in which carbon rods were vaporised by resistive heating in an inert He atmosphere produced larger quantities. This method, combined with procedures to isolate C_{60} from other compounds [13,14], has enabled high purity C_{60} (>99.5%) to be produced in gram quantities for use in experiments.

2.7 Summary

A range of UHV techniques have been described that were used in the experiments described in later chapters of this thesis. In addition the Si(100)-

2x1 surface reconstruction has been discussed, with a description of the preparation method used. The fullerene molecule C_{60} has also been described.

2.8 References

1. Supplied by Oxford Instruments SPM group, formerly WA Technology
2. D. W. Pohl, Rev. Sci. Instrum., **58**, 54 (1987)
3. C. N. Woodburn, A. W. McKinnon, D. A. Roberts, M. E. Taylor and M. E. Welland, Meas. Sci. Technol. **4**, 535 (1993)
4. B. L. Blackford, M. H. Jericho, and M. G. Boudreau, Rev. Sci. Instrum., **63**, 2206 (1992)
5. S. Kleindiek, H. S. Kim, E. Kratschmer and T. H. P. Chang, J. Vac. Sci. Technol. B, **13**, 2653 (1995)
6. J. P. Ibe, P. P. Bey Jr., S. L. Brandow, R. A. Brizzolara, N. A. Burnham, D. P. Dilella, K. P. Lee, C. R. K. Marrian and R. J. Colton, J. Vac. Sci. Technol., **A8**, 4 (1990)
7. R. Zhang and D.G. Ivey, J. Vac. Sci. Technol., **B14**, 1 (1996)
8. P. C. Weakliem, G. W. Smith and E. A. Carter, Surf. Sci. **232**, L219 (1990)
9. O. L. Alerhand and E. J. Mele, Phys. Rev. B, **35**, 5533 (1987)
10. H. W. Kroto, J. R. Heath, S. C. O'Brien, R. F. Curl and R. E. Smalley, Nature **318**, 162 (1985)
11. D. E. Manilopoulos, J. C. May and S.E. Down, Chem. Phys. Lett. **181**, 105 (1991)
12. W. Krätchmer, L. D. Lamb, K. Fostirooulos and D. R. Huffman, Nature **347**, 351 (1990)
13. D. S. Bethune, G. Meijer, W. C. Tang and H. J. Rosen, Chem. Phys. Lett. **174**, 219 (1990)
14. R. Taylor, J. P. Hare, A. K. Abdul-Sada and H. W. Kroto, J. Chem. Soc., Chem. Commun. **20** 1423 (1990)

Chapter 3

Construction of a multipurpose scanning probe microscope controller

In this chapter a versatile scanning probe microscope controller capable of data acquisition during molecular manipulation is described. The system, based on a commercial digital signal processor board interfaced to a Pentium PC, has been designed and constructed entirely within the School of Physics and Astronomy at Nottingham University. Its versatility has been demonstrated in the control of a number of SPMs within our research group and in molecular manipulation experiments using a commercial UHV STM head [1]. The controller, described in a recently published paper [2], uses the DSP board to produce all analogue outputs, resulting in an extremely flexible system with complete control of the probe tip. The software written for the controller utilizes a modular architecture, making it possible to enhance and upgrade quickly and easily.

3.1 Introduction

The last ten years has seen a massive increase in processing power of cheap, commercially available, microprocessors. One type of processor that has found a particularly wide range of uses, from mobile telecommunications to digital video, is the digital signal processor (DSP). Designed for high data-rate processing of analogue signals, it is ideally suited for scanning probe microscope (SPM) control.

The first scanning tunnelling microscopes [3,4] were controlled entirely by analogue electronics. However, it was not long before computer control was introduced. The versatility of computer control, combined with the ability to store and manipulate acquired images made them preferential to analogue

systems. Early computer controlled systems used an analogue feedback circuit and digital lateral position control [5,6]; the computers were not fast enough to perform digital feedback control at update rates suitable for stable SPM operation (>20kHz) without considerable financial investment [7]. With the development of the DSP, digital feedback control became possible, offering the flexibility to implement novel control and scan routines [8,9].

With the number of available SPM modes constantly increasing, it is common for a set of control electronics to be used for more than one application. Commercial systems are often now capable of operation in several SPM modes using a single instrument [10]. Through the use of DSPs, SPM control systems can be easily developed for use with a range of instruments. The control system described in this chapter was developed for use with a number of SPM instruments within our group, and motivated by the need to acquire data during room temperature molecular manipulation experiments (see chapter 4). An additional requirement of the system was that it was flexible enough to be expanded for use with new systems, such as the magnetic resonance force microscope (see section 5.8) as they are developed.

3.2 Feedback control

Feedback control is a process that maintains a given property of a system at a constant level independent of small perturbations to the system. For example, in a STM, the tunnel current between tip and sample is kept constant while the tip is moved across the sample surface. Feedback control can be implemented in a large number of ways, all of which have a few basic elements. A property of the system (e.g. tunnel current) is measured and compared to a reference value. The result of this comparison is then fed back into the system to correct any error. In a STM, the tunnel current is compared to a reference current. The measured error is then converted into a change in voltage applied to the piezoelectric scanner, resulting in a displacement of the tip to correct the error.

3.2.1 Three-term control (PID)

The algorithm employed in the control system described here is three-term, or proportional-integral-derivative (PID) control. Three-term control is a common feedback algorithm that is simple to implement and extremely versatile. It is particularly useful in systems where an exact theoretical model is not available, as critical response parameters may be determined experimentally. This is often the case in SPM, as the probe-sample interaction is highly complex and cannot be characterised completely.

In three-term control, the controlled property of the system (such as tunnel current) is continuously compared to a reference value, or setpoint. An output is then applied to the system calculated from an algorithm consisting of the sum of three terms. The first term is *proportional* to the error between the setpoint and the measured value, the second is proportional to the *integral* of the error and the third is proportional to the *derivative* of the error (hence the alternative name "PID control"). The output, U, at time t, can be expressed algebraically as:

$$U(t) = PE(t) + \int IE(t)dt + D\frac{dE}{dt} \qquad (3.1)$$

Where E(t) is the error between the measured value and the setpoint, and P, I and D are constants. The proportional constant, P, relates the measured value to the output value in a linear fashion. In a STM, it is related to the rate of change of tunnel current with Z height, and how piezo drive voltage is related to Z height (i.e. the piezoelectric constant of the scan tube). With just proportional control, a system will exhibit a steady state error as the output only depends on the difference between the setpoint and measured value. So if the difference is zero, the output will be zero. Consequently, the system will generally stabilise to a steady state that is offset from the setpoint.

To eliminate this offset, an integral term can be introduced. Since the integral term is dependent on all previous values of the error, it can have a non-zero value even when the error is zero. The derivative term is sometimes omitted

from feedback algorithms, as it is not essential to the functionality of the system. However, it can improve response to perturbations as it modifies the output according to the rate of change of the difference. It can also be used to improve stability of the feedback system.

Most real systems have a finite response time, so changes in output will not affect the measured value immediately. In STM, there are delays associated with the response of the piezoelectric scan tube, and with the control electronics themselves. When analysed in the frequency domain, these appear as phase lags in the signal. If the phase lag at a given frequency is 2π, and the gain overall gain at that frequency is >1, instability occurs and the system starts to oscillate [11,12]. Bode plots (gain or phase versus frequency plots) can be produced for any feedback system in order to determine the location of these instabilities. With three-term control, careful choice of gains (i.e. values of P, I, and D) prevents oscillation in most cases. Figure 3.1 shows examples of different feedback gains, and their effect on the feedback response to a step change in setpoint. For a more detailed discussion of feedback control and analysis in STM, see references 4, 11 and 12.

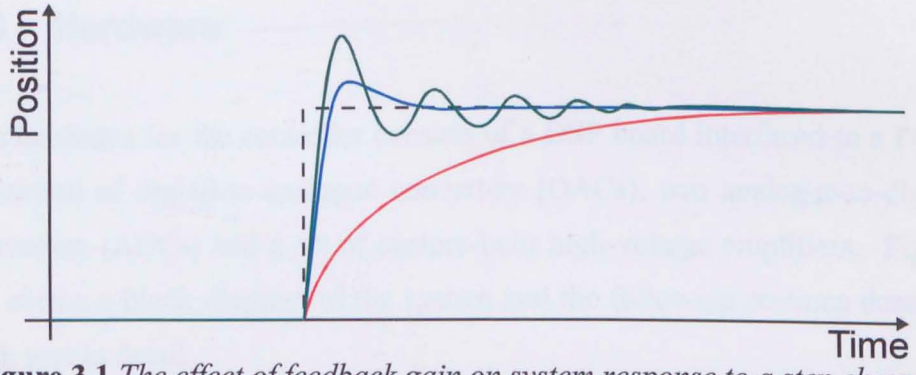

Figure 3.1 *The effect of feedback gain on system response to a step change. Red line shows too low gain – system responds slowly, blue line is optimum response with minimum overshoot, and green line is too high gain – system overshoots and oscillates for a considerable period.*

In many systems optimum values for P, I and D can be theoretically derived from the physical properties of the system. However, in scanning probe microscopy it is usually more practical to determine their values experimentally due to the variable nature of the probe-sample interaction.

3.2.2 Digital feedback control

The description of three-term control given above applies to analogue systems. To implement such a control system on a computer, it is necessary to convert the algorithm to a discrete form. So now, rather than continuously varying, the input is sampled and output is updated at discrete time intervals. Using finite differences, equation 3.1 can be written in discrete form:

$$U_i = PE_i + \sum_{j=o}^{j=i} I\Delta TE_j + \frac{D}{\Delta T}(E_i - E_{i-1}) \qquad (3.2)$$

Where 'i' is the iteration number, E_i is the i^{th} difference between the setpoint and measured value, ΔT is the period between output updates and P, I and D are the same constants as before. A digital signal processor is ideal for this kind of calculation provided that the input signal varies slower than the update rate of the feedback algorithm. In a scanning probe microscope the input signal typically varies at audio frequencies (kHz), so a DSP is ideal for digital feedback.

3.3 Hardware

The hardware for the controller consists of a DSP board interfaced to a PC, a collection of digital-to-analogue converters (DACs), two analogue-to-digital converters (ADCs) and a set of custom-built high-voltage amplifiers. Figure 3.2 shows a block diagram of the system and the following sections describe each part in detail.

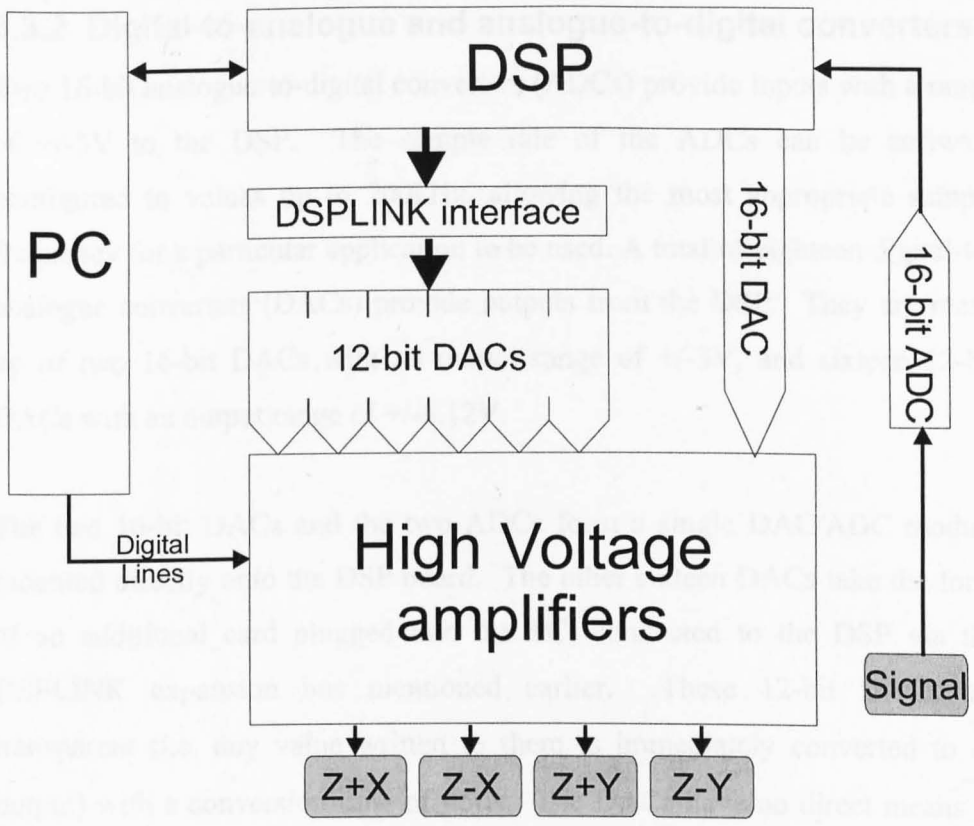

Figure 3.2 *Block diagram of SPM controller system.*

3.3.1 The Digital Signal Processor board

The digital signal processor chosen for the controller was a Texas Instruments TMS320C32 – a 32-bit processor optimised for floating point calculations. It has a peak processing power of 50 MFLOPS. The chip forms part of a PC expansion board [13] housed within a standard Pentium PC running Windows 95. The board contains an area of 512 kilobytes of static RAM for DSP program storage, plus an area of 32 kilobytes of dual port RAM for sharing data with the PC. In addition, the DSP board also has a DSPLINK expansion bus [14] and two mounting sites for DAC/ADC modules. Although the DSP board is housed within a PC, it essentially runs completely independently. Programs are written on the PC in a mixture of C and assembly code, and then compiled for the DSP. The compiled code is downloaded and run on the DSP board.

3.3.2 Digital-to-analogue and analogue-to-digital converters

Two 16-bit analogue-to-digital converters (ADCs) provide inputs with a range of +/-3V to the DSP. The sample rate of the ADCs can be software configured to values up to 200kHz, allowing the most appropriate sample frequency for a particular application to be used. A total of eighteen digital-to-analogue converters (DACs) provide outputs from the DSP. They are made up of two 16-bit DACs with an output range of +/-3V, and sixteen 12-bit DACs with an output range of +/-8.12V.

The two 16-bit DACs and the two ADCs form a single DAC/ADC module mounted directly onto the DSP board. The other sixteen DACs take the form of an additional card plugged into the PC, connected to the DSP via the DSPLINK expansion bus mentioned earlier. These 12-bit DACs are transparent (i.e. any value written to them is immediately converted to an output) with a conversion time of <5μs. The DACs have no direct means of communication with the PC; they simply take their power from it. Figure 3.3 shows how each DAC is used, and how they connect to the high voltage amplifiers.

3.3.3 High voltage amplifier system

A typical piezoelectric scan tube has a piezoelectric constant of ~50Å/V in the Z direction, and ~100Å/V in X-Y directions. In order to scan areas up to ~2μm^2, voltages of up to +/- 150 Volts are required to create the desired deformation of the piezoelectric tube. The outputs from the DACs described above clearly require amplification to reach these levels. However, the noise level on the Z-axis must not exceed ~0.1Å, therefore the output from the amplifiers must have a noise level less than 2mV. To achieve this low level of noise over an output range of +/-150V requires careful design of the amplifier system.

Figure 3.3 shows a block diagram of the HV amplifier system. Each axis of movement of the probe (X and Y parallel and Z perpendicular to sample plane) is the sum of two signals from the DACs - an offset and a fine signal.

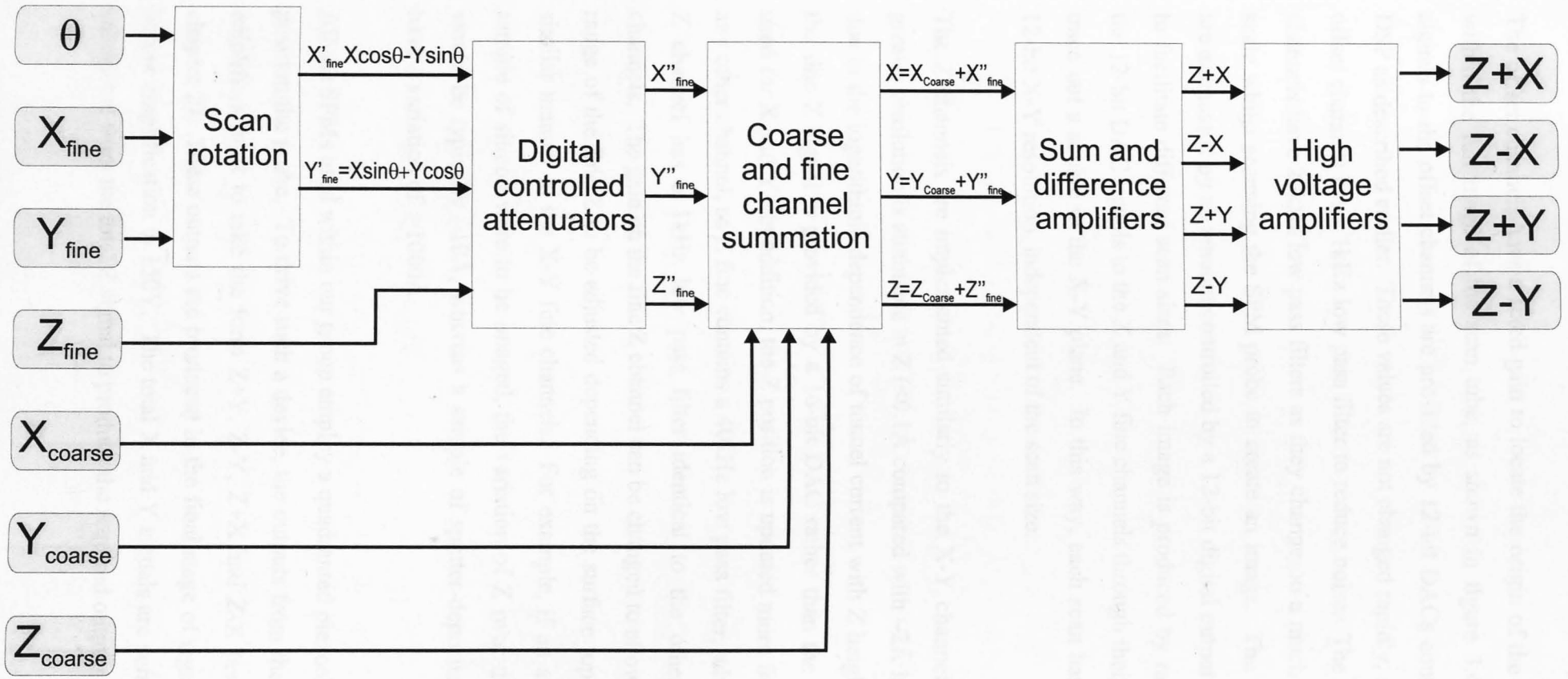

Figure 3.3 *Block diagram of high voltage amplifier system*

The offset channels have a fixed gain to locate the origin of the scan window within the full range of the scan tube, as shown in figure 3.4. The input signals to the offset channels are provided by 12-bit DACs controlled by the DSP as described earlier. These values are not changed rapidly, so each of the offset channels has a 1kHz low pass filter to reduce noise. The X and Y fine channels have 20kHz low pass filters as they change on a much shorter time-scale whilst scanning the SPM probe to create an image. The fine channels are attenuated by an amount controlled by a 12-bit digital output from the PC, to facilitate different scan sizes. Each image is produced by raster scanning the 12-bit DAC signals to the X and Y fine channels through their full range to trace out a square in the X-Y plane. In this way, each scan has a consistent 12-bit X-Y resolution, independent of the scan size.

The Z channels are implemented similarly to the X-Y channels. However, greater resolution is attainable in Z (<0.1Å compared with ~2Å laterally [18]), due to the logarithmic dependence of tunnel current with Z height. Therefore the fine Z signal is provided by a 16-bit DAC rather than the 12-bit DACs used for X and Y. In addition, the Z position is updated more frequently than any other channel, so Z fine contains a 40kHz low pass filter, while the coarse Z channel has a 1kHz low pass filter identical to the other two coarse channels. The gain on the fine Z channel can be changed to allow the dynamic range of the fine Z to be adjusted depending on the surface topography, in a similar manner to the X-Y fine channels. For example, if an atomically flat sample of silicon were to be imaged, the variation of Z over the entire scan would be typically ~10Å, whereas a sample of sputter-deposited gold could have a variation of >1000Å.

All the SPMs used within our group employ a quadranted piezoelectric tube to position the probe. To drive such a device, the outputs from the high voltage amplifiers must to take the form Z+Y, Z-Y, Z+X and Z-X (as described in chapter 2). These outputs are produced in the final stage of signal processing before amplification to 150V. The total X and Y signals are summed with, or subtracted from the total Z signal to produce the required outputs.

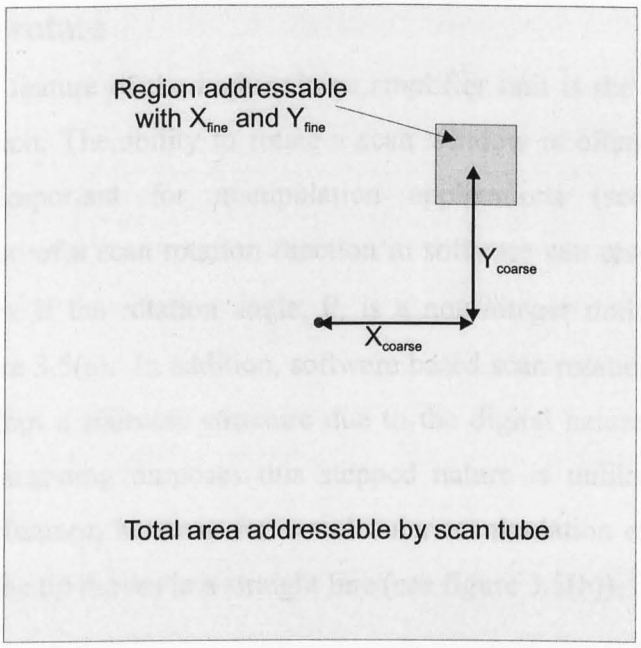

Figure 3.4 *Schematic diagram of the regions of a sample addressable using combinations of the coarse and fine channels. Large grey region represents the total addressable area, and the small dark square represents the region accessible using the fine channels (this can be scaled using different gains on the amplifiers).*

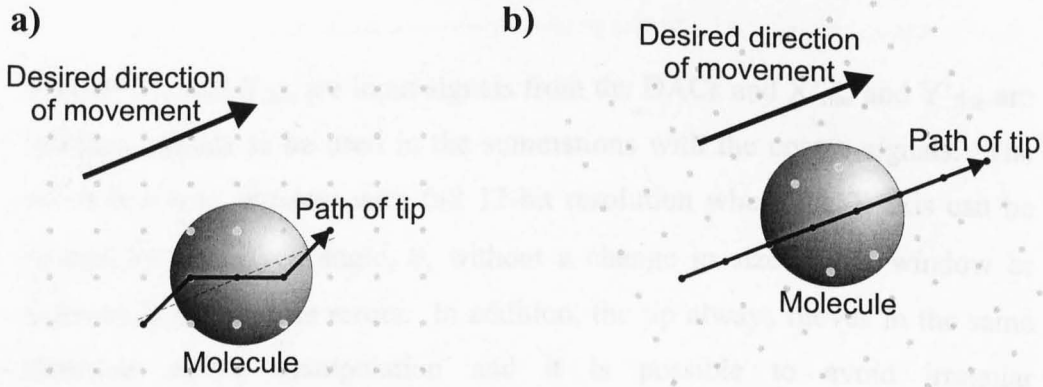

Figure 3.5 *Comparison of STM tip trajectory during a manipulation procedure with digital and analogue scan rotation. a) Scan rotation performed digitally in software. The small grey dots represent possible tip positions (limited due to digitisation of DAC outputs). The tip trajectory forms a stepped structure as an approximation to the desired direction of manipulation. b) The array of addressable points is rotated by analogue electronics to align the primary axes with the desired direction of manipulation. The tip trajectory forms a continuous line, enabling controlled manipulation experiments to be performed.*

3.3.4 Scan rotate

An important feature of the high voltage amplifier unit is the analogue scan rotation function. The ability to rotate a scan window is often useful, and is particularly important for manipulation applications (see chapter 4). Implementation of a scan rotation function in software can result in a loss of X-Y resolution if the rotation angle, θ, is a non-integer multiple of $\pi/2$ as shown in figure 3.5(a). In addition, software based scan rotation causes the X -Y axes to adopt a staircase structure due to the digital nature of the output DACs. For scanning purposes this stepped nature is unlikely to make a significant difference, however for a molecular manipulation experiment it is required that the tip moves in a straight line (see figure 3.5(b)).

To overcome these problems, an analogue rotation function has been implemented in the signal conditioning stages of the fine channels of the high voltage amplifiers. The rotation combines the X and Y fine inputs according to the following equations using sine-cosine operational amplifiers:

$$X'_{fine} = (X_{fine}\cos\theta - Y_{fine}\sin\theta) \quad (3.3)$$

$$Y'_{fine} = (X_{fine}\sin\theta + Y_{fine}\cos\theta) \quad (3.4)$$

Where X_{fine} and Y_{fine} are input signals from the DACs and X'_{fine} and Y'_{fine} are resultant signals to be used in the summations with the coarse signals. The result is a scan window with full 12-bit resolution where the X-axis can be rotated by any given angle, θ, without a change in size of the window or increase in digitisation errors. In addition, the tip always moves in the same direction during manipulation and it is possible to avoid irregular displacements (see figure 3.5(b)). In practice the orientation of the scan window must therefore be rotated so that the direction for manipulation is aligned with either the X'_{fine} or Y'_{fine} axes.

3.3.5 Inertial sliding motor control channels

Three additional high voltage channels are included in the HV amplifier unit. They are used to amplify the drive signal for inertial sliding motors used for

μm-scale positioning of the tip (see chapter 2, and section 5.3). Consisting of identical high voltage amplifiers to the scan tube system described above, they amplify exponential waveforms produced by three of the 12-bit DAC channels on the DSP card. Each channel has an additional circuit after the amplifier to short the high voltage output to ground in ~500ns in order to produce the accelerations required to initiate inertial sliding (see section 5.3).

3.3.6 Variable gain tunnel current amplifier

For scanning tunnelling microscope applications, an amplifier is required to amplify the tunnel current and convert it to a voltage suitable for ADC input. The design chosen is a two-stage system to allow a high enough signal bandwidth for STM applications. The first stage is a current to voltage conversion amplifier with a gain of 10^8, positioned as close to the tunnel junction as possible to reduce noise. The second stage consists of four digitally selectable amplifier circuits each with different gains, permitting operation at different signal levels. The gains chosen for the second stage amplifiers result in saturation tunnel current values of 1,10,100 and 1000nA. The input DAC has 16-bit resolution, so the theoretical minimum detectable tunnel current is 1/32768 nA (~0.03pA). However noise in the I-V amplifier circuit prevents this level of sensitivity. In practice, the noise level at the input to the DACs is ~10mV (this corresponds to ~0.1pA).

3.4 Software

The hardware of a SPM controller determines the ultimate resolution of the system, but the software determines its functionality and flexibility. There are two distinct parts to the software implemented in this system - the DSP program and the PC program. The main function of the DSP program is to perform the feedback calculation and control the DAC signals to the amplifiers. The PC program provides an interface for the user to interact with the SPM and to analyse acquired data.

3.4.1 DSP software

Development of the DSP software was performed on the host PC. It was written mainly in C with some additional assembly code instructions. The assembly code was required to perform specific hardware functions such as resetting interrupt flags. The C code is compiled and optimised using a compiler provided with the DSP board. After compilation, the DSP program can be downloaded into static RAM on the DSP board where it is executed. The program is then completely independent of the PC, only sharing data that is placed in dual port RAM. This leaves the DSP free to execute code without unpredictable changes in processing rate associated with the multitasking operating system of the PC (Windows 95). Regular periods between input samples are a critical part of a digital feedback loop, so independence from the PC is essential.

To facilitate regular feedback updates, an interrupt flag on the DSP board is set each time a new input sample is acquired. The DSP program then responds to this flag by entering an interrupt service routine (ISR) where it performs the feedback calculation plus other functions determined by the message system described in the next section.

3.4.1.1 Messaging system

Multitasking operating systems like Windows 95 use a method called a *messaging system* to determine what the processor should be doing at any given moment in time. A message is simply a numeric value placed into a particular memory location. Different values placed in that location represent different tasks required by the operating system. Regular checks of the memory location by the processor determine what value is present and therefore which function should be performed next.

A similar messaging system has been implemented in DSP code. A global variable is used to contain the message value. Every time the interrupt service routine is called, the message variable is checked and the corresponding

function executed. For example, a value of 0 represents an "Idle" function in which only the feedback calculation is performed. However, other values represent functions such as scan initialisation, image point acquisition, tip movement etc. In this way, complex tasks can be performed as sequence of simple operations. The PC has direct access to the message variable, so its contents can be modified at any time - immediately changing what task the SPM performs. The system is completely modular, so new functions can be added at any time without major modification to the code, allowing a library of tasks to be available. In addition, it is possible to use the system as a form of macro language in which the PC can be used to send a sequence of user-defined commands to the SPM.

To create an image, a sequence of functions are called that perform the following:

1. Move to the lower left corner of the scan window
2. Pause for a fixed duration to allow the piezoelectric tube to stabilise.
3. Calculate average of *average* samples of Z height and tunnel current for first image point. A*verage* is determined by the user in the PC software.
4. Move to the next image point via a number of intermediate points, *interpoint*, which is set by the user.
5. Pause at new image point for *settle* samples to allow feedback to stabilise. *Settle* set by user.
6. Repeat steps 3-5 until the end of the line is reached.
7. Flag to PC that a line of data is available.
8. Move to the start of the next image line.
9. Wait for PC to indicate data has been read, and then start a new image line.
10. Repeat until end of the scan.

Each function in the list above is a separate operation, called by a distinct message. It is clear that changing the method of image acquisition only requires minor changes to the DSP code. The values of *interpoint, settle* and *average* determine the overall scan rate. They are user-defined in the PC software, and can be modified during a scan.

3.4.1.2 Feedback update rate

In order to maintain a constant feedback update rate, the input sample frequency must be carefully chosen. The faster the feedback is performed the better the response of the system and the less time required for image acquisition. However, if the sample frequency is too high, the code in the ISR will not be completely executed before the next interrupt occurs. This leads to erratic timing – the next ISR is processed as soon as possible or may even interrupt the current ISR. So the interval between input samples must be chosen to be slightly longer than the time taken to perform the ISR.

The message system described in the previous section causes the duration of the ISR to depend on what function is being performed. Therefore, to ensure consistent timing the input sample rate must be set from the function with the longest duration. To test whether the updates were regular, a square-wave output was added, whose state was changed each time a feedback calculation was performed. It was found that a sample rate of 40kHz or less was required for STM control. This is considerably slower than other similar systems [9]. However, this has not posed significant problems, and the flexibility offered by the message system is essential for the molecular manipulation experiments described in chapter 4. The slow update rate is mainly due to overheads associated with aspects of the DSP code. For example it was found that the log conversion required to linearise the tunnel current took nearly half of the time spent in the ISR. For this reason, a logarithmic tunnel current amplifier is currently in development. Other overheads associated with calling subroutines from within the ISR also cause significant delays. When a subroutine is called from within an ISR, the compiler is unsure which registers on the DSP will be needed on return from the routine. To ensure proper operation, the compiler ensures that *all* registers are stored and recalled on entry and exit from a subroutine. This introduces significant time costs that are totally unnecessary in this case. To remedy the problem, the compiled assembly code can be modified (before final assembly to machine code) to remove the non-essential register storage.

3.4.1.3 DSP-PC data transfer

During program execution, all communication between the DSP and PC is performed via the dual port RAM mentioned in section 3.3.1. Standard RAM has a single port (i.e. it is connected to one source of data), whereas dual port RAM allows access from two different data sources. As a result, both the DSP and the PC can read and write data stored in the same area of memory. All the parameters controlling the feedback, plus image data acquired during a scan are stored within the dual port RAM. When a user changes a parameter on the PC program, it is immediately written to dual port RAM for the DSP to use.

Height and signal (e.g. tunnel current) data acquired during a scan are stored in dual port RAM until the completion of a scan line, at which point a flag is set and the PC reads the scan-line data and resets the flag when it has finished. This method of data transfer is far more efficient than passing single image-points one by one for several reasons. Firstly, the PC is able to perform other functions (such as displaying the scan-line) while the DSP collects data. Secondly, the PC can read the data as a single contiguous block (very efficient) rather than many individual read operations (very inefficient). Also, the DSP can move the SPM probe to the start of the next scan-line while the PC reads the data from the dual port RAM. All these improvements reduce scan acquisition time and thus increase data throughput.

3.4.2 PC software

The purpose of the PC software is essentially to provide a method of interaction between the user and the SPM. Apart from some additional image processing facilities, this is the only function of the PC software. The program runs under the Windows 95 operating system, and is split into two parts. The main program is an executable file written and compiled in Visual BASIC, the other is a set of image processing functions written in Visual C and compiled as a dynamic link library (DLL).

3.4.2.1 Visual BASIC program

Microsoft Visual BASIC has been designed to enable software authors to quickly develop Windows 95 programs without worrying about how the

program fundamentally interacts with the operating system. It was chosen as the language in which to write the SPM control software as its ease of use and windows functionality were ideal for rapid development of the graphical user interface (GUI) needed. Visual BASIC is an object orientated programming language, which means that the code is written in small re-usable modules rather than one long program. An important feature of object-oriented programs is the concept of a class. A class is a piece of code containing variables and functions relevant to a particular *type* of object [16]. In the SPM program, each scan is a separate object, but they are all *images*. A class has been written that describes the properties of a SPM image, and what functions can be performed on one. Every time a new scan is acquired or loaded from disk, a new *instance* of the image class is created. This allows scans to be opened and closed at random without many problems with memory wastage.

Most of the SPM control functions are performed through the "control panel" window. The control panel has buttons and controls relating to all the various parameters associated with the SPM. For example there are controls to set the feedback constants (P, I and D), scan constants (*average, settle and interpoint*), indicators to display the tunnel current and tip position, and buttons to acquire or abort a scan. The control panel window is what is often called a virtual instrument – a computer representation of a piece of equipment. When a parameter is changed on the control panel, the visual BASIC program immediately transfers the new value to dual port RAM for the DSP to use. To save DSP processing time, some of the values are converted to a form that is simpler for the DSP to use. For example if a user modifies the tunnel current setpoint when in STM mode, the logarithm of the new current value is calculated and passed to the DSP, or a displacement in Angstroms is converted to a change in DAC output.

During data acquisition, each line is transferred from dual port RAM to PC memory. The data is then displayed on the screen in a separate window as a normalised grey-scale map. To increase execution speed, the display of data is performed using fast graphical commands in the windows Application Programming Interface (API) – a set of functions provided with the operating

system to allow programs to quickly access the display. To make the system more intuitive, functions have been added to enable the user to move, rotate and scale the scan window visually. For example, a line can be drawn on a previously acquired image to translate the scan window across the surface of the sample.

The system is designed to control a variety of different SPM heads. Each head may have different properties such as different maximum scan range or a different approach mechanism. To facilitate these different systems, a configuration file is stored for each SPM head, containing calibration data and options set by the user. In addition, a separate DSP program can be used for each scanning mode, to allow modifications specific to a particular scan head to be implemented. This may be as simple as removing a logarithm calculation for AFM use, or as complex as adding a new data acquisition channel for photon emission STM work.

3.4.2.2 C dynamic link library

It was necessary to write image-processing routines in C as Visual BASIC was found to be too slow for such calculations. The routines perform processes such as plane subtraction, line normalisation, differentiation and image magnification. Most of these routines were written for an earlier image processing program developed by other group members [15], and have simply been utilised in the SPM control software. They have been written using visual C++ and compiled as a Windows dynamic link library. A dynamic link library is a collection of routines stored in a form that enables them to be called by any Windows program whenever required. This enables standard functions to be used by several different programs without the need to copy the code. Another example of a DLL is the windows API mentioned in the previous section.

3.5 Results

3.5.1 Noise levels

The largest source of noise in the system was found to be 50Hz mains pick-up. Low frequency noise such as mains noise can be very problematic as it produces a clear effect on acquired images. High frequency noise (>10kHz) is less important as the piezoelectric tube will not respond properly to frequencies above its natural resonance frequency (typically a few tens of kHz). Mains noise is not eliminated in this way, and so must be reduced as much as possible before reaching the scan tube. Careful positioning and screening of power supplies within the amplifier unit minimised this noise, however it was impossible to remove completely.

With the inputs to the amplifiers shorted to ground, the total broadband RMS noise (measured as the linewidth on an oscilloscope) was measured as <2mV, which meets the criteria for noise levels proposed in section 3.3.3. However, with the system connected to the DACs, the noise increased to ~5mV. This increase in noise suggests the dominant noise source is either the DAC boards or cabling to the DACs. To minimise pick-up on the cables, shielded cabling was used, and lengths were kept to a minimum. Even with the DACs connected, the noise levels are comparable to equivalent levels measured on the commercial STM controller (also ~5mV).

3.5.2 Atomic resolution STM images of silicon surfaces in Ultra-High Vacuum

The ultimate test of any SPM is its ability to image surfaces with true atomic resolution. Using a commercial UHV STM head [1] and the controller described in this chapter, atomically flat surfaces of silicon have been imaged. The STM head had an inertial sliding approach mechanism that was driven using the inertial slider controller described in section 3.3.5.

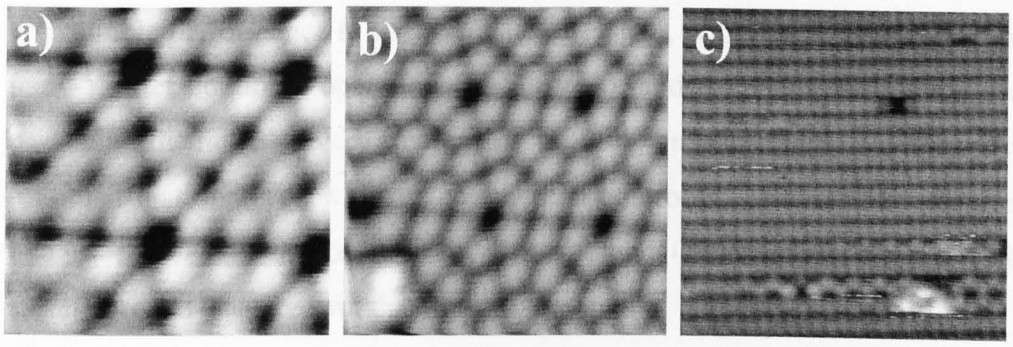

Figure 3.6 *Atomic resolution STM images of silicon surfaces. Image a) shows a filled state image of a 53x53Å area of the Si(111)-7x7 surface. Image b) shows an empty state image of a 74x74Å area of the same surface. Image c) shows a filled state image of a 98x98Å area of the Si(100)-2x1 surface. Image parameters: a)-1.0V, 2nA b)1.0V, 1nA c) -3V,0.2nA*

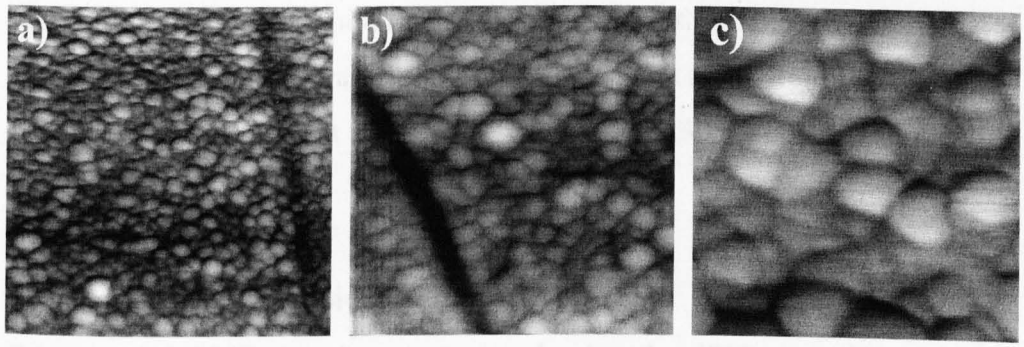

Figure 3.7 *Contact mode AFM images of aluminium grains. Note the scratch along the surface in images a) and b).Image sizes: a) 12000x12000Å b) 7000x7000Å c)4000x4000Å*

Samples of Si(111)-7x7 and Si(100)-2x1 were prepared as described in chapter 2. Figure 3.6 shows examples of the images obtained. The images are full scans, with no image processing applied (apart from simple plane subtraction to improve printed clarity). It was found that the new system had comparable performance to the commercial system, with low drift (<10Å/min in X-Y after continual operation for >5hours), and excellent resolution. In particular, the noise on very small scans (<100Å) appeared to be significantly less than that observed with the commercial controller. Attempts to acquire images equivalent to those shown in 3.6(a) and (b) using the commercial system proved unsuccessful due to noise problems.

3.5.3 AFM images

The UHV STM work described above has proved the stability and resolution of the controller. The following few sections demonstrate the versatility of the system, with examples of its use to control several different SPM systems. Firstly, the multifunction SPM head described in chapter 5 was used in contact mode AFM to acquire images of a sample of aluminium grains. The sample was a test sample supplied with a Topometrix Explorer AFM [17] used elsewhere in the department. Figure 3.7 shows several images of the surface with sizes of 12000x12000, 7000x7000 and 4000x4000Å^2. The images were acquired at a relatively early stage of development of the multifunction head, and so the system had limited vibration isolation at the time. The noise that is visible on the smallest scan is vibrational noise, not noise from the controller. However, it is clear from the images that the controller worked well with the AFM system.

3.5.4 Photon Emission STM images

Recently, Dr. Philip Moriarty has started using the SPM controller in a new custom-built photon emission STM system. The system collects light emitted from an STM tunnel junction under certain conditions and records its intensity as the sample is scanned, producing a photon map, as shown in figure 3.8(a). It is hoped this technique will provide additional information about the surface of samples. Some minor additions to the controller software were introduced

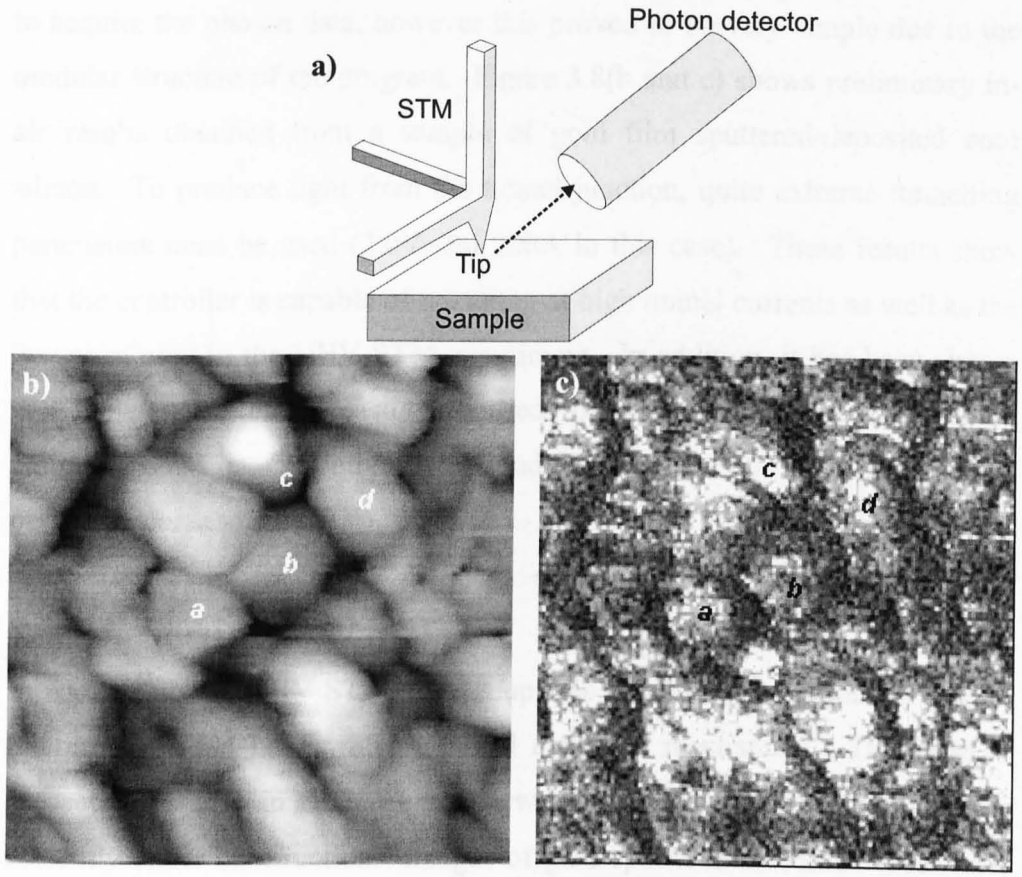

Figure 3.8 *a) Schematic of a photon emission STM. b) In-air STM image of a gold surface (500x500Å). c) Photon map showing the intensity of light emitted during acquisition of the STM image. Scan parameters: 2.0V, 20nA, peak photon intensity ~1500 counts/second.*

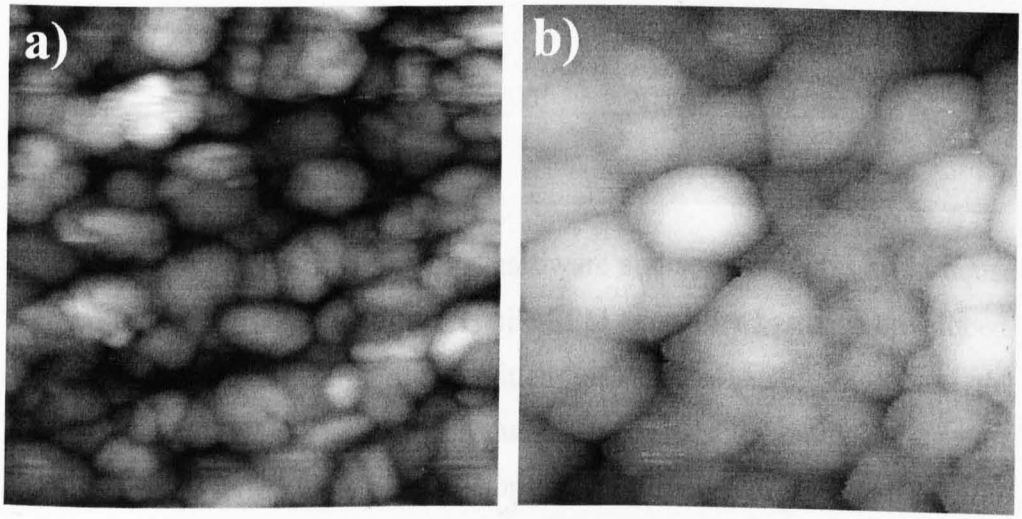

Figure 3.9 *In-air STM images of gold. Image a) shows an area of 1600x1600Å with scanning parameters of V=0.4V, I=0.1nA. Image b) is a smaller scan (480x480Å) of the same sample with the same scan parameters.*

to acquire the photon data, however this proved to be very simple due to the modular structure of the program. Figure 3.8(b and c) shows preliminary in-air results obtained from a sample of gold film sputtered-deposited onto silicon. To produce light from the tunnel junction, quite extreme tunnelling parameters must be used (2.0V and 20nA in this case). These results show that the controller is capable of operating at high tunnel currents as well as the low ones used in the UHV STM experiment. In addition, it has been shown that the system can be easily modified for new applications. The photon emission STM is currently being modified for use in UHV to improve performance.

3.5.5 Manual approach STM

In addition to the UHV STM, our group also has an earlier model of Oxford Instruments STM head with a manual approach mechanism. This head is presently operating in air, however a new UHV system in which to mount it is currently under construction. Images of gold-sputtered silicon surfaces have been acquired in air to test the functionality of the STM and its compatibility with the controller. Accurate calibration of the system will be performed once the system is operational in UHV. Figure 3.9 shows examples of images obtained with the system.

3.6 Summary

Using a combination of DSP and PC hardware and software, plus an in-house high voltage amplifier system, a versatile SPM controller has been developed. The system uses a PC interface written in Visual BASIC to control the function of a DSP. The DSP produces analogue output signals that are amplified by a set of high voltage amplifiers to drive a wide range of SPM heads. The amplifiers also contain an analogue rotation function, useful for molecular manipulation experiments. Experiments have demonstrated atomic

resolution images, and control of a UHV STM, an in air STM, a custom-built AFM and a photon emission STM system.

3.7 References

1. TOPSystem 1, provided by Oxford Instruments - formerly WA Technology.
2. M. Humphry, R. Chettle, P. Moriarty, M. Upward, P. Beton, Review of Scientific Instruments **71,** 1698 (2000)
3. G. Binnig, Ch. Gerber, E. Weibel and H. Rohrer, Pys. Rev. Lett. **50,**120 (1983)
4. D.P. DiLella, J. H. Wandass, R. J. Colton and C. R. K. Marrian, Rev. Sci. Intrum. **60** 997 (1989)
5. P. Schroer and J. Becker, IBM J. Res. Dev. **30**, 543 (1986)
6. C. Y. Nakakura, V. M. Phanse, G. Zheng, G. Bannon, E. I Altman, K. P. Lee, Rev. Sci. Instrum. **69**, 3251 (1998)
7. R. Piner and R. Reifenbeger Rev. Sci. Instr. **60** (10) 3123, (1989)
8. D. R. Baselt, S. M. Clark, M. G. Youngquist, C. F. Spence, J. D. Baldeshwieler, Rev. Sci. Intrum. **64,** 1874 (1993)
9. T. M. H. Wong and M. E. Welland, Meas. Sci. Technol. **4** 270 (1993)
10. Park Scientific Instruments produce a range of microscopes for different applications, all of which are controlled by the same basic control electronics. Several of the microscopes can be operated as different types of SPM.
11. D. W. Pohl, IBM J. Res. Dev. **30**, 417 (1986)
12. S-I. Park and C. F. Quate, Rev. Sci. Instrum. **58**, 2004 (1987)
13. Blue Wave systems – formerly Loughborough Sound Images.
14. A proprietary expansion system developed by Loughborough Sound Images.
15. Earlier image processing software described on pages 47 –50 in PhD thesis "Fullerenes, transition metal clusters and organometallics on silicon

surfaces" by M.D. Upward to aid analysis of images obtained with commercial UHV STM system in ref. 1.

16. B.J. Cox, Object Oriented Programming, Addison-Wesley Publishing (1986)
17. Supplied by Thermomicoscopes, formally Topometrix.
18. E. Louis, F. Flores and P. M. Echenique, Phys. Scr. **37**, 359 (1988)

Chapter 4

Manipulation of C_{60} on the Si(100)-2x1 surface

In this chapter an experimental investigation of room-temperature STM-induced movement of C_{60} adsorbed on the Si(100)-2x1 surface is presented. Evidence for an attractive mode of interaction, not previously observed at room temperature is given. In addition, a detailed investigation of a second, repulsive, mode of interaction is discussed, including the effect that changes in sample bias and feedback response have on repulsive manipulation events. An explanation of the software routines used to perform the manipulation experiments is also presented.

4.1 Introduction

The processing power of commercial microprocessor chips has exponentially increased over the last thirty years. This is clearly demonstrated by an observation-based rule called Moore's law [1], proposed in 1965. Moore's law states that the transistor count and processing speed of the newest commercial microprocessor chips doubles approximately every eighteen months. Figure 4.1 shows how actual values of transistors per chip for commercial processors agree surprisingly well with Moore's law, even thirty years on.

As the number of transistors on a microprocessor chip increases, the dimensions of features on each chip must decrease for the size of the chip to stay constant. As a result, it has been predicted that as early as 2005 linewidths will approach dimensions of 650Å [2], and that by 2025 this will have decreased to 30Å [3]. Such features are comparable in size to the dimensions of a single molecule.

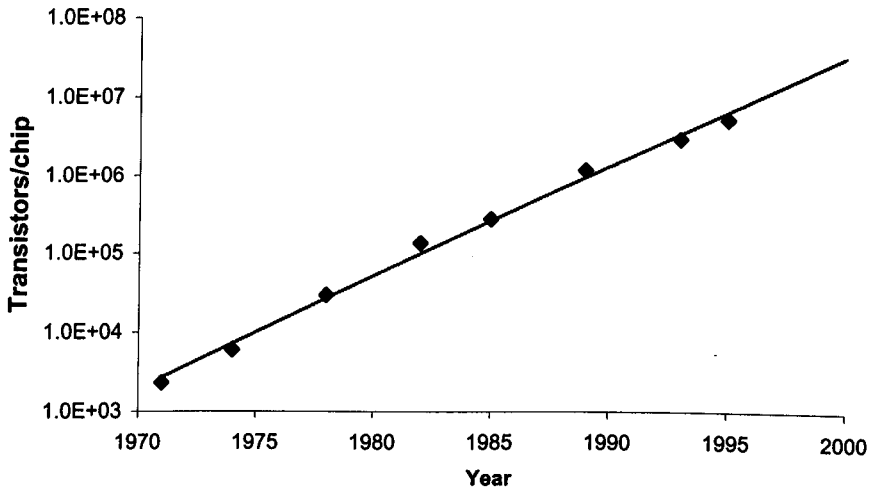

Figure 4.1 *Demonstration of Moore's Law over a 30-year period*

Formation of molecular-scale nanostructures, presents numerous technological problems. For example, current photolithography techniques have a resolution limit of 0.1 μm imposed by the wavelength of light used in the process. To overcome this, alternative approaches to feature formation are required. Methods such as self-assembly [4] and atomic holography [5] have been proposed, along with SPM-induced molecular positioning [6]. In this chapter, a method of controlled molecular positioning utilising tungsten STM tips is investigated, motivated by the potential use in nanostructure formation.

4.2 Controlled movement of individual atoms and molecules

In 1990, Eigler and Schweizer demonstrated that the tip of a STM could be used to position individual Xe atoms on a Ni surface in a controlled manner [6]. Xe atoms were dragged one by one to desired locations by bringing a STM tip down on top of an adsorbed atom and then slowly moving the tip parallel to the surface (see next section for a more detailed description). The atom was found to follow the tip until it was retracted, leaving the atom bound to the surface at a new location.

This attractive interaction can be understood if the potential between an isolated atom and a STM tip is considered. Such a potential, shown in figure 4.2, takes a form similar to the Lennard-Jones potential found between two isolated atoms. Primarily consisting of two terms - a short-range repulsive term proportional to r^{-12} and a weaker long-range attractive term proportional to r^{-6}, where r is the separation. The repulsive term arises from electron-electron interactions, while the attractive term is a result of van der Waals interactions.

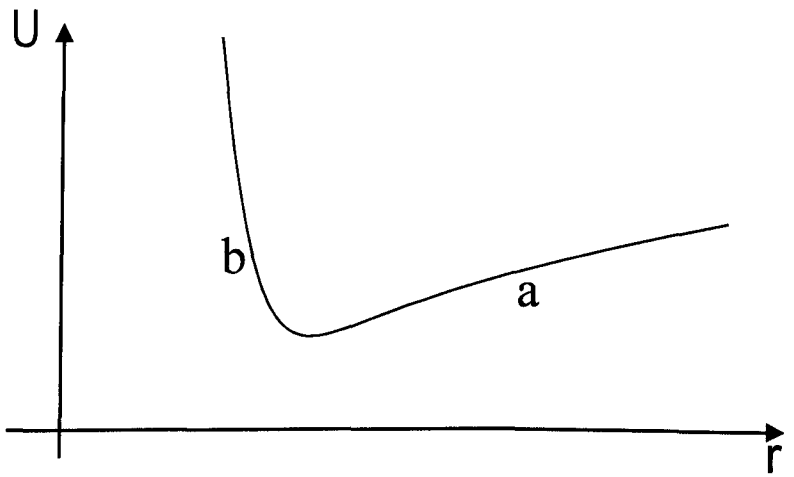

Figure 4.2 *Potential, U, between a STM tip and an isolated atom separated by a distance r. Region marked "a" exhibits attractive interaction, while "b" is repulsive in nature.*

If the tip-sample distance is located in the region marked "a" in figure 4.2, the atom will be subjected to an attractive force towards the tip, as the interaction force is proportional to the energy gradient. However, if the tip-atom separation in decreased to "b", a repulsive force occurs. In the case of an atom adsorbed on a substrate, the atom can be moved across the surface by the tip provided the interaction is greater than the diffusion barrier. If the attractive interaction is large enough, an atom can be dragged along a surface for an almost arbitrary distance. Alternatively, the atom could be pushed across the surface if the tip-atom separation is sufficiently reduced. A number of papers [7-9] have been published modelling such situations, which have proved to be in reasonable agreement with the observations of Eigler & Schweizer.

Further work by the Eigler's group [10] also showed that surface electrons could be confined within corrals formed by adatoms positioned with a STM

tip. These corrals exhibit novel quantum mechanical effects such as electron standing waves [10] and quantum mirages [11]. All their work to date has been performed at 4.2K to prevent thermal diffusion of the Xe atoms due to the low diffusion barrier of Xe on Ni(100).

Ultimately, if STM induced nanostructure formation is to be used to produce molecular electronic circuits it is desirable that Eigler and Schweizer's experiments be extended to room temperature. For this to be possible, thermal diffusion of the adsorbate must be suppressed by stronger substrate-adsorbate interaction. However increased substrate-adsorbate interaction also results in a larger barrier for STM induced movement. At present, only a small number of substrate-adsorbate combinations have been found with an appropriate diffusion barrier to permit room temperature manipulation whilst preventing thermal diffusion.

Gimzewski and co-workers [12,13] theoretically and experimentally investigated a range of molecules and surfaces potentially suitable for molecular manipulation at room temperature. They successfully demonstrated controlled manipulation of porphyrin-based molecules [13] and C_{60} [12] on Cu(100) and Cu(111) surfaces. Other groups [14-18] also found C_{60} and related fullerene molecules (e.g. $C_{59}N$) to be particularly suitable for room temperature manipulation, due to their near-spherical shape. A spherical molecule presents a large interaction cross-section to the STM tip, whilst providing a small area of interaction with the surface.

In addition to operation at room temperature, it is also desirable for nanostructures to be formed on non-metallic substrates. This would permit measurement of the electronic properties of nanostructures and could ultimately be used in the construction of molecular electronic circuits. Use of a metallic substrate would result in conduction through the substrate, masking the properties of a nanostructure. Semiconducting or insulating substrates eliminate this problem, however insulators are unsuitable for use in scanning tunnelling microscopy, leaving semiconductors as the only viable option.

Silicon is the natural choice for a semiconducting substrate as it is already widely used in the semiconductor industry. Early manipulation experiments on semiconductors at room temperature used the Si(111)-7x7 surface, with C_{60} molecules as adsorbates. Maruno et al [14] demonstrated the manipulation of C_{60} by performing a STM scan with the tip held close to the surface and the feedback loop effectively turned off. However, the movement was not controlled enough to create specific nanostructures. Work by Beton and co-workers [15-18] demonstrated *controlled* manipulation of C_{60} on silicon, first on the Si(111)-7x7 surface [15,16] and later on the Si(100)-2x1 surface [17,18]. Far greater control was achieved on Si(100)-2x1 as surface anisotropy resulted in a directional barrier to displacement. A lower barrier was observed parallel to the Si dimer rows than was observed perpendicular to them (see chapter 2 for a description of the Si(100)-2x1 surface).

To further improve control of molecular manipulations, a clear understanding of tip-adsorbate interactions is required. The exact nature of this interaction is complex and not yet known fully, as very little data acquired *during* the manipulation process has been available. To the author's knowledge, Bartels et al [19] are the only group to have published data acquired during individual manipulation events. In their experiments, performed at 30K, a selection of different atoms and dimers on Cu surfaces were manipulated whilst recording tip position. Analysis of the tip height data showed three modes of movement, dependent on tunnelling parameters; one attractive and two repulsive. The work presented in this chapter shows data similar to Bartels et al [19] at room temperature, rather than 30K, and is intended to provide a basis for later theoretical studies.

4.3 Previous manipulation procedures

As the discussion above shows, controlled molecular manipulation has been performed on a range of different surfaces and adsorbates. The basic procedure resulting in manipulation of the adsorbate was similar in each case.

Eigler and Schwiezer [1] used a custom built low temperature STM and the manipulation procedure shown in figure 4.3(a). First an adsorbed Xe atom was located through conventional imaging, and then the STM tip was positioned directly above it. By increasing the tunnelling current, the tip was moved towards the atom resulting in an increased tip-atom interaction. Motion could then be initiated by moving the tip across the surface at a rate of ~4Å per second, as the atom was found to follow the trajectory of the tip. To cease manipulation the tunnelling current was reset to its original value, retracting the tip and leaving the atom bound to the surface.

Gimzewski et al [12,13] also used a custom-built STM for room temperature molecular manipulation experiments, implementing the procedure shown in figure 4.3(b). A control system, developed in collaboration with Welland et al, allowed positioning of the STM tip under mouse control. Initially an image of the area containing the molecule to be manipulated was acquired. The tip was then positioned *next to*, rather than directly on top of, the molecule to be moved. The location of the tip was chosen such that it was placed behind the molecule in order to *push* it. Next the tunnelling parameters were modified to move the tip closer to the surface. The tip was then displaced a given distance along the intended direction of motion of the molecule, and subsequently retracted. A second image was then acquired to determine the result of the manipulation procedure.

The manipulation procedure employed by Bartels et al [19] was virtually identical to that performed by Gimzewski, shown in 4.3(b). Bartels et al used a custom built STM, operating at 30K. The only significant difference in procedure was that tip-height data was collected during the manipulation.

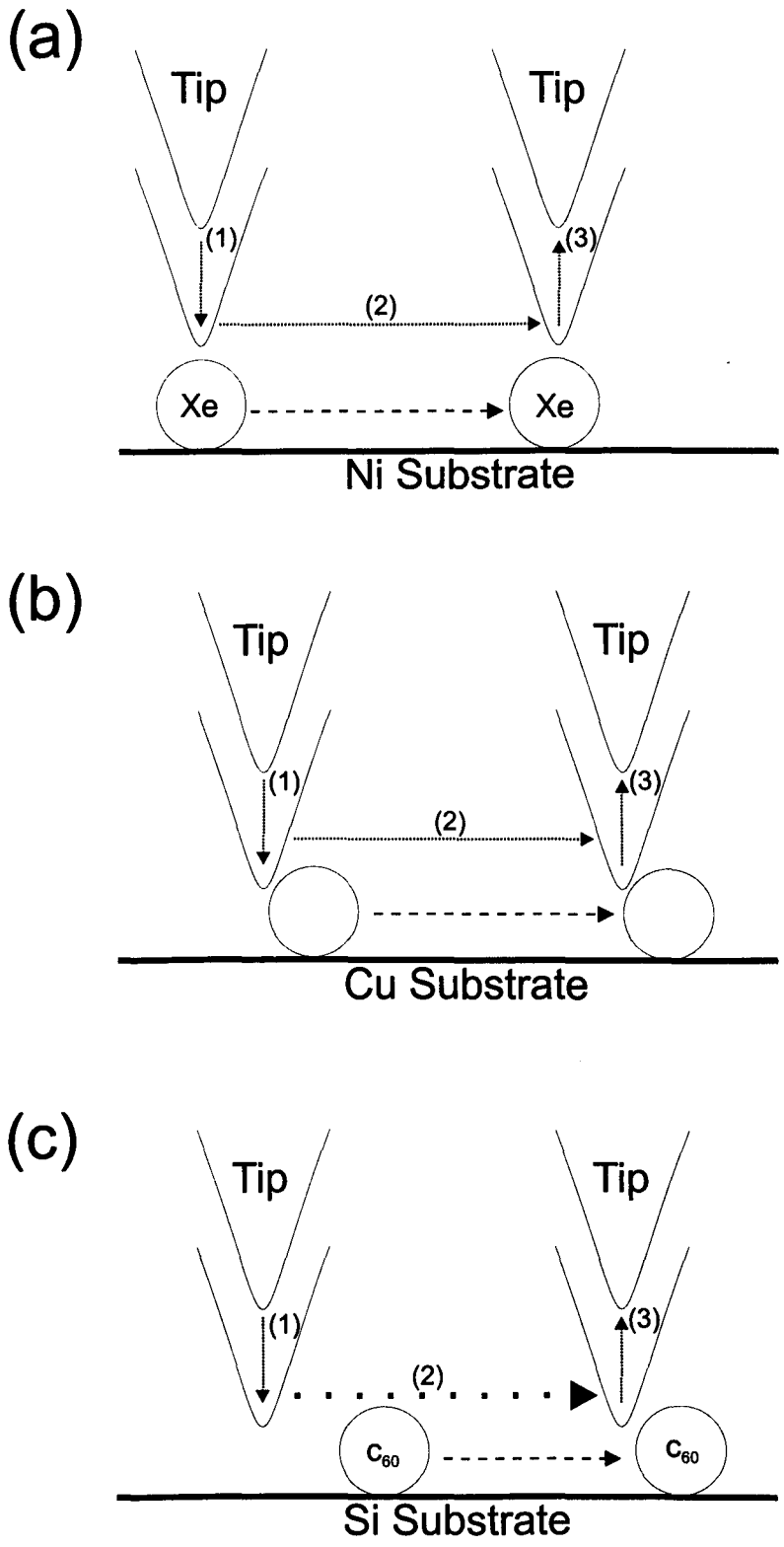

Figure 4.2 *Examples of manipulation procedures. (a) method used by Eigler & Schwiezer, (b) method emplyed by Gimzewski et al. and Bartles et al. The tip moves smoothly along path (2) (c) method used by Beton et al. The tip moves in discrete steps of 6Å along path (2).*

Our research group (Beton et al [15-18]) are the only group to date to have implemented a manipulation procedure using a commercial STM and controller [20]. The controller includes a basic macro language that enables a degree of positional control of the tip. However, limitations of the macro system prevent increments of tip displacement less than 6Å, thus we were unable to reproduce the slow, controlled motion used by other groups. In addition, it is not possible to collect data during the manipulation. Figure 4.3(c) shows the manipulation procedure employed. As in other manipulation experiments, an initial image was acquired. The tip was then positioned next to the molecule to be moved by repeatedly scanning a small area and moving the scan window until the centre of the scan was located at the intended initial tip position. The tunnelling parameters were then modified to bring the tip closer to the surface and the manipulation macro was initiated. The macro moved the tip along the X or Y-axes of the scan through a distance of ~30Å in 6Å steps, with the digital feedback loop updated after each step. At the end of the procedure the tip was retracted and a final scan was acquired to determine the result of the manipulation.

4.4 Extension of existing manipulation procedures

The use of a commercial STM controller in manipulation experiments imposed severe limitations on the level of control of tip position. In order to improve the manipulation process, the custom-built controller described in chapter 3 replaced the commercial STM controller. This enables complete control over the STM tip, and the ability to write specific manipulation software routines. These routines allow variation of parameters that control tunnelling conditions and feedback response. In addition to the improved tip control, the new controller is also capable of recording both the tunnel current and tip-height during the manipulation procedure – an essential requirement if further understanding of the tip-adsorbate interaction is to be gained.

The modular nature of the control software described in chapter 3 made it very simple to write additional functions for molecular manipulation experiments. Routines were added to perform the following manipulation procedure: Firstly, as with all previous manipulation experiments, a suitable area of a sample was located and a scan of the region acquired. For the results presented in this thesis, the first scan was always chosen to be ~300x300Å^2. Next a line was drawn on the scan to define the intended trajectory of the tip during the manipulation procedure. This line was limited to be parallel to the primary axes of the scan, to ensure a linear tip trajectory during manipulation (see chapter 3 for an explanation). However, the ability to rotate the scan window in hardware allowed the line to be defined in any orientation relative to the sample.

Once a line had been defined, the tip was then repeatedly scanned over it, using standard imaging parameters (typically –3V, 0.1nA). The tip height along the line was sent back to the PC and displayed, to facilitate fine adjustment of the line position to ensure correct location of the line and to reduce the effects of piezoelectric drift and creep. In this way, it was possible to locate the line directly over a chosen feature on the scan (e.g. an individual C_{60} molecule).

At this point, a range of parameters defining the tunnelling conditions (i.e. sample bias and tunnel current) and feedback response were set, and the manipulation procedure initiated. Feedback parameters were defined in chapter 3, however to recap they are: *settle, average,* and *interpoint.* For the purposes of manipulation, *interpoint* has been replaced by an equivalent parameter called *step-size.* During scanning, *interpoint* is used to determine the number of non-imaging points between each image point. This can also be considered as defining the distance moved between feedback updates. During manipulation experiments, data is collected throughout the procedure, so non-imaging points are irrelevant. The displacement between each measurement and feedback update is important, and can be set by the *step-size* parameter.

Figure 4.4 shows the relationship between *settle, average* and *step-size.* Lateral tip position is plotted on the Y-axis, and time in feedback cycles is plotted on the X-axis. The tip is moved laterally in discrete units determined by *step-size.* Between each step the lateral position is maintained for a period determined by the sum of *settle* and *average.* The value of *settle* defines the number of feedback cycles performed immediately after a lateral tip displacement, prior to a period of data collection (defined by *average*). No data is acquired during the *settle* period to allow the system to stabilise after the lateral tip displacement. During the period defined by *average*, the tip-height and tunnel current is measured and the average value is stored. It is useful to consider a total dwell time at each point, τ, given by *settle* + *average*, as there is no change in feedback function between *settle* and *average.* The only difference is in the data returned to the PC. For the experiments in this chapter only τ is considered, and *average* is kept constant at 1, so τ = *settle* + 1.

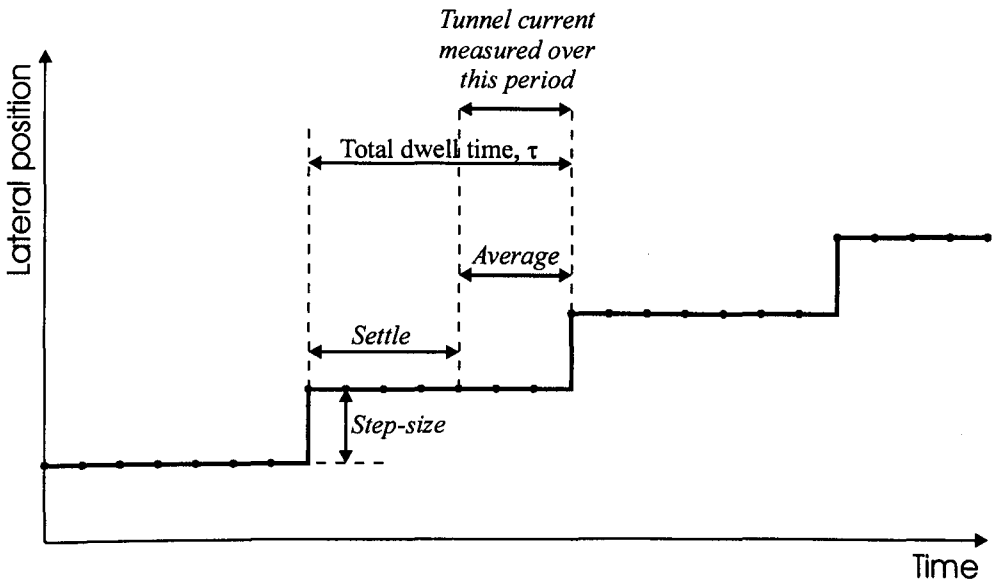

Figure 4.4 *Relationship between feedback parameters settle, average and step-size. Red dots represent feedback updates.*

Continuing the description of a manipulation procedure, once the manipulation parameters have been defined, the tip performs a series of scans along the line defined previously. It is moved forwards and backwards along the line whilst recording the tunnel current and tip-height. A completely different set of

tunnelling and feedback parameters can be set for each direction of tip motion. For example, in the convention used in this thesis, the forward motion always had parameters similar to those used when acquiring a conventional scan, while the reverse motion had parameters that may cause a manipulation event. The forward direction is defined as left to right motion, and the reverse is defined as right to left. Figure 4.5 shows a schematic of the manipulation procedure. Each forwards and backwards scan of the line was subsequently repeated a number of times specified by the user. On completion of the manipulation procedure, a second scan of the region was acquired

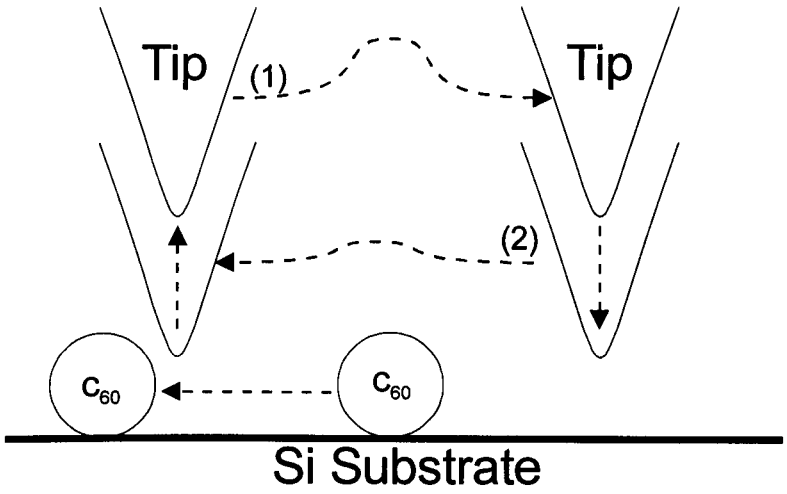

Figure 4.5 *The manipulation procedure used in this thesis. Tip is scanned backwards and forwards over a molecule with different tunnelling parameters for each direction of motion.*

To enable accurate comparisons between linescans with different feedback parameters, a facility to incrementally change parameters was implemented. This allowed the values of bias, *settle* and *average* to be independently incremented or decremented between each repetition. For example a manipulation procedure could contain ten repetitions, the first reverse scan may have a bias of -3V and each subsequent one would have a bias of .2V greater than the previous, ending with a value of -1.2V. Varying parameters in such a way meant that an identical line could be traced with a series of different parameters, giving a clear indication of their effect on the system.

4.5 Anatomy of a linescan

Two experimental investigations were performed in order to improve the understanding of room temperature molecular manipulation, using the data acquisition process described in the preceding section. The first investigation (presented in section 4.6) concentrates on the system response to a C_{60} molecule on a Si(100)-2x1 surface, and the effect of changes in feedback and tunnelling parameters on this response. The second investigation (presented in sections 4.7 and 4.8) demonstrates room temperature manipulation of C_{60} on Si(100)-2x1, and looks at the effect of changes in tunnelling and feedback parameters on the probability of manipulation. The results presented are an accumulation of different measurement sessions using several different tips and samples. Each sample and tip was prepared as described in chapter 2. To clarify explanation of the results from these two investigations, this section describes the data obtained from a typical manipulation procedure, and defines some conventions used in the discussion of the experimental results.

Earlier it was stated that a large volume of data is acquired during manipulation experiments. To quantify this statement, consider a typical manipulation attempt. During a single manipulation procedure, graphs of tip-height and tunnel current are produced for each pass of the STM tip along the manipulation line. Typically the procedure is repeated ten times, and data is acquired when the tip scans both forwards and backwards along the line. Thus a total of 2 x 2 x 10 = 40 graphs are produced for a single manipulation attempt.

To assist in the presentation of such a large volume of data within this thesis, some conventions and standard presentation methods will now be defined. Figure 4.6 shows data collected during a typical manipulation procedure. The example shown does not contain any movement of the C_{60} molecule (seen as a ~7Å protrusion in graphs A and B). It was chosen to demonstrate common features seen, without a manipulation event adding complex features to the trace. However it was acquired in an identical manner to all other linescans in this chapter.

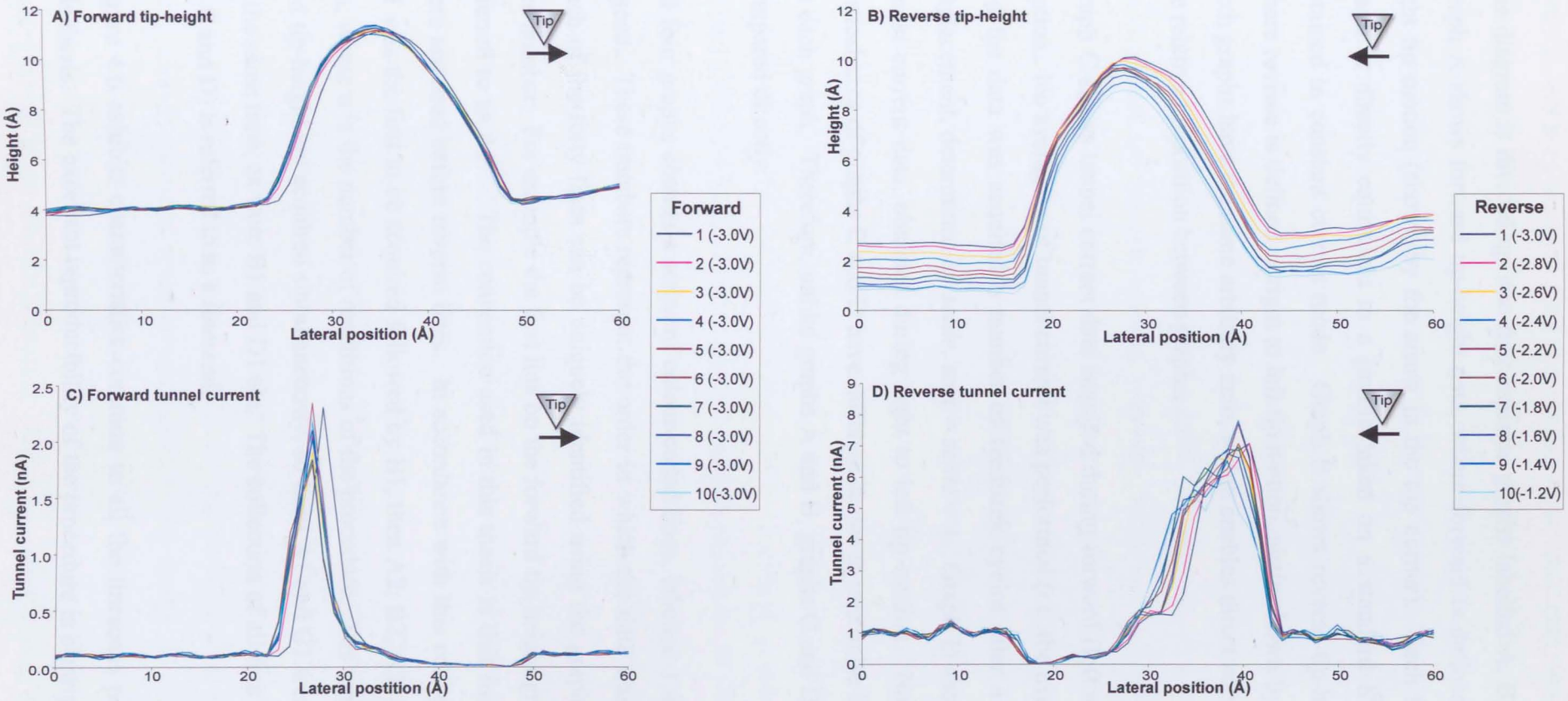

Figure 4.6 *A typical linescan. Forward parameters: I=0.1nA, V=-3V, Step size=1.1Å, τ =21*
Reverse parameters: I=1nA, V=-3V to -1.2V, step size=1.1Å, τ=21

The diagram is divided up into four separate graphs labelled A, B, C and D. Graph A shows forward tip-height data, where forward is defined as left to right tip motion (shown by the arrow in the top corner). Each line on the graph is directly equivalent to a profile taken on a standard STM image obtained in constant current mode. Graph B shows reverse tip-height data, where reverse is defined as right to left tip motion, again shown by an arrow. Both graphs have the same arbitrary zero, which enables direct comparison of the relative tip position between graphs.

Graph C shows tunnel current data acquired during forward (left to right) tip motion. No averaging of tunnel current was performed (i.e. the *average* = 1), and the data was acquired a number of feedback cycles after a lateral tip displacement, determined by *settle,* so τ = *settle* + 1. Graph D shows reverse tunnel current data, obtained during right to left tip motion. Note that the vertical axes of graphs C and D have different scales to maximise the features on each graph. Therefore, unlike graphs A and B, graphs C and D cannot be compared directly.

All four graphs contain a series of colour-coded lines, labelled 1 to 10 in the legend. These numbers represent the order in which the data was collected. Each of the forty lines can be uniquely identified using the graph letter and line number. For example the first line on the forward tip-height graph can be referred to as A1. The convention used in this thesis is that forward lines were acquired before reverse lines. In accordance with this convention, line A1 was the first to be acquired followed by B1, then A2, B2, A3, B3, ... An, Bn, where n is the number of repetitions of the procedure. The tunnel current and tip-height are acquired simultaneously, so lines A1 and C1 were acquired at the same time, as were B1 and D1 etc. The collection of all four graphs (A, B, C and D) is referred to as a *linescan.*

Figure 4.6 exhibits characteristics common to all the linescans presented in this thesis. The excellent reproducibility of the procedure is clearly shown by

graph A. All lines on graph A lie virtually on top of each other, apart from A1 which is offset by ~1Å. This offset may be due to piezoelectric creep (see section 4.5.1 for a discussion of errors), as it is observed in every linescan. To avoid errors in the results, line A1 is not used when measuring lateral molecular displacements.

A comparison between graphs A and B shows the tip was initially positioned ~1.2Å closer to the surface in graph B than in graph A (compare A1 and B1), and was displaced further towards the surface between each repetition. These displacements are due to changes in tunnelling parameters. All lines on graph A were acquired using I = 1nA and V = -3.0V, whereas each line on graph B had different tunnelling parameters. Line B1 was acquired with I = 1nA and V = -3.0V. Comparison of lines A1 and B1 shows an order of magnitude change in tunnel current (0.1nA to 1nA) results in ~1.2Å change in tip-height. Subsequent lines on graph B have incrementally higher sample biases (indicated by the value in brackets on the legend), from –3.0V in B1 to –1.2V in B10. It is clear from graph B that a decrease in sample bias results in a displacement towards the surface. This will be discussed in more detail in section 4.6.1. Note that there is also a lateral displacement of ~5Å between graphs A and B. This is thought to be caused by a combination of piezoelectric hysteresis and limitations of the digital feedback loop, and is currently unavoidable.

It is interesting to note that graph C is far from featureless (which it should be if the feedback loop were perfect). The current remains relatively constant at 0.1nA whilst the tip traverses the Si surface, however when the tip encounters the C_{60} molecule a sharp increase in current is observed. This is a manifestation of the finite temporal response of the feedback loop, resulting in a decreased tunnelling gap and therefore increased current. The problem is exacerbated by the discrete nature of the lateral tip position. The tip is moved 1.1Å laterally between measurement points. This results in the tip being temporarily positioned too close to the molecule before the feedback response adjusts the z position. This kind of tunnel current error occurs whenever a large gradient in the surface is present. A similar effect is seen on the other

side of the molecule, this time resulting in a decrease in tunnel current. Tunnel current spikes and troughs like these are also likely to occur during normal constant current scan acquisition. However, the effect may be less pronounced if non-imaging points are used when moving between imaging points. A 300Å scan with 16 non-imaging points between each imaging point, would have a step size of <0.1Å resulting in less perturbation to the feedback. In effect, the tunnel current error approaches zero as *settle* approaches infinity, or *stepsize* approaches zero.

Similar features to those observed in graph C are also seen in graph D. Whilst traversing the Si surface, the tunnel current is approximately constant at 1nA. On encountering the C_{60} molecule a peak in tunnel current is once again observed, however this time the peak is ~8nA rather than the ~2.2nA seen in graph C. The dip in current on the downward slope of the molecule is also more pronounced in graph D. The apparent additional structure in the tunnel current varies from trace to trace, and is therefore difficult to interpret (there are a few exceptions to this, which will be discussed in section 4.7).

4.5.1 Inaccuracies in measurements

Before a discussion of experimental results is presented, a brief discussion of errors is required. Linescans suffer from similar sources of noise and errors as normal scans. In particular, piezoelectric hysteresis and creep introduce uncertainties in the measurement of displacements. As mentioned previously, hysteresis in the piezoelectric scan tube causes the reverse motion of a linescan to be displaced laterally with respect to the forward motion. As a result, it is difficult to compare forward and reverse traces directly to obtain molecular displacements.

Piezoelectric creep occurs when the voltage applied to the piezoelectric tube is changed. The tube moves ~95% of the new displacement immediately, and then slowly moves the final 5% over a period of minutes [21]. This has a two-fold effect on linescans. Firstly, creep associated with moving the tip to the start of the linescan is thought to cause the entire initial forward line to be

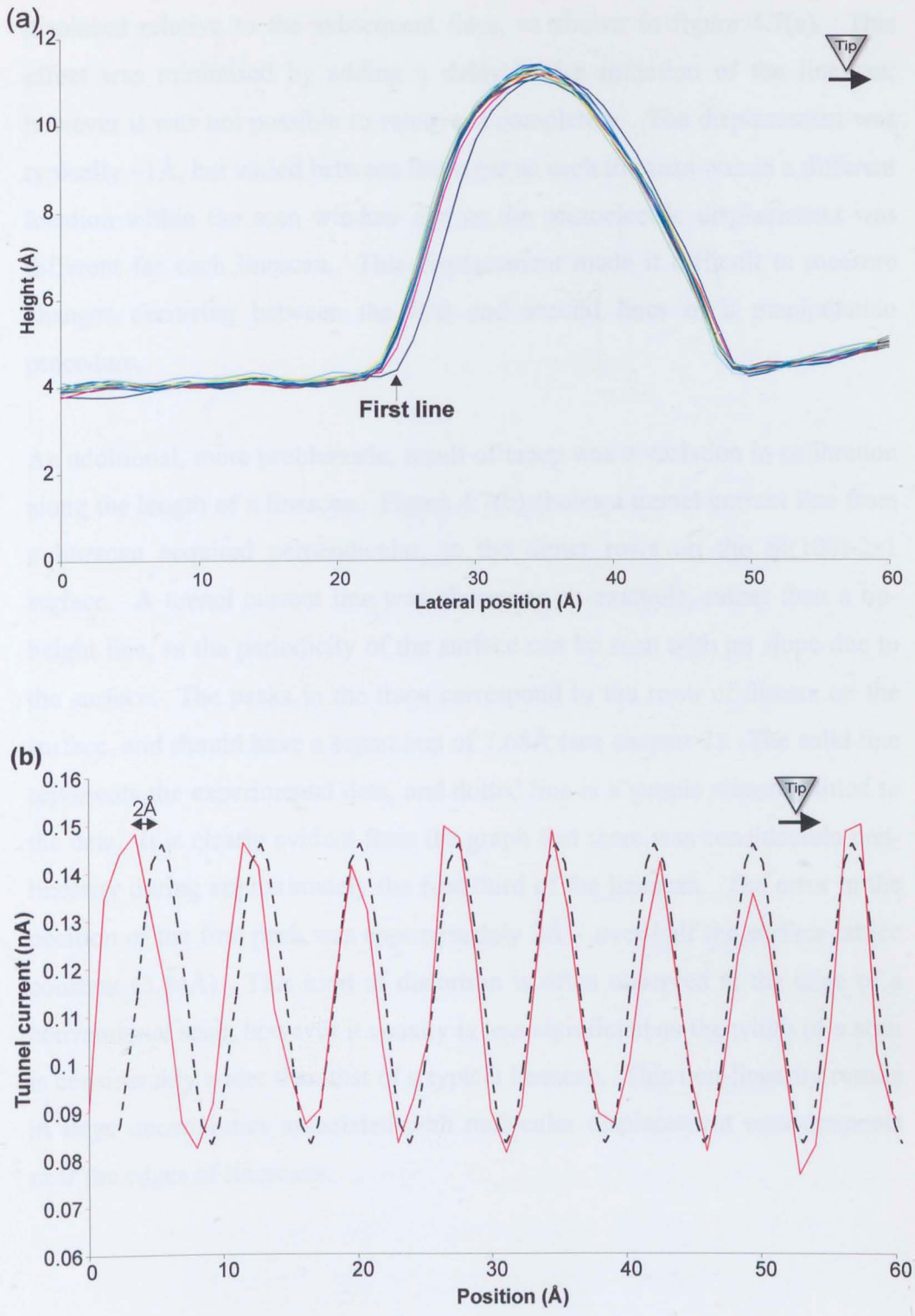

Figure 4.7 *(a) Displacement of the first line relative to subsequent lines on a linescan. (b) Non-linearity along the length of a single line.*

displaced relative to the subsequent lines, as shown in figure 4.7(a). This effect was minimised by adding a delay before initiation of the linescan, however it was not possible to remove it completely. The displacement was typically ~1Å, but varied between linescans as each linescan was in a different location within the scan window and so the piezoelectric displacement was different for each linescan. This displacement made it difficult to measure changes occurring between the first and second lines of a manipulation procedure.

An additional, more problematic, result of creep was a variation in calibration along the length of a linescan. Figure 4.7(b) shows a tunnel current line from a linescan acquired perpendicular, to the dimer rows on the Si(100)-2x1 surface. A tunnel current line was chosen as an example, rather than a tip-height line, as the periodicity of the surface can be seen with no slope due to the surface. The peaks in the trace correspond to the rows of dimers on the surface, and should have a separation of 7.68Å (see chapter 2). The solid line represents the experimental data, and dotted line is a simple sinusoid fitted to the data. It is clearly evident from the graph that there was considerable non-linearity during approximately the first third of the linescan. The error in the position of the first peak was approximately 2Å – over half the surface lattice constant (3.84Å). This kind of distortion is often observed at the edge of a conventional scan, however it usually is less significant as the width of a scan is considerably wider than that of a typical linescan. This non-linearity results in large uncertainties associated with molecular displacement measurements near the edges of linescans.

4.6 Characterisation of linescan response

Now that the conventions used in the presentation of experimental results have been explained, and a typical linescan has been described, the experimental

investigation of how linescans change with variation of feedback and tunnelling parameters can be discussed. There are four user-defined parameters that directly affect the STM response: τ, *step-size,* sample bias and tunnel current. In addition, feedback gains P, I and D (see chapter 3) affect the response of the system, but these are optimised during scanning and therefore are not modified during manipulation procedures. The effect of changes in sample bias and tunnel current are considered in the next section, followed by discussions of τ and *step-size* in the following sections.

4.6.1 Variation of sample bias and tunnel current

The example linescan given in section 4.5 showed that a variation in bias voltage resulted in a vertical displacement of the tip. To more clearly illustrate this voltage dependence, the average tip displacement was measured for a range of voltages. Linescans in which the sample bias was ramped between reverse traces, as in the previous example, were analysed. The average tip displacement during each reverse trace was measured relative to the forward trace (which was always acquired using –3.0V and 0.1nA). By measuring displacements on a number of linescans, displacements for a range of bias and tunnel current values were measured. To ensure consistency, the displacements were only measured on areas of the Si surface, not over any adsorbates. Figure 4.8 summarises the results obtained. Each curve on the graph represents relative displacement versus sample bias for a different value of tunnel current. The more negative the value of displacement, the closer the tip to the surface. All the lines follow approximately the same shape, which is a general downward trend with a slight inflection at a bias of -2.2V. Note also that, in general, an increase in tunnel current resulted in a shift of the entire curve towards the surface.

For analysis of the manipulation results it would be useful to know how far the STM tip is displaced towards the surface when a translation of the molecule occurs. This can be calculated if a displacement/voltage ratio is known. To facilitate this a linear approximation to the lines in figure 4.8 was calculated,

resulting in a gradient of ~0.9Å/V. Note that this is only a rough approximation, and will only apply over a limited range. It holds for sample biases between -3.0V and –1.2V, but may deviate outside of this range. It also holds for tunnel currents between 0.2nA and 0.7nA, as it appears to be independent of tunnel current within this range. Using this displacement/voltage ratio, predictions can be made regarding the position of the STM tip for a given voltage.

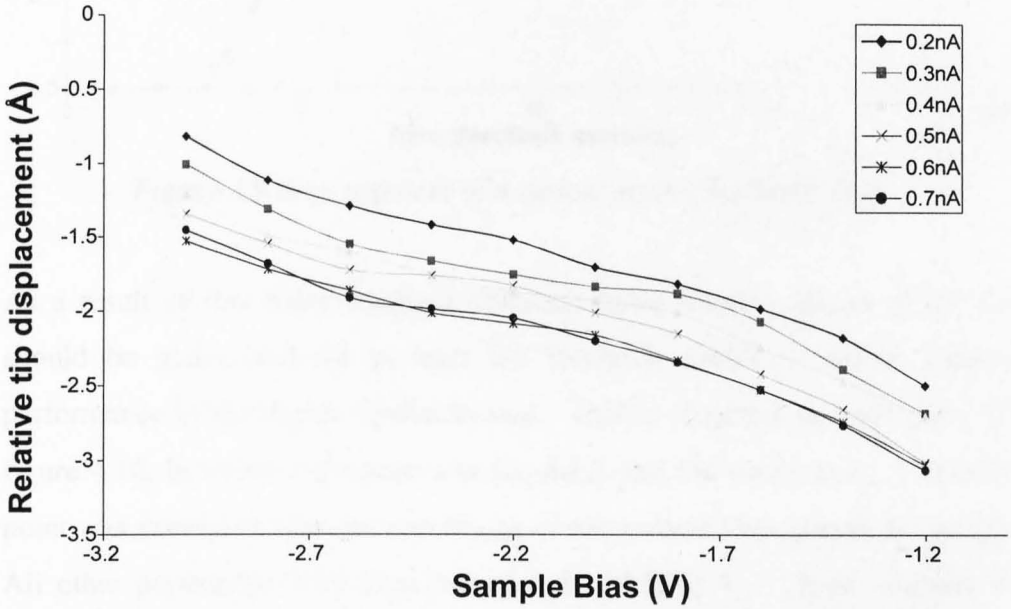

Figure 4.8 *Graph of tip Z position as a function of sample bias for a range of tunnel currents.*

4.6.2 Variation of dwell time, τ

Moving on now to consider dwell time, Wong and Welland [21] observed that a typical STM digital feedback loop has a 0-90% rise time of approximately ten cycles when responding to a step change in tunnel current. Figure 4.9 shows a schematic, taken from their paper, of the response of a digital feedback loop to a unit step. Note that although a 90% rise occurs in ~10 feedback cycles, the remaining 10% takes a further 5-7 cycles. The initial delay of 3 feedback cycles is a result of DAC/ADC sampling times, software delays and the rise time of the piezoelectric scan tube.

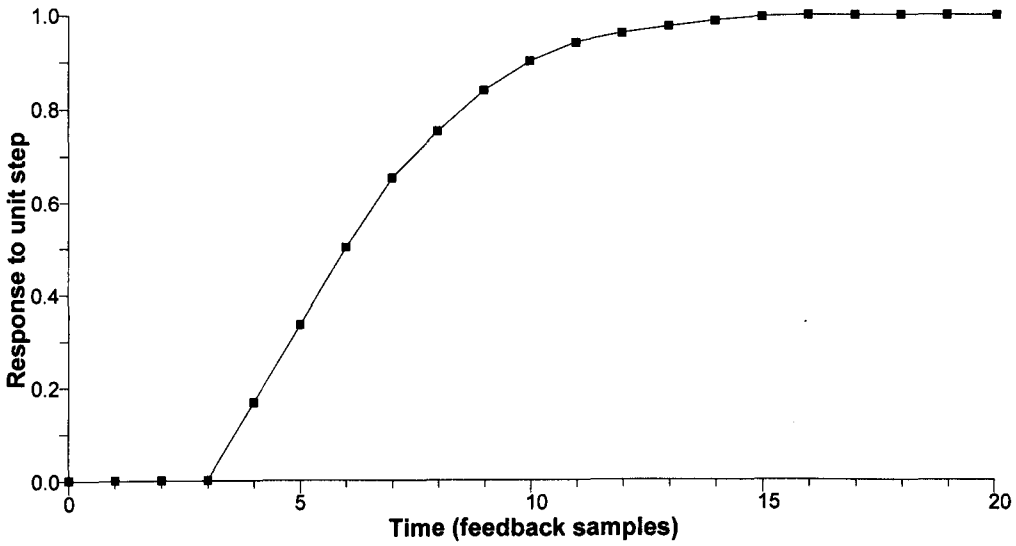

Figure 4.9 *Step response of a typical digital feedback loop*

As a result of this finite feedback response time, lateral position of the tip should be maintained for at least ten feedback cycles to ensure correct performance of the digital feedback loop. This is elegantly demonstrated by figure 4.10, in which a linescan was acquired, and the dwell time, τ, at each point was decreased between repetitions of the reverse line (graphs B and D). All other parameters were kept constant (I = 0.1nA, V = -3.0V, stepsize = 1.1Å) and were the same for both directions. All forward lines were acquired with a dwell time of 21 feedback cycles. Decreasing the dwell time at each data point had the effect of reducing the response of the system, so the feedback became less and less effective. As τ was decreased from 21 to 10 cycles (lines D1 to D12) the tunnel current spike, observed when the tip meets the C_{60} molecule, increased from ~1nA to ~2.5nA. However, the tip-height curves (B1 to B12) only exhibited small progressive displacements over this range.

At values of τ less than ten feedback cycles (B13 to B15), a considerable change in response is observed. The initial gradient of tip trajectory on encountering the molecule is reduced significantly between each successive line. This agrees well with figure 4.9, since below 10 feedback cycles the feedback loop corrects less than 90% of any error caused by the lateral

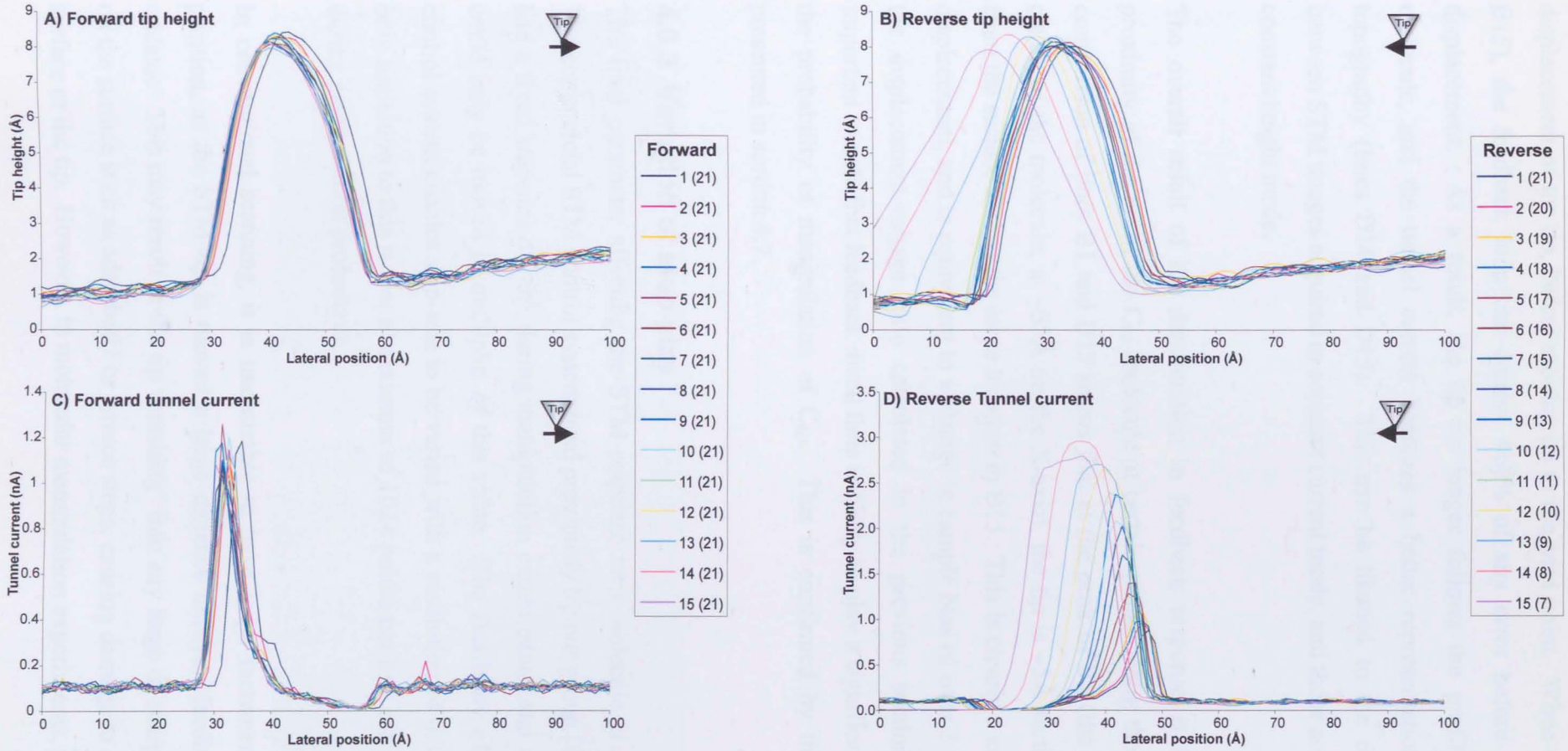

Figure 4.10 *The effect of dwell time, τ, on system response. Values in brackets show dwell time in feedback cycles for each line. Forward parameters: I=0.1nA, V=-3.0V, step size=1.1Å, τ=21.Reverse parameters: I=0.1nA, V=-3.0V, step size=1.1Å, τ=21 to 7.*

displacement of the tip, before moving on to the next point. When τ=7 (line B15), the feedback loop can correct <60% of any error before the next displacement. As a result, the tip no longer follows the profile of the molecule, and the tunnel current becomes a better representation of the topography (lines D14 and D15). This can be likened to the difference between STM images acquired in constant current mode, and those acquired in constant height mode.

The overall result of the deterioration in feedback response is increased proximity of the tip to the C_{60} molecule at certain points along the line. A comparison of lines B1 and B15 shows that at the peak of B1 (the apparent centre of the molecule, at ~35Å on the X-axis), the tip is ~5Å further away from the surface than at the same location in B15. This is clearly a significant displacement, and is equivalent to a change in sample bias of over 5.5V using the displacement-voltage ratio calculated in the previous section. It is important to note that feedback dwell time is likely to play a significant role in the probability of manipulation of C_{60}. This is confirmed by the results presented in section 4.7.

4.6.3 Variation of step-size

The final parameter affecting the STM response to a molecule is *step-size.* The commercial STM control system used previously by our group [15-18,20] had a fixed *step-size* of ~6Å during manipulation experiments, and so the tip could only be moved in multiples of this value. The flexibility of the new control system enables *step-size* to be varied with a resolution of 0.07Å. The only limitation to this is that a maximum of 1024 points per line can be stored during manipulation procedures.

In conventional scanning, it is undesirable to have large increments in tip position, as the STM tip is moved a large distance between feedback loop updates. This may result in the tip "crashing" into any large or sharp features on the surface such as adsorbates or terrace steps, causing damage to either the surface or the tip. However, in molecular manipulation experiments, large

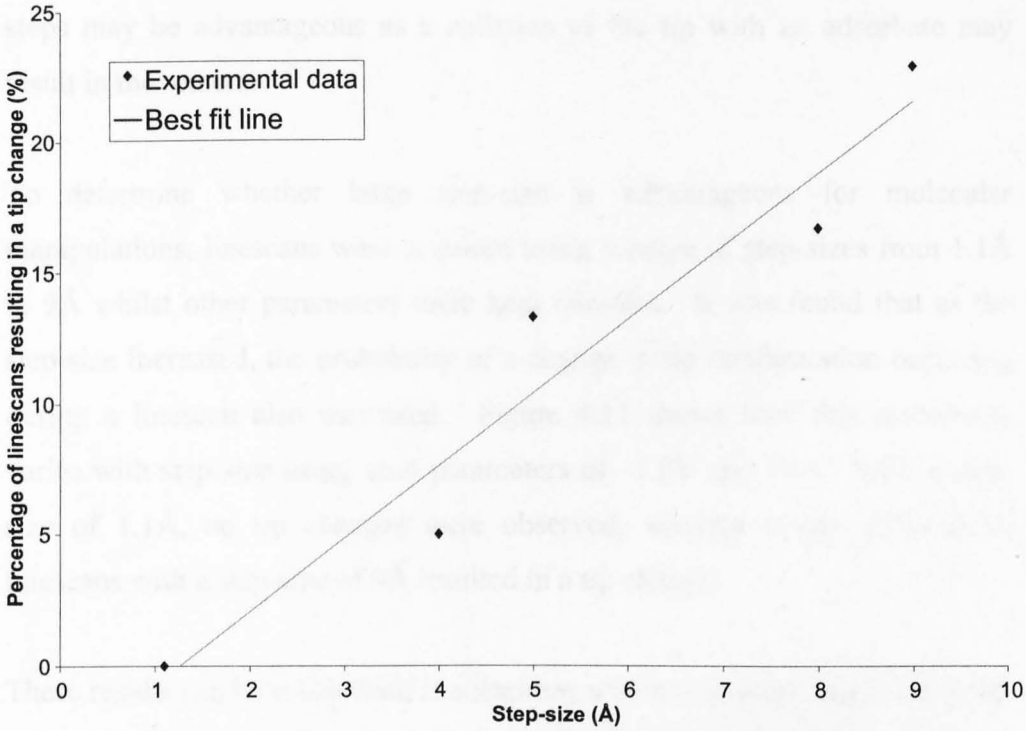

Figure 4.11 *Graph showing how the probability of a tip change increases with tip step-size.*

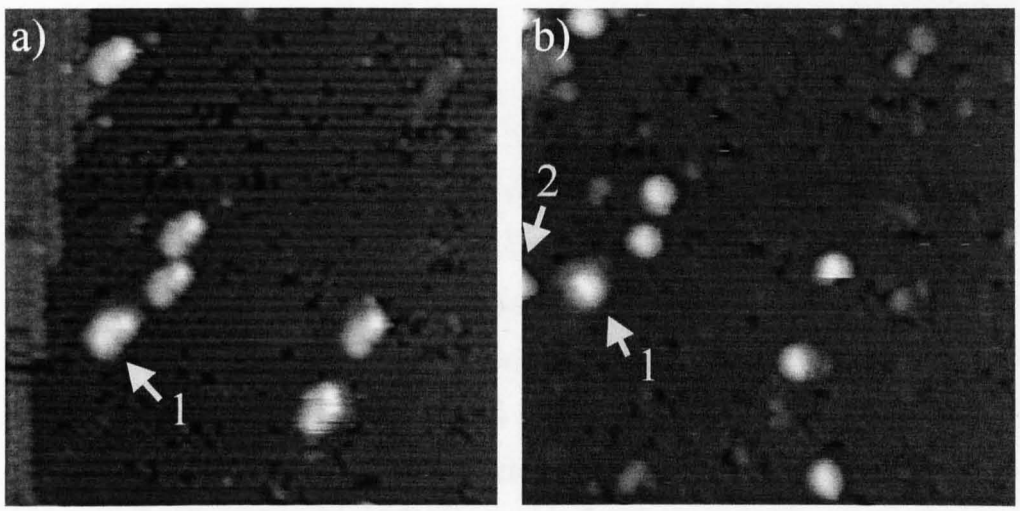

Figure 4.12 *Images showing a tip change due to deposition of a C_{60} molecule during a manipulation procedure. a) image before procedure, b) image after procedure. Arrow labeled 1 indicates subject of manipulation attempt. Arrow 2 indicates deposited molecule.*

steps may be advantageous as a collision of the tip with an adsorbate may result in movement.

To determine whether large step-size is advantageous for molecular manipulations, linescans were acquired using a range of step-sizes from 1.1Å to 9Å whilst other parameters were kept constant. It was found that as the step-size increased, the probability of a change in tip configuration occurring during a linescan also increased. Figure 4.11 shows how this probability varies with step-size using scan parameters of –1.0V and 1nA. With a step-size of 1.1Å, no tip changes were observed, whereas nearly 25% of all linescans with a step-size of 9Å resulted in a tip change.

These results can be understood if a linescan with a large step-size is analysed. Figure 4.12 shows images (a) before and (b) after the manipulation procedure shown in 4.12. The molecule marked 1 in figure 4.11 was the subject of the manipulation experiment. During the reverse motion of the procedure (graphs B and D in figure 4.13), the step-size was 9.1Å, while the standard 1.1Å was used during forward motion (graphs A and C). Although ten repetitions of the procedure were performed, only the first three are shown in figure 4.13 to improve clarity.

A comparison of lines A1 and A2 shows a displacement of the tip both vertically and horizontally occurs between the two lines. This is consistent with a change in tip configuration resulting in different tunnelling points on the tip. Note that line A2 also appears to have an additional feature not present in A1. This is most likely to be a tip artefact caused by two tunnelling points on the STM tip. Line A3 is also displaced relative to the preceding line (A2), indicating a further tip change has occurred. An example of a possible tip change is shown in figure 4.14.

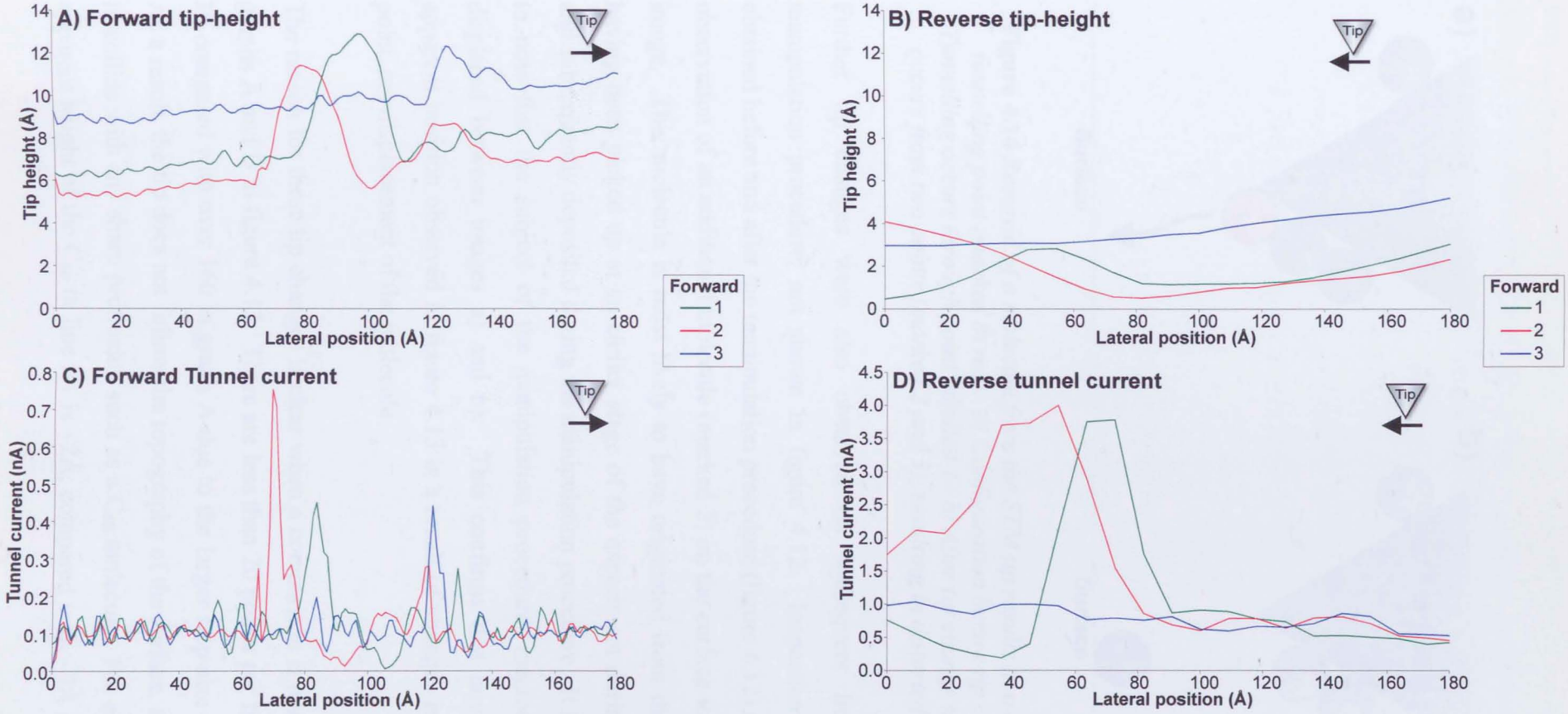

Figure 4.13 *Example of a tip change during a manipulation procedure. Forward parameters: I=0.1nA, V=-3.0V, step size=1.1Å, τ=21. Reverse parameters: I=1nA, V=-1.0V, step size=9.1Å, τ=21.*

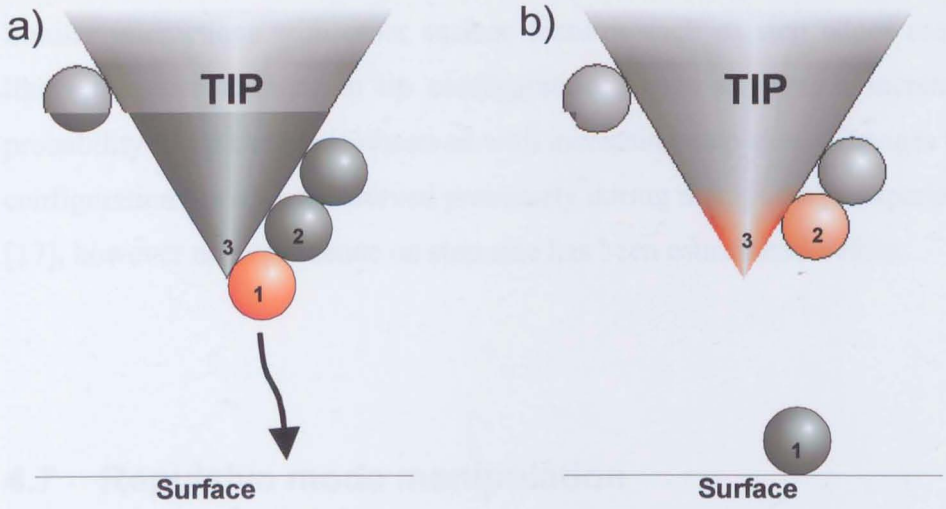

Figure 4.14 *Removal of a molecule from the STM tip results in a change in tunnelling point (marked in red). a) Configuration before tip change. Tunnelling occurs through point labelled 1. b) After tip change tunnelling occurs from two points (marked 2 and 3), resulting in distorted image.*

Further tip changes were also observed on subsequent lines in the manipulation procedure, not shown in figure 4.12. Inspection of images obtained before and after the manipulation procedure (figure 4.12) result in the observation of an additional molecule (marked 2) on the surface in the "after" image. This molecule is most likely to have originated from the STM tip, having been picked up at an earlier stage of the experiment during imaging, and subsequently deposited during the manipulation procedure. It is important to note that the subject of the manipulation procedure, marked 1, is not displaced between images a) and b). This confirms that any change in apparent position observed in figure 4.13 is a result of changes in tunnelling point, not displacement of the molecule.

The reason for these tip changes is clear when a comparison is made between graphs A and B in figure 4.13. There are less than 20 points per line in graph B, compared with over 160 in graph A due to the larger step-size in graph B. As a result, the tip does not follow the topography of the surface, and is likely to collide with any sharp protrusion such as a C_{60} molecule. For example, the apparent height of the C_{60} in line B1 is ~2Å, compared with ~7Å in A1. The

result of this would be a strong interaction between tip and molecule, resulting in either a displacement of the molecule or a change in tip configuration. Similar interactions with other surface features such as step edges are also likely to cause changes in tip configuration, hence an overall increase in probability of tip change is observed with increasing step-size. Changes in tip configuration have been observed previously during manipulation experiments [17], however no dependence on step-size has been established before.

4.7 Repulsive mode manipulation

Now that characteristics of the feedback loop have been studied, the results of its application to molecular manipulation experiments are discussed. Attempts to move many different C_{60} molecules were made, using a range of scanning and feedback parameters. Some unexpected results were obtained, including evidence for a previously uncharacterised attractive mode of movement (see section 4.8). In addition, detailed data during both attractive and repulsive manipulations was acquired, which may help in the development of a theoretical model for the tip-molecule interaction.

In previous C_{60} on Si manipulation experiments [14-18], the tip-molecule interaction has been assumed to be repulsive in nature, as opposed to the attractive interaction employed in the low temperature experiments with atoms on metal surfaces [6]. This was confirmed in experiments performed by Moriarty et al [17], where the STM tip was returned to its initial position before withdrawal, leaving the C_{60} at the extreme of the tip excursion. If the interaction had been attractive, the molecule would have been dragged back to the initial tip position.

Experiments performed using the procedure described in the preceding sections, have confirmed that movement of C_{60} can be initiated through repulsive interactions with a STM tip. Figure 4.15 shows an example of a

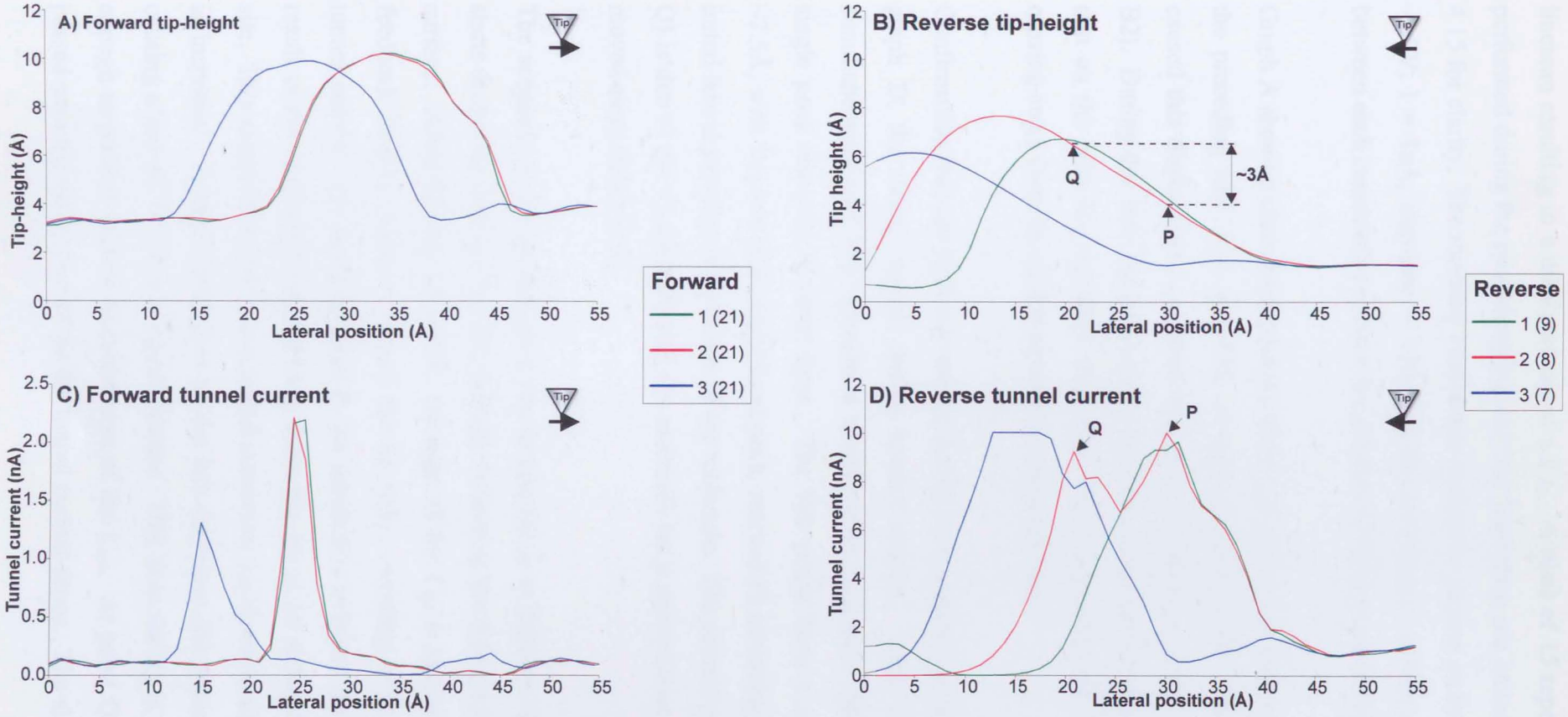

Figure 4.15 *An example of a C_{60} moved during a linescan. Molecule moves during line D2. Forward parameters: I=0.1nA, V=-3.0V, step-size=1.1Å, τ=21. Reverse parameters: I=1nA, V=-1.7V, step-size=1.1Å, τ=9 to 7. Figures in brackets indicate value of τ.*

linescan resulting in a displacement of a C_{60}. A total of 15 repetitions were performed during the procedure, but only the final three are included in figure 4.15 for clarity. The scanning parameters during the reverse motion were: V = −1.7V, I = 1nA, step-size = 1.1Å and the dwell time, τ, was decremented between each consecutive reverse line (shown in brackets on the legend).

Graph A shows a clear displacement of the C_{60} molecule in line A3, relative to the preceding lines (A1 and A2), of approximately 7.6Å. The event that caused this displacement occurred during the preceding reverse motion (line B2). During this line, the molecule is observed to be considerably wider than that on the previous repetition (line B1). This is a result of the molecule moving away from the tip during acquisition of the line.

Confirmation that the molecule moves during data acquisition can be seen in graph D, the tunnel current during reverse motion. Line D2, acquired simultaneously with B2, contains a double peak structure, rather than the single peak observed in other lines. The two peaks have a separation of ~7.5Å, with the first peak (right-hand peak, marked P) occurring close to the initial lateral position of the centre of the molecule. The second peak (marked Q) is due to the tip encountering the molecule for a second time, after it has moved away from the tip.

The sequence of events that gave rise to line D2 is as follows: The STM tip starts at the far right of line D2, initially following the topography of the Si surface. After moving left ~15Å, the edge of the C_{60} is encountered. The feedback loop is unable to retract the tip fully, resulting in an increase in tunnel current. On reaching point P, the interaction between the tip and C_{60} result in the molecule jumping away from the tip to an alternative bonding site. This results in a decrease in tunnel current as the tip-molecule separation is increased. Further movement to the left decreases the separation again, causing a second increase in tunnel current. This time the tip is retracted far enough to prevent further displacements of the C_{60}. At point Q, the tip has passed over the molecule, and so the tunnel current drops. The slow response

of the feedback loop fails to correct for the drop in tunnel current until the end of the line.

It is important to note that the drop in tunnel current between points P and Q on line D2 did not result in a displacement of the tip towards the surface (line B2). This was because the tunnel current remained well above the target value, and thus the tip continued to be retracted. Subsequently, the second encounter with the molecule occurred when the tip-molecule separation was ~3Å larger, as shown on graph B. This explains why the second encounter did not result in further displacement of the molecule, as the tip had been retracted far enough that the tip-molecule interaction was insufficient to produce movement. Multiple displacements during a single line have been observed in other linescans, and are discussed in the next section.

4.7.1 Evidence for discrete movement

An important point can be drawn from the previous section – the molecule did not move continuously along the surface, it *hopped* away from the STM tip. A second example of a manipulation event is shown in figure 4.16. In this example the molecule moved twice during a single line, again by hopping. Only the data from motion in the reverse direction is shown, but the graphs are labelled B and D for consistency. The graphs show the repetition preceding the manipulation (B1 and D1), and the manipulation line itself (B2 and D2). In this case, the manipulation was initiated through a reduction in sample bias, rather than τ, however the observed characteristics are virtually identical.

An examination of graph D shows three clear peaks in line D2, implying that the C_{60} molecule was positioned in three distinct locations during the line. An alternative interpretation would be that three molecules were present, however this is disproved by the presence of a single peak in line D1. Graph B also exhibits evidence for three positions of the molecule. Line B2 shows the apparent width of the molecule to be ~8Å wider than in B1. Two distinct changes in gradient on the right-hand-side of the molecule coincide with the

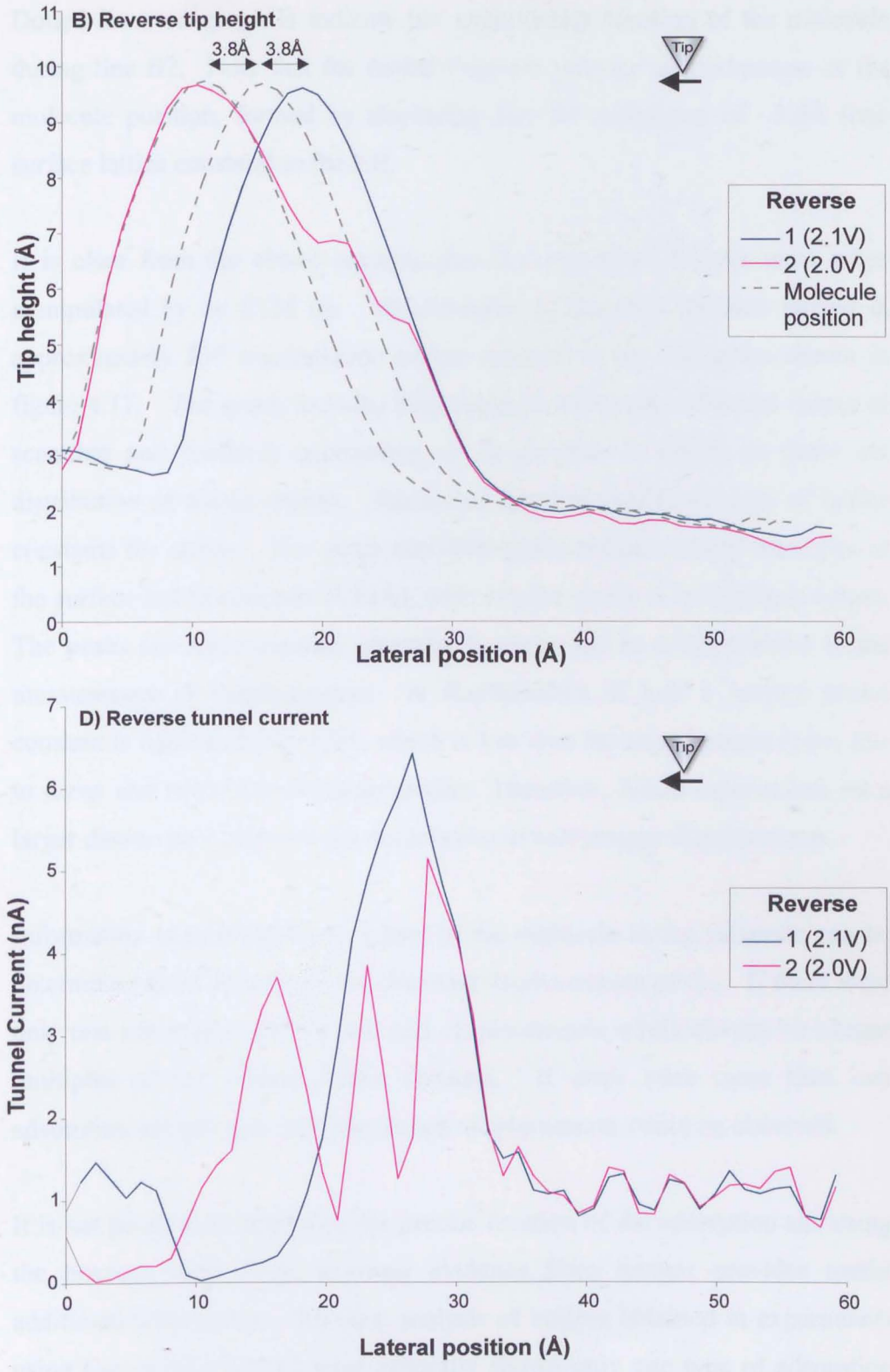

Figure 4.16 *Example of multiple displacements during a single line. Reverse parameters: I=1.0nA, step-size=1.1Å, τ=21, V= -2.1V to -2.0V.*

peaks in line D2 – the points at which the molecule hops away from the tip. Dotted lines on graph B indicate the approximate location of the molecule during line B2. Note that the dotted lines are only an approximation of the molecule position, formed by displacing line B1 a distance of ~3.8Å (one surface lattice constant) to the left.

It is clear from the above example that C_{60} moves in discrete units when manipulated by an STM tip. Measurement of the total distance moved in approximately 250 manipulation events resulted in the histogram shown in figure 4.17. The graph includes data acquired with many different values of scanning and feedback parameters, as its purpose is simply to show the distribution of displacements. The x-axis has been scaled in units of lattice constants for clarity. The graph has clear peaks around integer multiples of the surface lattice constant (3.84Å), with smaller peaks at half-integer values. The peaks are approximately gaussian in shape due to random errors in the measurement of displacements. A displacement of half a surface lattice constant is equivalent to ~1.9Å, which is less than the experimental errors due to creep and hysteresis discussed earlier. Therefore, future experiments on a larger dataset may disprove the observation of half-integer displacements.

Information concerning the bonding of the molecule to the substrate can be determined from the size of the observed displacements of C_{60}. If there were only one adsorption site per unit cell, displacements would always be integer multiples of the surface lattice constant. If there were more than one adsorption site per unit cell, non-integer displacements could be observed.

It is not possible to determine the precise location of the adsorption site using the linescan data alone, however evidence from images provides useful additional information. Previous analysis of images obtained in experiments using C_{60} on Si(100)-2x1 have generally shown only one type of adsorption site at room temperature [17,24]. This has been termed the four-dimer site, as it is located in the trough between dimer rows between four dimers, shown in

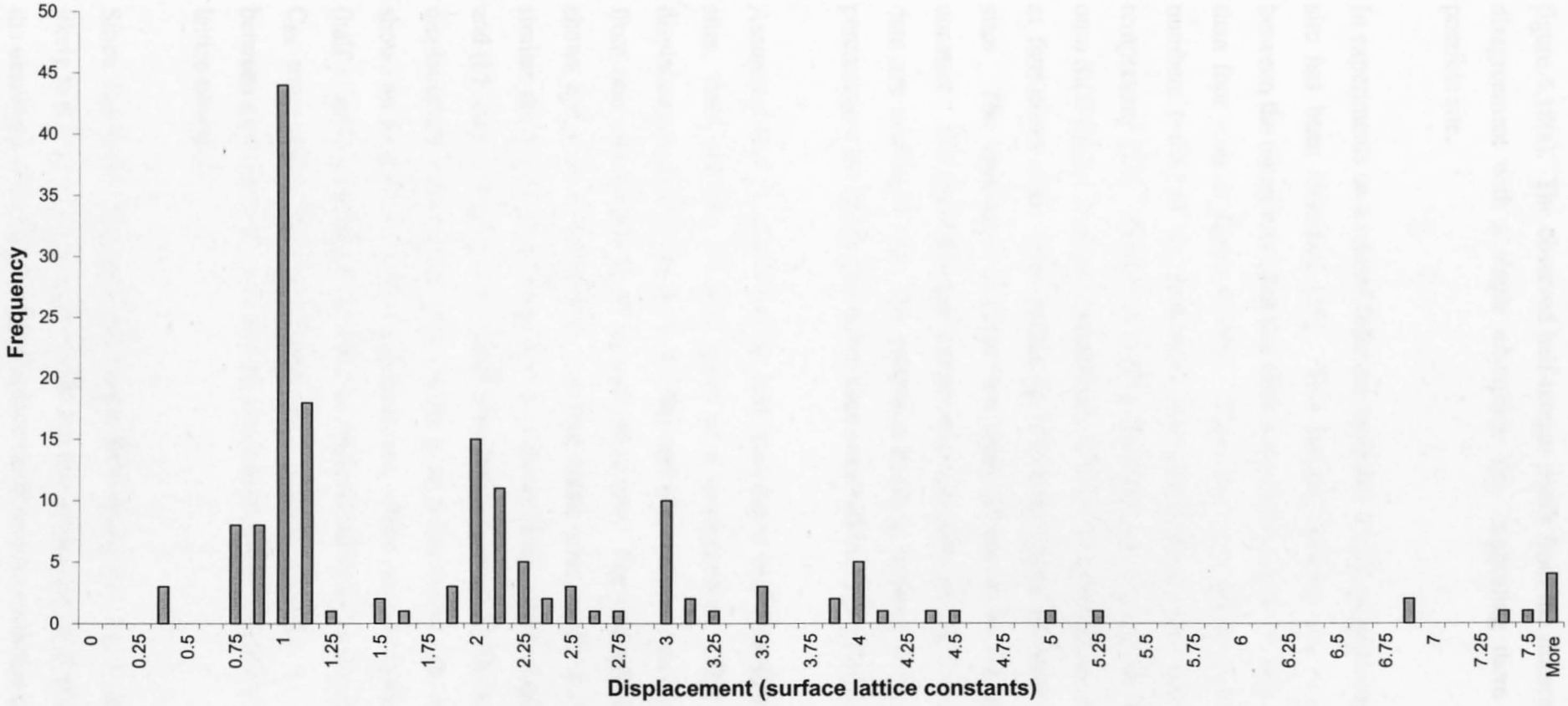

Figure 4.17 *Graph showing the distribution of total displacements of C_{60} molecules after manipulation. Grouping around integer multiples of the surface lattice constant (3.84Å) is observed.*

figure 4.18(a). The observed half-integer peaks from the linescan data are in disagreement with a single adsorption site, suggesting there is a second possible site.

In experiments on a related fullerene molecule, $C_{59}N$, an additional adsorption site has been identified [25]. This second bonding site is again located between the dimer rows, but this time is positioned between two dimers rather than four – as in figure 4.18(b). There has been some evidence of small numbers (~5%) of C_{60} molecules also adsorbing to this location at room temperature [23]. Butcher et al [25] observed that when $C_{59}N$ was deposited onto Si(100)-2x1 at room temperature, ~75% of the molecules were adsorbed at four-dimer sites. The remaining 25% were found to bond to two-dimer sites. The separation of these two types of site is half a surface lattice constant. The observed half-integer displacements of C_{60} from the linescan data are consistent with this proposed bonding scheme, and also with the percentage adsorbed to two-dimer sites observed by Chen et al [23].

Assuming that C_{60} can bond to both two-dimer and four-dimer adsorption sites, there are two possible types of a displacement. The first type of displacement, shown in figure 4.19(a) and (b), occurs when a C_{60} is moves from one adsorption site to an *equivalent* site. For example figure 4.19(a) shows a C_{60} moving between two four-dimer sites, while 4.19(b) shows a similar displacement between two two-dimer sites. Both displacements (a) and (b) have a magnitude of 3.84Å (one lattice constant). The second type of displacement occurs when a C_{60} moves to an *inequivalent* site. Figure 4.19(c) shows an example of such a displacement, which has a magnitude of 1.92Å (half a lattice constant). In order to observe half-integer displacements, the C_{60} must move between inequivalent adsorption sites, as displacement between equivalent site will always result in an integer multiple of the surface lattice constant.

Since C_{60} bonds preferentially to the four-dimer site when deposited, it is likely that it is only weakly bound to the two-dimer site (if at all). As a result, the observations of half-integer displacements may be evidence of a transient

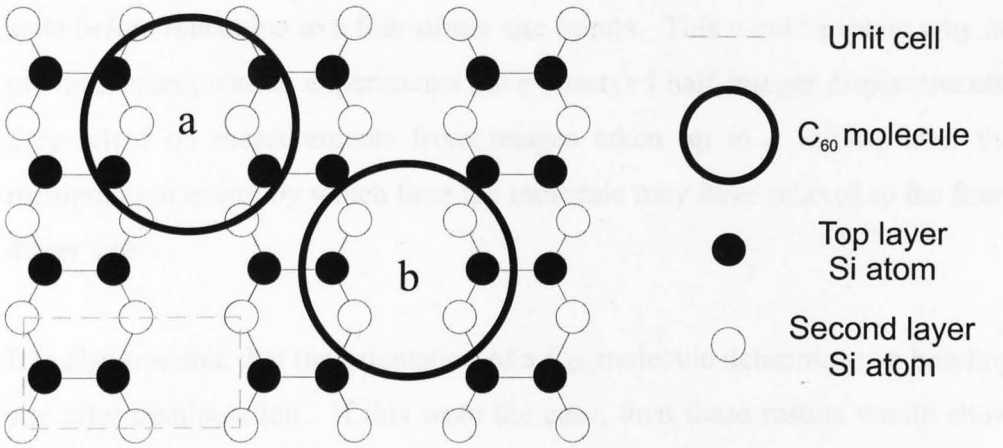

Figure 4.18 *Adsorption sites for C_{60} on a Si(100)-2x1 surface. Large circles represent C_{60} molecules, small filled circles are top layer Si atoms, and small empty circles are second layer Si atoms. (a)Four-dimer site (b) Possible two-dimer site. Surface unit cell is marked in blue.*

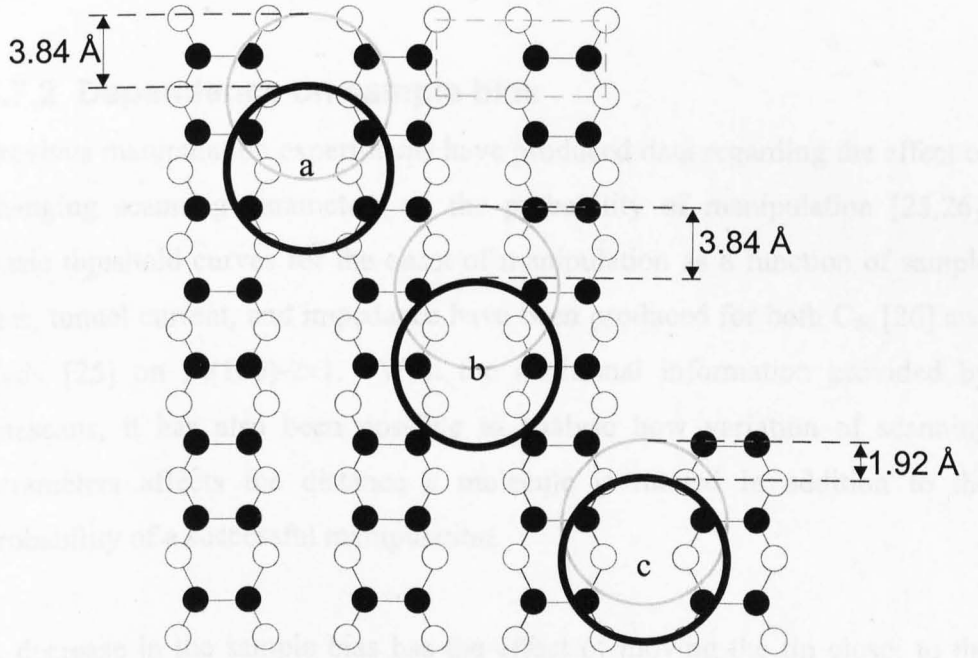

Figure 4.19 *Proposed scheme for displacement of C_{60} on Si(100)-2x1. a) Displacement between two equivalent four-dimer sites, total separation = 1 lattice constant. b) Displacement between two equivalent two-dimer sites, total displacement = 1 lattice constant. c) Displacement between inequivalent adsorption sites, total displacement = ½ lattice constant.*

state before relaxation to a four-dimer site occurs. This would explain why no previous manipulation experiments have observed half-integer displacements; they relied on measurements from images taken up to a minute after the manipulation event, by which time the molecule may have relaxed to the four-dimer site.

It is also possible that the orientation of a C_{60} molecule determines its bonding site after manipulation. If this were the case, then these results would show evidence of rotation of the molecule during manipulation. If the molecule did not rotate, it would always move to an equivalent bonding site, and no half-integer displacements would be observed. The fact that half-integer displacements *are* observed could confirm observations by Moriarty et al [17] of changes in internal structure of individual C_{60} molecules when manipulated, attributed to rotation of the molecule. However, if only integer displacements are observed rotation of the molecule is still possible. In addition, if the bonding site is independent of molecule orientation, half-integer displacements may still be observed without rotation.

4.7.2 Dependence on sample bias

Previous manipulation experiments have produced data regarding the effect of changing scanning parameters on the probability of manipulation [25,26]. Basic threshold curves for the onset of manipulation as a function of sample bias, tunnel current, and impedance have been produced for both C_{60} [26] and $C_{59}N$ [25] on Si(100)-2x1. With the additional information provided by linescans, it has also been possible to analyse how variation of scanning parameters affects the distance a molecule is moved in addition to the probability of a successful manipulation.

A decrease in the sample bias has the effect of moving the tip closer to the surface, as demonstrated in section 4.6.1. This results in an increased interaction between tip and molecule, and therefore an increased probability of successful manipulation. Collating all manipulation attempts with a tunnel current of 1nA, step-size of 1.1Å and dwell time of 21 generated the graph

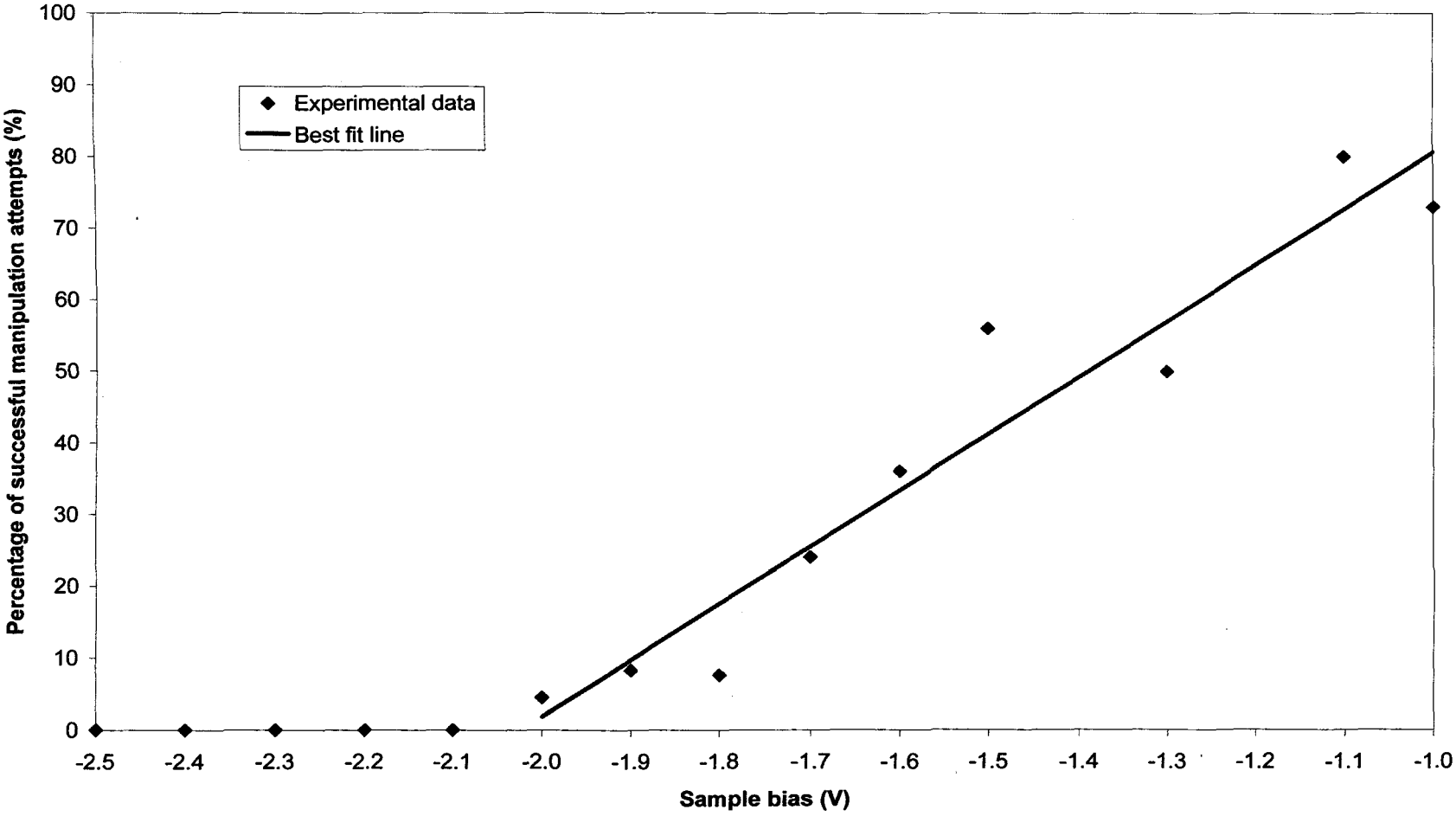

Figure 4.20 *Threshold graph for the onset of manipulation with decreasing sample bias. Data obtained with I=1.0nA, τ=21, step-size=1.1Å.*

shown in figure 4.20, which confirms that manipulation probability increases with a decrease in sample bias. For each value of sample bias, the probability of a successful manipulation was calculated. The resulting curve has a threshold of approximately -2.0V, which is equivalent to a gap impedance of 2.0GΩ, at which point displacements start to be observed. This graph agrees well with similar data published for $C_{59}N$ [25], which showed a threshold value of between 1.5 and 2.5GΩ, however no such data has been published for C_{60}. The only published data for C_{60} manipulation states a probability of manipulation at a gap impedance of 1GΩ as ~95% [17,18], which is also in agreement with figure 4.20.

In addition to an increase in manipulation probability, it was observed that the distribution of displacement size also changed with sample bias. Figure 4.21 shows a series of histograms for different voltage ranges, showing the fraction of successful manipulations vs. the distance moved in lattice constants. Each histogram is scaled such that the total frequency is one. Note that these graphs only show *successful* manipulations, and so the actual number of events is different for each graph due to the different success rates for different biases. However, the graphs are intended to show how the *distribution* of displacements changes with sample bias. When compared, the graphs show a general shift towards larger displacements as the sample bias is decreased.

To provide a true distribution of manipulation displacements, the normalised graphs for each voltage range were scaled according to the manipulation probabilities shown in figure 4.20 and combined into one graph, shown in figure 4.22. It shows that the majority of manipulation events occur with biases below −1.4V, and that the number of large (>6 lattice constants) displacements increases significantly when bias is decreased. Note that the values of displacement are the total distance a molecule moves during a single line in a manipulation (e.g. B3, or B10). Therefore multiple displacements, like those shown in the previous section, appear as a single large displacement in figure 4.22. So the shift towards larger displacements is likely to be a result

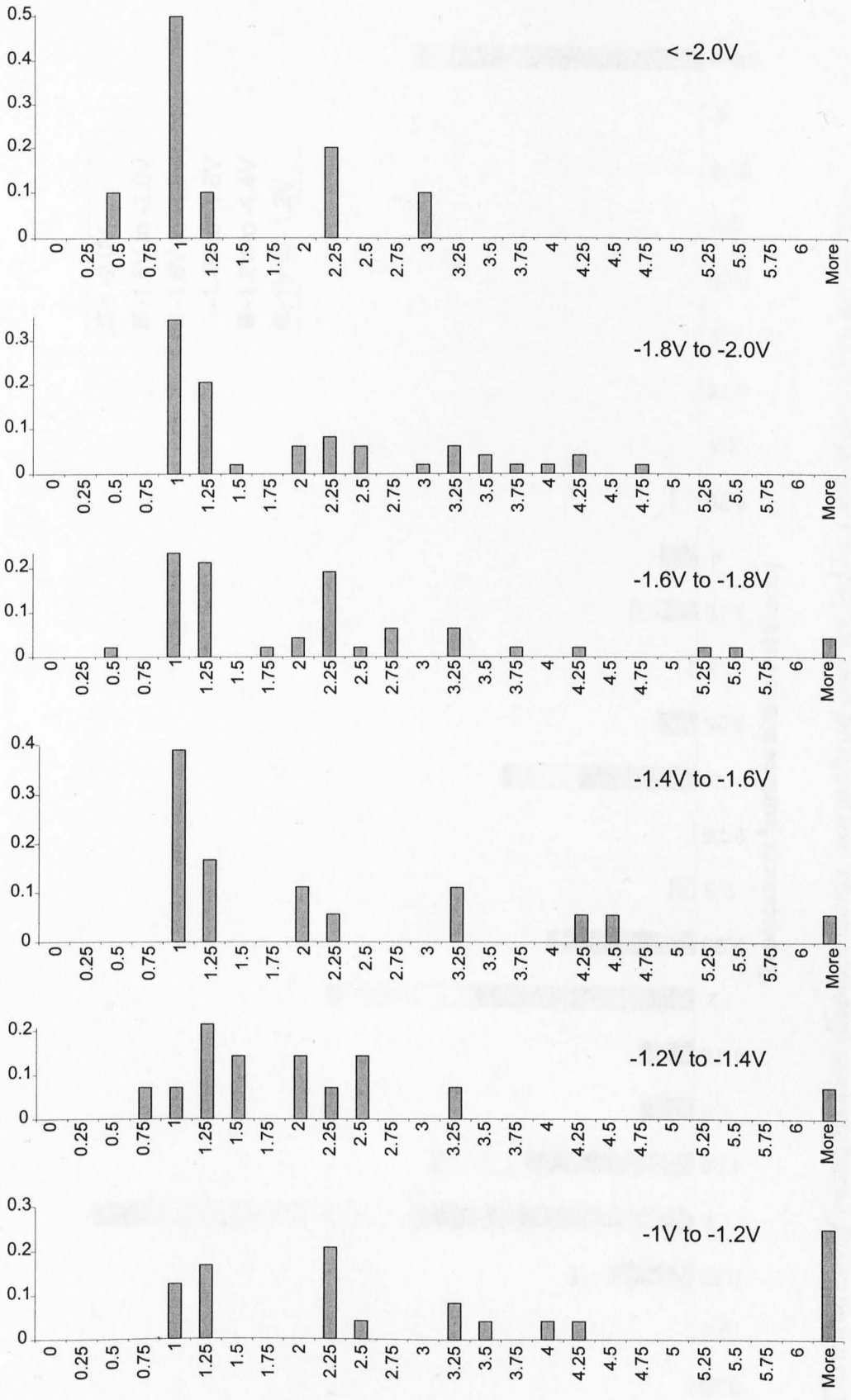

Figure 4.21 *Distribution of C_{60} displacements during manipulation experiments. Graphs show how displacements increase as sample bias is decreased.*

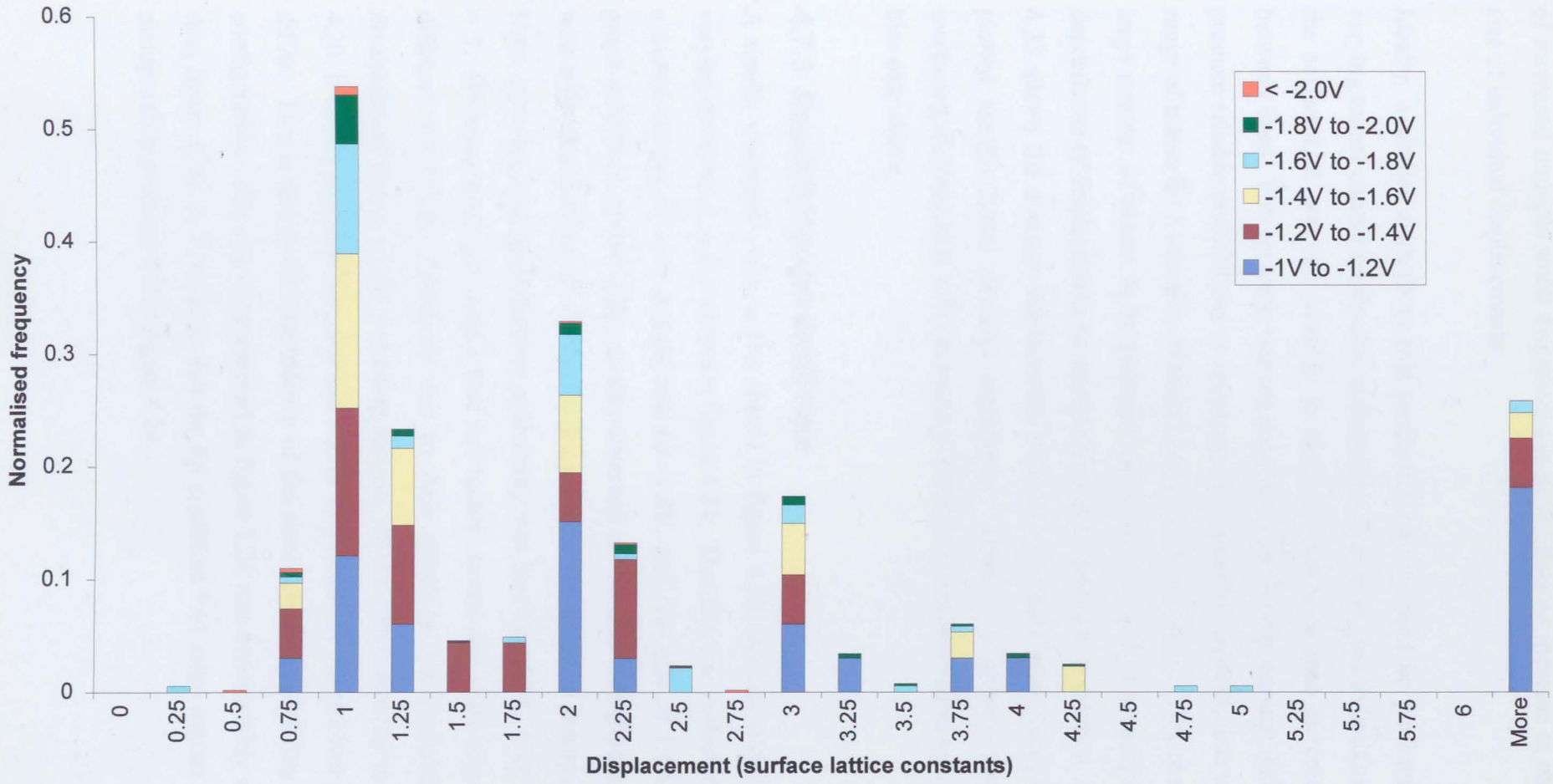

Figure 4.22 *Distribution of manipulation displacements, normalised and scaled by probability of manipulation*

of increased multiple small displacements rather than an increase in absolute size of individual displacements.

Ideally, a similar analysis to that performed above could be performed by varying tunnel current rather than sample bias. However, due to limitations of the software, it was not possible to vary the tunnel current incrementally between lines. This meant it was not possible to get a large enough dataset to produce reliable probabilities or frequency distributions. Instead, data using a range of biases for a selection of tunnel currents was acquired. This enabled a large number of events to be recorded and could be used to investigate the dependence of displacement on *impedance* rather than tunnel current. Figure 4.23 shows the average displacement of a C_{60} molecule after manipulation plotted against tunnel junction impedance. There is a general trend for increasing displacement with decreasing impedance, as observed in the sample bias data above.

4.7.3 Dependence on dwell time

A similar threshold curve to that shown in figure 4.20 was also obtained by varying dwell time, and is shown in figure 4.24. The data was collected using a tunnel current of 1nA, sample bias of –1.8V, and step-size of 1.1Å. The graph exhibits a similar shape to that observed for sample bias (figure 4.20), with a threshold value of ~15 feedback cycles for the onset of manipulation. Note, however, that the maximum probability was less than 25%, even with $\tau = 5$. Different values of sample bias and tunnel current are likely to produce different dwell time thresholds due to their effect on the probability of manipulation shown in the preceding section. If compared directly to figure 4.20, it can be seen that the absolute values of probability for the two graphs differ. This is due to the dependence of the manipulation probability on tip configuration. The data set presented in figure 4.24 was considerably smaller than figure 4.20, so it is likely that the tip condition had more impact on the manipulation probabilities in figure 4.24.

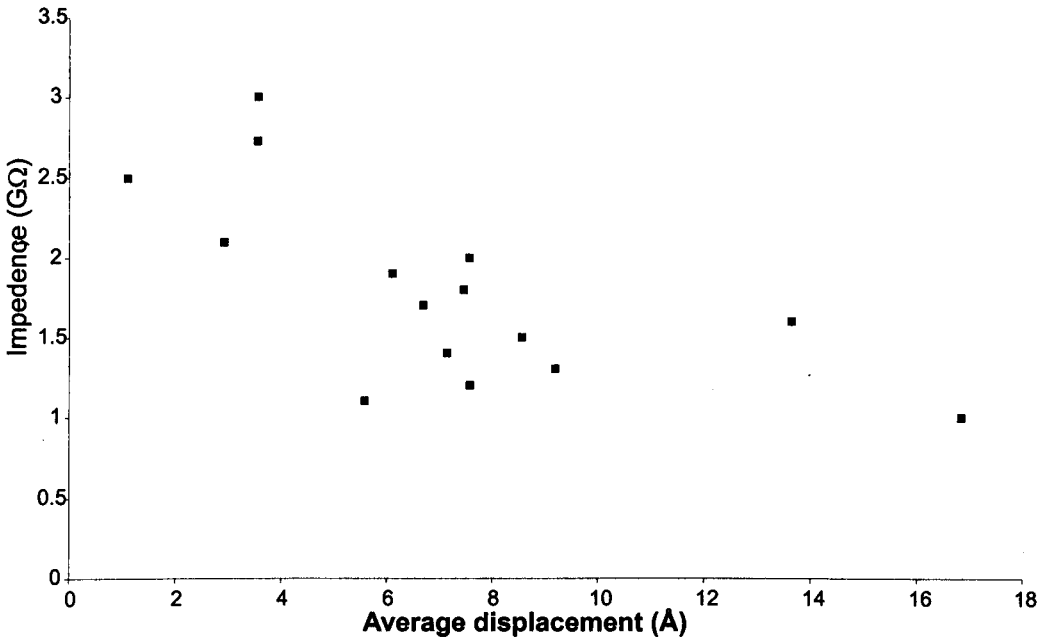

Figure 4.23 *Variation of displacement with tunnelling gap impedance.*

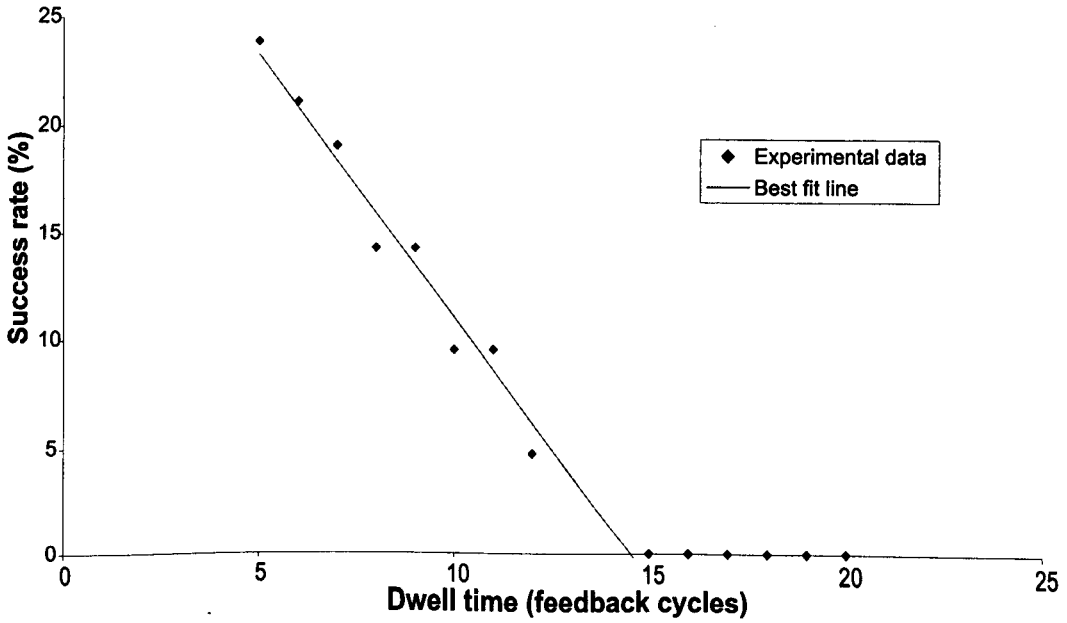

Figure 4.24 *Threshold graph for onset of manipulation with decreasing dwell time. Data obtained with I=1nA, V=-1.8V, step-size=1.1Å.*

The analysis of feedback response in section 4.6.2 showed that a decrease in dwell time, τ, resulted in a decrease in the effectiveness of the feedback loop, particularly with values of τ below ~10. This reduction in feedback loop efficiency causes reduced tip-molecule separation when initially encountering a molecule (see section 4.6.2), and therefore increased tip-molecule interaction at these points. Therefore these results suggest that the reason a decrease in dwell time increases the probability of manipulation is that the tip-molecule separation is reduced, increasing the tip-molecule interaction. This is exactly the same result as that seen for sample bias and impedance. Hence the critical parameter is the tip-molecule separation during a manipulation attempt.

4.8 Attractive mode manipulation at room temperature

It was discussed in an earlier section how previous experiments at low temperature exploited an attractive interaction to move atoms [6,7,19]. Bartels et al [19] also observed repulsive interactions at low temperature, similar to those presented in the preceding section. It is possible that the tip-molecule interactions leading to manipulation at low temperature and at room temperature are similar. At low temperature adsorbates can be much more weakly bound to the substrate without diffusion, allowing weaker interactions between tip and adsorbate to result in a displacement. At room temperature, adsorbates must be chosen which bond more strongly to the surface to prevent thermal diffusion. This means that a larger force is required to initiate movement. If the attractive force between tip and adsorbate is large enough to overcome the diffusion barrier of an adsorbate at room temperature, attractive mode displacements may be observed.

No evidence for attractive interactions has been published for C_{60} at room temperature, suggesting that if it occurs, it is considerably weaker than the repulsive interaction demonstrated in the previous section. Unpublished

images obtained by P. Moriarty [26] have strongly suggested that attractive mode displacements do occur at room temperature.

4.8.1 Evidence from images

A selection of images are shown in figure 4.25, all of which contain examples of C_{60} molecules moving during the acquisition of a scan. Image (a) has an attractive manipulation highlighted. The discontinuity in the shape of the molecule indicates that it moved during acquisition of the image. In fact, the molecule moves twice, by what appears to be the same amount each time. The scan is acquired from bottom to top, so lines nearer the top of the scan were acquired after lines nearer the bottom. Analysis of the molecule highlighted in (a), shows that over half of the molecule was scanned before it moved *up* the image. This indicates that the interaction must have been attractive in nature. If the interaction were repulsive, the only way the molecule could move up the image would be if it were pushed from below. However, the tip was clearly located higher up the scan than the molecule at the time of the displacement as more than half of the molecule had been imaged. Therefore, the interaction must be attractive in nature.

Image (b) shows more examples of movement during scanning. The molecule labelled by the number 1 on the image shows a slightly different type of discontinuity to that in (a). This time, the first movement occurs before the tip has passed the middle of the C_{60}. However, the interaction is still clearly attractive as the molecule still moves towards the tip – this time down the image rather than up. The second movement takes an identical form to that observed in (a). The molecule marked with a number 2 in (b) exhibits sideways movement. This is because the dimer rows are horizontal rather than vertical in this part of the image. All displacements of this kind have been observed to occur along dimer rows, as the barrier height is much larger across the rows. Such horizontal movement is not easy to interpret as the STM tip moves in both directions during each scan line.

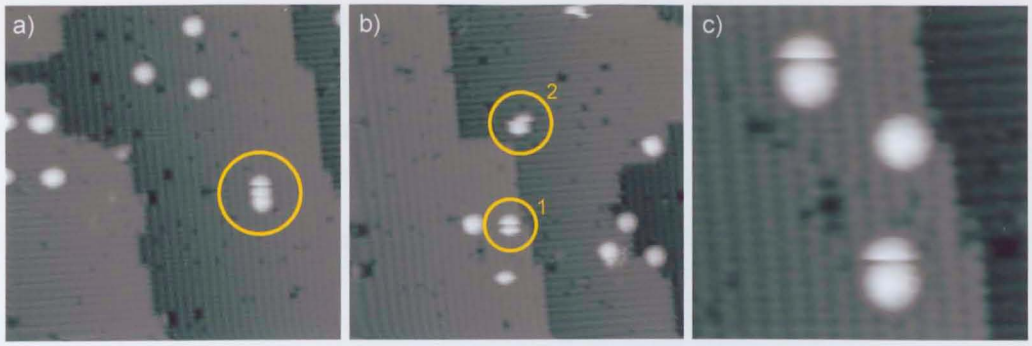

Figure 4.25 *Examples of attractive mode manipulation during scanning.*

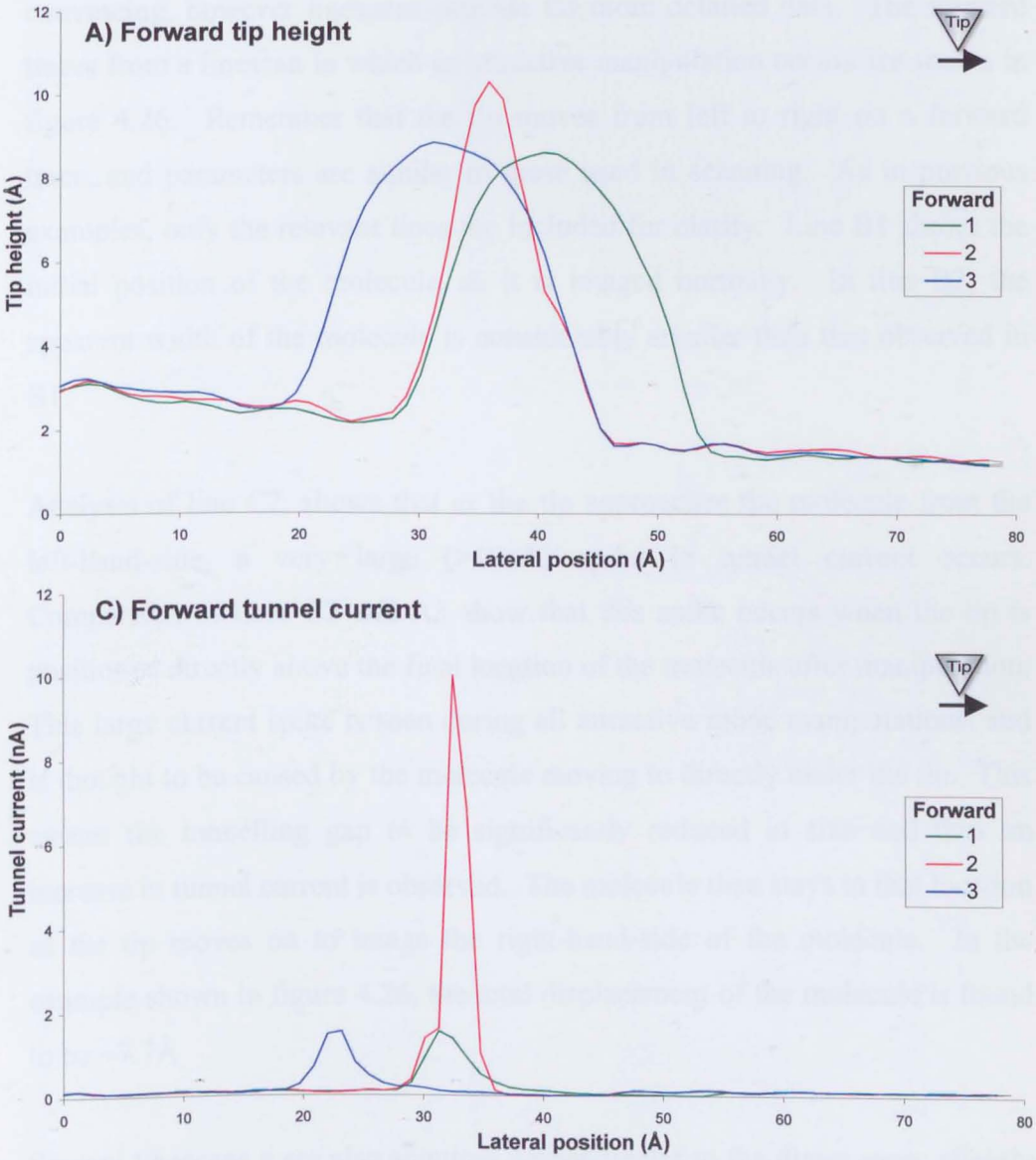

Figure 4.26 *Forward traces obtained during an attractive mode manipulation. Forward parameters: I=0.1nA, V=-3.0V, step-size=1.1Å, τ=21.*

The third image (c) shows a close-up of two C_{60} molecules moving up the image. In each case, the molecule is almost completely scanned before it moves. From these images there can be little doubt that an attractive interaction was present. Note that no evidence for repulsive interactions is observed under normal scanning conditions.

4.8.2 Evidence from linescans

The evidence for attractive interactions from the images shown above is quite convincing, however linescans provide far more detailed data. The forward traces from a linescan in which an attractive manipulation occurs are shown in figure 4.26. Remember that the tip moves from left to right on a forward trace, and parameters are similar to those used in scanning. As in previous examples, only the relevant lines are included for clarity. Line B1 shows the initial position of the molecule, as it is imaged normally. In line B2, the apparent width of the molecule is considerably smaller than that observed in B1.

Analysis of line C2, shows that as the tip approaches the molecule from the left-hand-side, a very large (>10nA) spike in tunnel current occurs. Comparison of lines C2 and A3 show that this spike occurs when the tip is positioned directly above the final location of the molecule after manipulation. This large current spike is seen during all attractive mode manipulations, and is thought to be caused by the molecule moving to directly under the tip. This causes the tunnelling gap to be significantly reduced in size and thus an increase in tunnel current is observed. The molecule then stays in that location as the tip moves on to image the right-hand-side of the molecule. In the example shown in figure 4.26, the total displacement of the molecule is found to be ~7.7Å

Several linescans were also acquired perpendicular to the dimer rows, slightly offset from a C_{60}, in order to reproduce a situation similar to normal scan acquisition where attractive manipulations have been observed. Figure 4.27

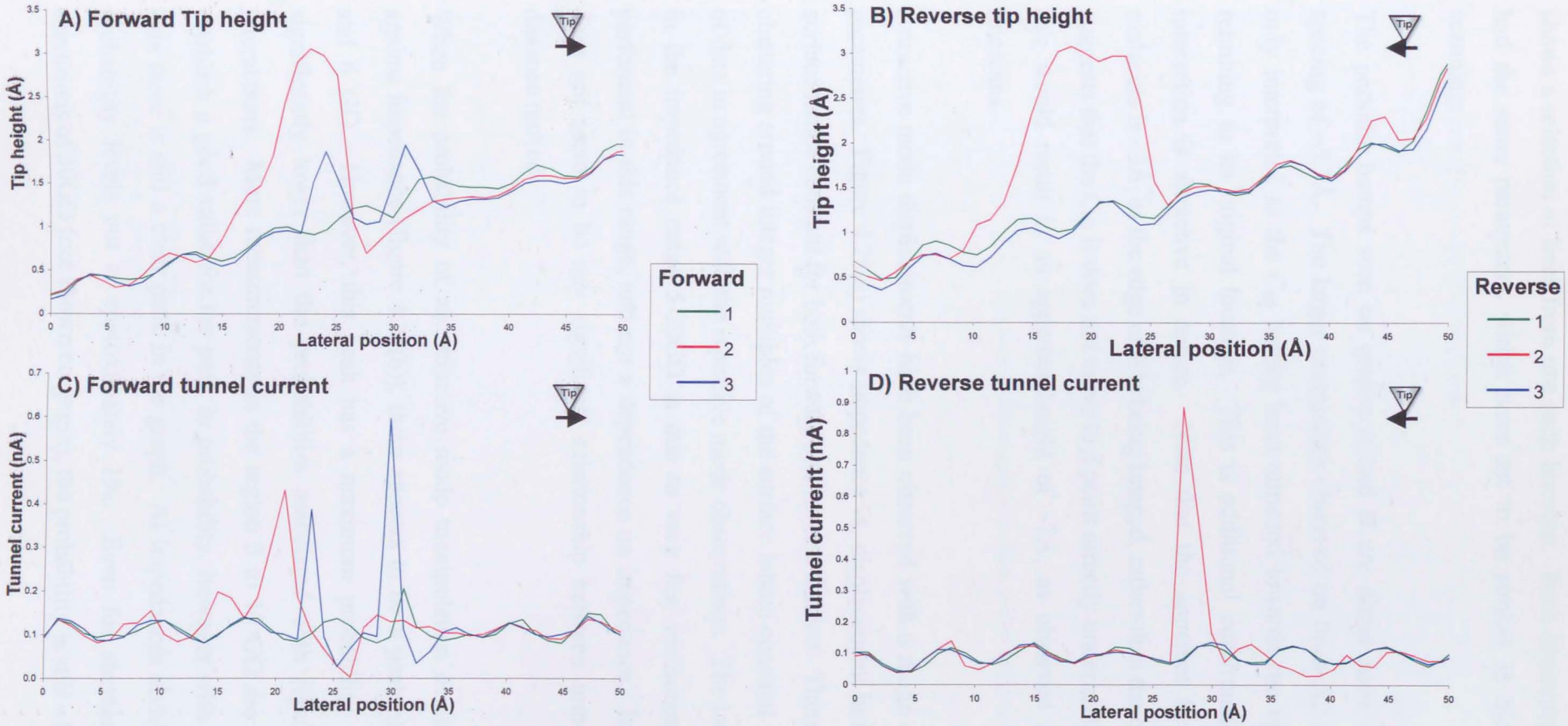

Figure 4.27 *An example of a C_{60} attractive to an STM tip moving perpendicular to the direction of molecular displacement. Forward and reverse parameters identical: I=0.1nA, V=-3.0V, step-size=1.1Å, τ=21.*

shows a selection of lines from one such linescan. Both directions of motion had the same parameters, which were set to be similar to those used in scanning.

The periodic bumps seen on graphs A and B are dimer rows and have a spacing of ~7.7Å. The larger protrusions observed on lines A2 and B2 can only interpreted as the C_{60} having been attracted towards the tip, and then returning to its original location. This is additional confirmation that the interaction is attractive in nature. Note that the apparent height of the molecule is ~3Å, as the edge of it is being imaged, rather than the centre. This suggests that the C_{60} is does not move to a point directly underneath the tip, as this would result in an apparent height of ~7Å, as observed in previous linescans.

Attractive mode displacements have been observed with a range of scanning parameters. Figure 4.28(a) shows impedance vs. displacement in multiples of surface lattice constant for both forward and reverse motion. There is obvious clustering around integer multiples of the surface lattice constant in both sets of data in agreement with the repulsive mode observations. The lack of points in the impedance range 5-30GΩ is due to very few measurements being performed in this range, and not a dependence on impedance. In fact there, does not seem to be any significant relationship between impedance and distance moved.

When the probability of an attractive mode manipulation event is plotted against impedance (figure 4.28(b)), there appears to be a peak at between 3 and 6 GΩ. However, this peak has a maximum probability of <10% - significantly lower than the probabilities associated with repulsive mode interactions. More measurements in the region 3 to 10 GΩ are required to establish a good value for the peak in probability, however with the present data there is still a clear peak in the graph. At impedances above 6GΩ, the probability levels out at approximately 1%. Even for standard scanning conditions of 30GΩ (not shown on graph), the probability is still ~1%. It is

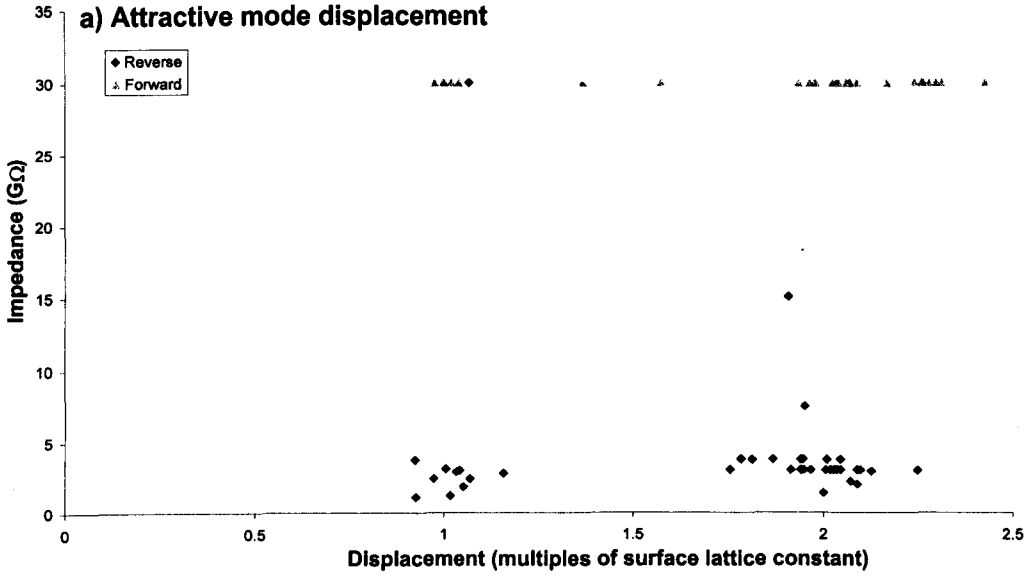

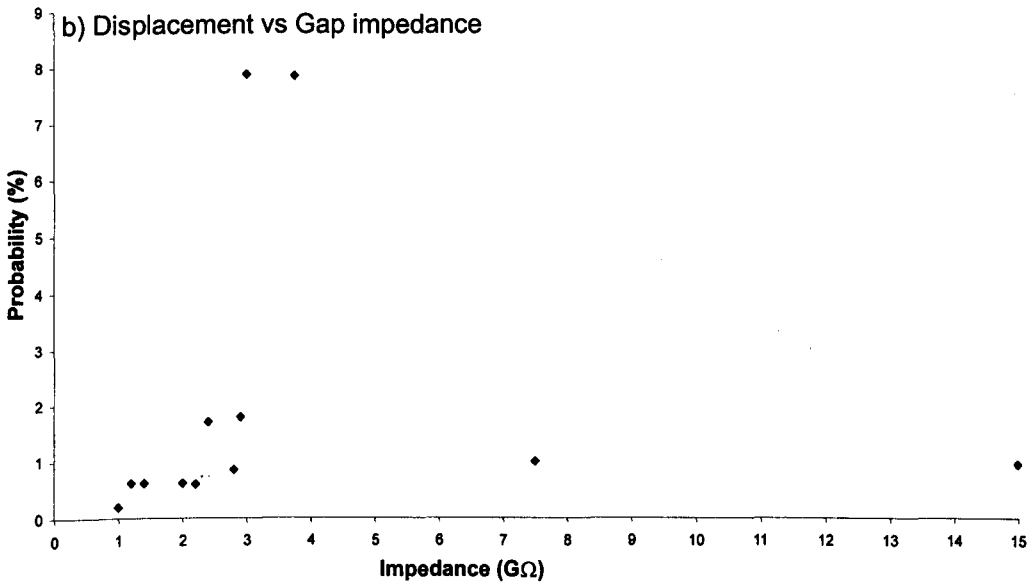

Figure 4.28 *Dependence of attractive mode manipulation on impedance. a) Impedance vs displacement , b) Probability of manipulation vs impedance.*

also important to note that a significant dependence on tip configuration was observed (i.e. sometimes more manipulation events were observed than at others).

For impedances below ~2GΩ the probability of attractive mode manipulation events decreases rapidly such that at 1GΩ it is less than 0.2%. This implies that there is a minimum impedance at which attractive mode manipulation can occur, and an optimum impedance with the greatest probability of manipulation. This is consistent with the results obtained at low temperature by Bartels et al [19] and with models proposed for atomic manipulation [8,9], all of which propose a transition from attractive to repulsive interactions with decreasing tip-adsorbate separation.

4.9 Apparent transparency of C_{60}

An interesting anomaly was observed on several different occasions whilst collecting manipulation data. Under certain tip conditions, the system would respond less and less to a C_{60} molecule as the bias decreased. Figure 4.29 shows a typical example of this effect. While all the lines in graph A show the apparent height of the C_{60} to be ~6.5Å, lines on graph B show different apparent heights. Each line on graph B was acquired with a different sample bias shown in the legend. For B1 a bias of –3V was used, increasing by 0.2V per trace, to –1.2V in B10. The apparent height of the C_{60} in B1 was ~6.5Å, as in graph A, however this decreased to <1Å in B10. It is significant to note that the response to the Si surface does not change with bias, apart from the displacement toward the surface observed before. In addition, the shape of the C_{60} molecule is asymmetrical for biases less than -2V (line B6). In fact, in line B10 (-1.2V) the C_{60} asymmetry is so severe a combination of a small depression and protrusion within the original width of the molecule is observed. Graph D, the reverse tunnel current, clearly shows that the variation in tunnel current also decreased with bias to such an extent that the final line D10 (-1.2V) was virtually flat at the target tunnel current (0.2nA).

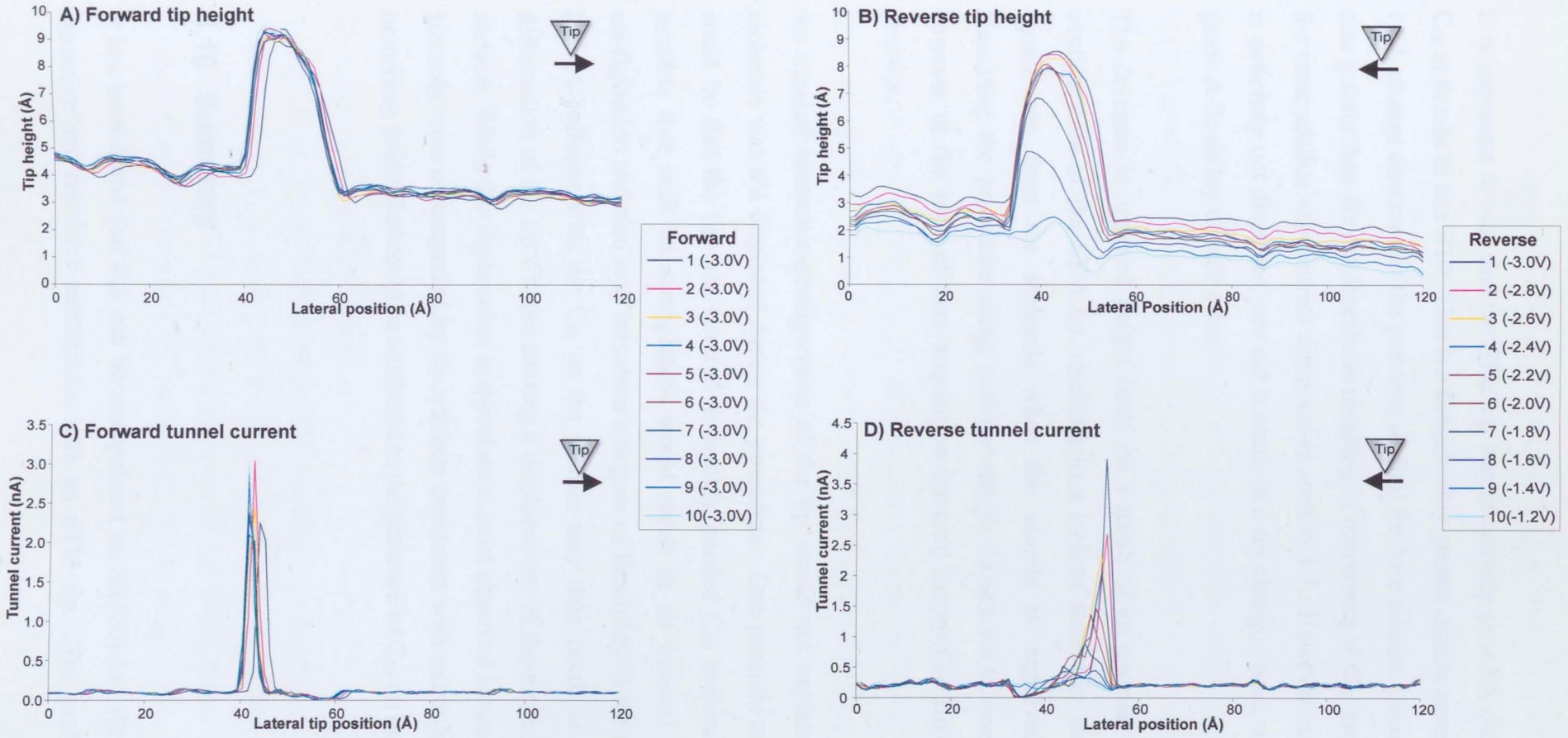

Figure 4.29 *Apparent transparency of C_{60} on Si(100)-2x1. Forward parameters: I=1.0nA, V=-3V, step-size=1.1Å, τ =21 Reverse parameters: I=0.2nA, V=-3V to -1.2V, Step-size=1.1Å, τ = 21*

It is important to note that the STM tip was effectively over 6Å closer to the C_{60} molecule in line B10. This is a considerably greater displacement than the 1.6Å change observed in the previous section for bare silicon. Note that it is also greater than the displacements resulting in movement of C_{60} molecules in the manipulation experiments discussed in section 4.7. However here the C_{60} is definitely not displaced, nor did it result in a tip change, as all the lines in graph A lie on top of each other.

The decrease in apparent height could be a result of an unusual electronic configuration of the STM tip, resulting in a lack of states for electrons to tunnel into from the molecule when the sample is negatively biased. Repeating the procedure using positive sample biases could confirm this, however at the time of data acquisition imaging in positive bias was not possible.

An unusual electronic configuration of the tip would not explain why the molecule was not displaced during the procedure. One possible explanation could be that the tip was covered in weakly bonded C_{60} molecules. It is possible that such an arrangement would result in an unusual electronic configuration and also may introduce a degree of flexibility to the end of the tip. A collision with the C_{60} on the surface may then result in an elastic deformation of the tip without causing a displacement of the molecule on the surface. While this explanation is speculative, most observed instances of this anomaly were accompanied by tip artefacts consistent with multiple localised tunnelling points that could be attributed to the presence of C_{60} on the tip.

4.10 Summary

It has been found that C_{60} can be manipulated on Si(100)-2x1 through both attractive and repulsive interactions with an STM tip. The probability of

manipulation for both modes of interaction was found to be critically dependent on tip-molecule separation. This separation was found to be determined by a combination of sample bias, target tunnel current, and efficiency of the feedback loop during data acquisition. These factors directly affected the manipulation probability of a C_{60} due to their affect on the tip-molecule separation.

Movement of C_{60} was observed to occur in discrete steps during manipulation. These steps occurred as integer and half-integer multiples of the surface lattice constant. The observation of half-integer displacements is evidence for an alternative bonding site for C_{60} on Si(100)-2x1, previously only seen for $C_{59}N$.

The stability of an STM tip was found to be dependent on the step-size between data points, with an increase in step-size resulting in an increase in the probability of a change in tip configuration. The dwell time at each data point was found to critically affect feedback loop performance, with values below 10 cycles causing the most significant decreases in performance.

4.11 References

1. G. Moore, Intel Corporation, in a speech made in 1965
2. "Performance systems on a chip key to Moore's Law", VNU business online, http://www.vnunet.com/News/103694 (1999)
3. "Moore's Law has to break down", http://www.cm.ph.bham.ac.uk/reports/roadmap99b/sld024.htm
4. X. M. Zhao, Y. N. Xia, G. M. Whitesides, J. Mat. Chem. **7**, 1069 (1997)
5. F. Shimizu, "Atomic holography technology", 44th International Conference on Atom, Ion and Photon Beam Technology and Nanofabrication (2000)
6. D. M. Eigler and L. K. Schweizer, Nature **344** 524 (1990)

7. J. R. Cerda, P. L. de Andres, F. Flores, and R. Perez, Phys. Rev. B **45** 8721 (1992)
8. X. Bouju, C. Joachim, C. Girard and P. Sautet, Phys. Rev. B **47** 7454 (1993)
9. A. Buldum and S. Ciraci, Phys. Rev. B **54** 2175 (1996)
10. M. F. Crommie, C. P. Lutz, D. M. Eigler, Science **262** 218 (1993)
11. H. C. Manoharam, C. P. Lutz, D. M. Eigler, Nature **403**, 512 (2000)
12. M. T. Cuberes, R. R. Schlittler and J. K. Gimzewski, Appl. Phys. Lett. **44** 3016 (1996)
13. T. A. Jung, R. R. Schlittler, J. K. Gimzewski, H. Tang and C. Joachim, Science **271** 181 (1996)
14. S. Maruno, K. Inanaga and T. Isu, Appl. Phys. Lett. **63** 1339 (1993)
15. P. H. Beton, A. W. Dunn and P. Moriarty Appl. Phys. Lett. **67** 1075 (1995)
16. A. W. Dunn, P. Moriarty and P. H. Beton J. Vac. Sci. Technol. A **15** 1478 (1996)
17. P. Moriarty, Y-R. Ma, M. D. Upward and P.H. Beton Surf. Sci. **407** 27 (1998)
18. P. Moriarty, Y-R. Ma, M. D. Upward, P. H. Beton and D. Teehan Semicond. Sci. Technol. **13** A47 (1998)
19. L. Bartels, G Meyer and K-H. Rieder, Phys. Rev. Lett. **79** 697 (1997)
20. TOPSystem version 1, provided by Oxford Instruments SPM Group, formerly WA Technology
21. T. M. H. Wong and M. E. Welland, Meas. Sci. Technol. **4** 270 (1993)
22. "Scanning Tunnelling Microscopy", J. Stroscio & W. Kaiser, Academic Press 1993
23. D. Chen and D. Sarid, Surf. Sci. **318** 74 (1994)
24. T. Hashizume, X. D. Wang, Y. Nishina, H. Shinohara, Y. Saito, Y. Kuk, T. Sakurai, Jpn J. Appl. Phys. **31** L881 (1992)
25. M. J. Butcher, F. H. Jones, P. Moriarty, P.H. Beton, K. Prassides, K. Kordatos and N. Tagmatarchis, App. Phys. Lett. **75** 1074 (1999)
26. P Moriarty, unpublished

Chapter 5
Construction of a multifunction scanning probe microscope head

In this chapter, a multifunction scanning probe microscope head capable of operation in magnetic field and in vacuum is described. The system was designed and built entirely within the School of Physics and Astronomy at Nottingham University, and is controlled by the custom-built SPM controller described in Chapter 3. Examples of operation as a contact mode AFM and a STM in magnetic field and in vacuum are presented. In addition, work towards operation as a magnetic resonance force microscope (MRFM) is discussed. Three-axis inertial sliding motors have been developed for coarse positioning, plus an optical fibre interferometer for detection of cantilever motion.

5.1 Introduction

Since the invention of the scanning tunnelling microscope by Binnig et al [1] in 1982, a large number of related scanning probe techniques have been developed. These range from scanning near-field optical microscopy [2], through various scanning force microscopes [3] to the more recent magnetic resonance force microscopy. The use of these techniques has made it possible to locally probe many forms of interaction and to image a vast range of surfaces on the atomic scale.

Of all the techniques to be developed from STM, the scanning force microscope (SFM) has become the most widely used, mainly due to its versatility. Unlike STM, the interactions in SFM are not caused by conduction of electrons, so the technique can be used to image insulating samples in addition to metals and semiconductors. This has led to its use in fields as diverse as biochemistry, metallurgy and surface science. Many samples

require very different environments to maintain their structure. For example biological samples often need to be immersed in liquid, whereas some semiconductor surfaces can only be formed under ultra high vacuum and yet other samples exhibit novel properties in magnetic fields. SFMs, and in particular AFM has proved to be capable of imaging under all these conditions.

With so many scanning probe techniques available, each providing different data, there is a clear need for a single integrated system providing a range of SPM techniques with which to investigate a sample. Such a system must be capable of operation in a range of environments, and provide a simple method of changing the probe technique in use. In recent years, commercial systems have become available that offer a large range of SPM techniques in a single instrument [4]. However, these instruments have tended to require in-air operation and are not generally designed to function in magnetic fields.

The motivation for the work presented in this chapter is to develop a SPM capable of operation in both magnetic field and in vacuum, with the ultimate aim of adding magnetic resonance force microscope (MRFM) functionality.

5.2 Overview of the SPM head

Every form of SPM has four basic components, a probe, a sample, a piezoelectric scan mechanism, and a sensor to detect the probe-sample interactions. Since these components are common to all SPMs, it should be possible to change from one SPM mode to another relatively simply. The most useful SPM head should enable changes of both the type of probe and detection mechanism. Such a head would enable virtually all SPM modes to be implemented without significant modifications to the head. If the system were also to be designed to operate in a range of different environments, a huge range of samples and interactions could be investigated.

The SPM head described here was designed to operate in ultra high vacuum (UHV), within the room-temperature bore of a 7 Tesla superconducting magnet. To facilitate this, materials used in the construction of the head were chosen to be both non-magnetic and UHV compatible. In addition, the magnet bore restricted the total diameter of the head plus vacuum tube to 54mm, resulting in a head diameter of 40mm.

Figure 5.1 shows a schematic of the SPM head, including the vacuum system and vibration isolation mechanism. The head plus vacuum system can be winched vertically as a unit, to allow insertion and removal from the magnet bore. Alternatively, the vacuum tube may be detached allowing the head to be winched out to gain access to the sample stage. The entire system is supported above the magnet by four pneumatic legs, which provide vibration isolation and limited positional control of the vacuum tube. The pumps can be detached to ensure good vibration isolation, with the pressure in the chamber held by a valve.

A close-up photograph of the SPM head is shown in figure 5.2(a), along with an equivalent schematic in figure 5.2(b). The support rods, shown as vertical bars in figure 5.2(b), were made to the exact length required to locate the sample/cantilever stage on the central line (i.e. maximum field) of the magnet. The rods, screwed into the top flange of the vacuum system (shown in figure 5.1 with a winch hook attached), can be detached from the microscope head to facilitate removal of the head for maintenance.

The head itself consists of three stages, as shown in figure 5.2. Stage 1, located at the top of the head, contains a 3-axis inertial sliding motor for positioning of the optical fibre used in the interferometer system. The second stage has a detachable sample holder, which can contain either a sample or a cantilever probe, depending on the mode of operation in use. A second 3-axis inertial sliding motor is attached to the bottom stage, onto which is mounted a quadranted piezoelectric tube to scan a sample relative to a probe.

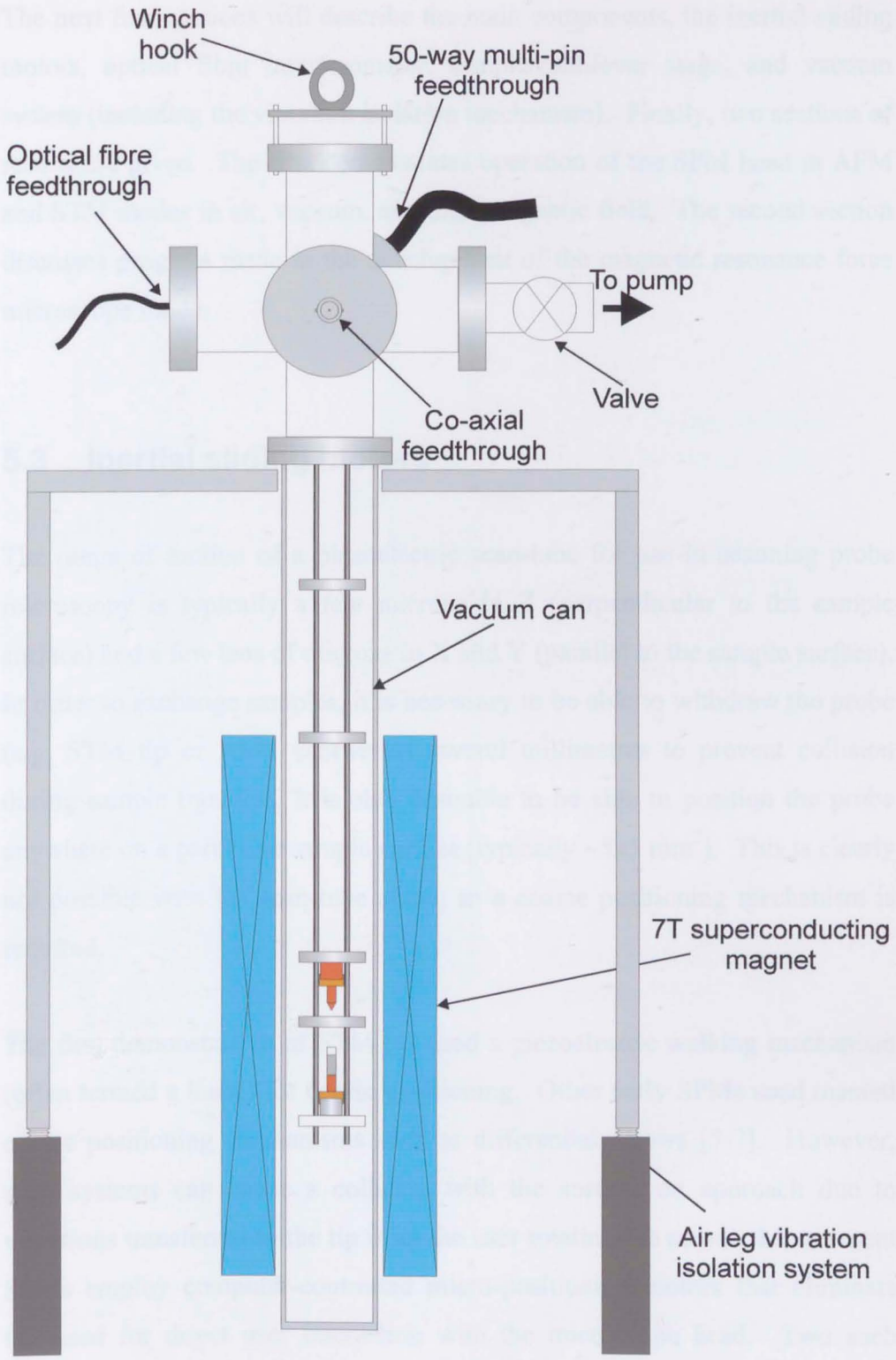

Figure 5.1 *Schematic of the multi-function SPM head and vacuum system.*

The next four sections will describe the main components, the inertial sliding motors, optical fibre interferometer, sample/cantilever stage, and vacuum system (including the vibration isolation mechanism). Finally, two sections of results are given. The first demonstrates operation of the SPM head in AFM and STM modes in air, vacuum, and high magnetic field. The second section discusses progress made in the development of the magnetic resonance force microscope mode.

5.3 Inertial sliding motors

The range of motion of a piezoelectric scan-tube for use in scanning probe microscopy is typically a few microns in Z (perpendicular to the sample surface) and a few tens of microns in X and Y (parallel to the sample surface). In order to exchange samples, it is necessary to be able to withdraw the probe (e.g. STM tip or AFM cantilever) several millimetres to prevent collision during sample transfer. It is also desirable to be able to position the probe anywhere on a particular sample surface (typically ~5x5 mm^2). This is clearly not possible with the scan-tube alone, so a coarse positioning mechanism is required.

The first demonstration of STM [1] used a piezoelectric walking mechanism (often termed a louse) for coarse positioning. Other early SPMs used manual coarse positioning mechanisms such as differential screws [5-7]. However, such systems can cause a collision with the surface on approach due to vibrations transferred to the tip from the user rotating the screw. More recent SPMs employ computer-controlled micro-positioning motors that eliminate the need for direct user interaction with the microscope head. Two such systems are inchworms [8,9] and inertial sliding motors [10,14]. The former uses a clamp-stretch-unclamp system in which the moving stage is always statically clamped by at least one point along its length. Inertial sliders, on the other hand, use a dynamic method proposed by Pohl [10] in which the entire moving stage periodically overcomes static friction and slides relative to a

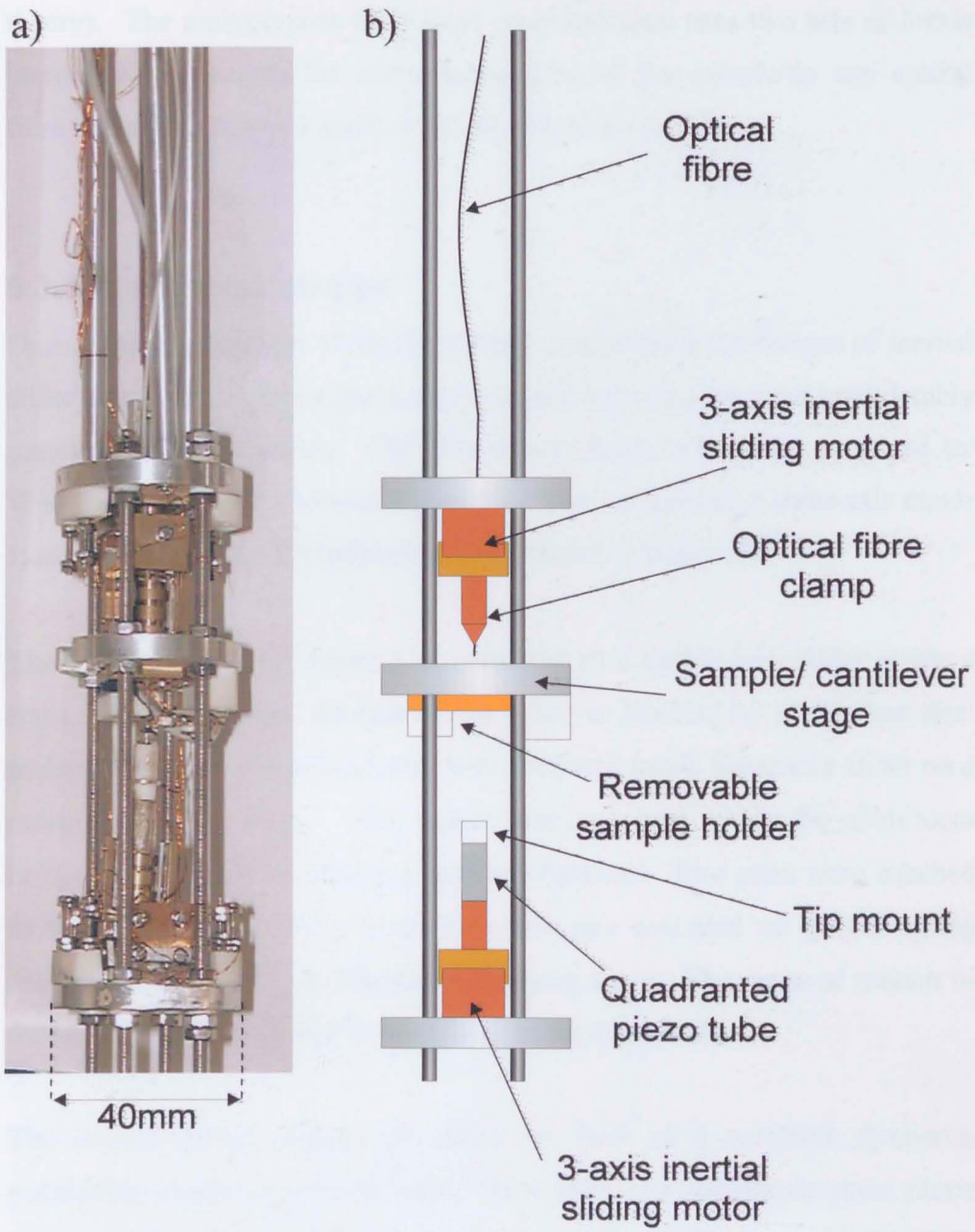

Figure 5.2 *Detail of multi-function SPM head. a) photograph of head. b) Schematic of head.*

static clamp (see chapter 2 for a more detailed discussion of inertial sliding theory). The multipurpose SPM head described here uses two sets of 3-axis inertial sliding motors for coarse positioning of the sample/tip and optical fibre, located on stages 1 and 3 of the head (see figure 5.2).

5.3.1 Mechanical design

During the development of the SPM head, several different designs of inertial slider were tested. It was found that two particular designs were considerably more reliable than others. The first was a single axis motor proposed by Woodburn et al [13], shown in figure 5.3. The second was a three-axis motor system developed by Kleindiek et al [14], shown in figure 5.4.

The single-axis motor (figure 5.3) consisted of a quartz tube slider inside a static aluminium tube. Motion of the slider is initiated by a stainless steel mass accelerated by a piezoelectric *tube* mounted inside the quartz slider on a machinable glass plug. The quartz tube was held inside the aluminium holder by three pairs of stainless steel ball bearings. Two pairs were attached to the inside of the tube, with the other pair mounted on a leaf spring mechanism to provide an adjustable clamping force. The range of motion of the motor was only limited by the length of the quartz tube.

The second design, figure 5.4, takes the form of a complete three-axis positioning system in a single unit. Three pairs of piezoelectric shear plates initiate motion, onto which are glued quartz rods using vacuum epoxy [16]. These rods mate with V-grooves on each sliding stage, forming guiding tracks for the stage to run along. One piezoelectric plate in each pair is mounted on a leaf spring to provide an adjustable clamping force between the quartz rods and V-grooves.

Although both designs of motor were successfully implemented, Kleindiek et al's 3-axis system was chosen for use in the SPM head, as it was extremely compact (25 x 25 x 30 mm^3), and therefore ideally suited to the restricted

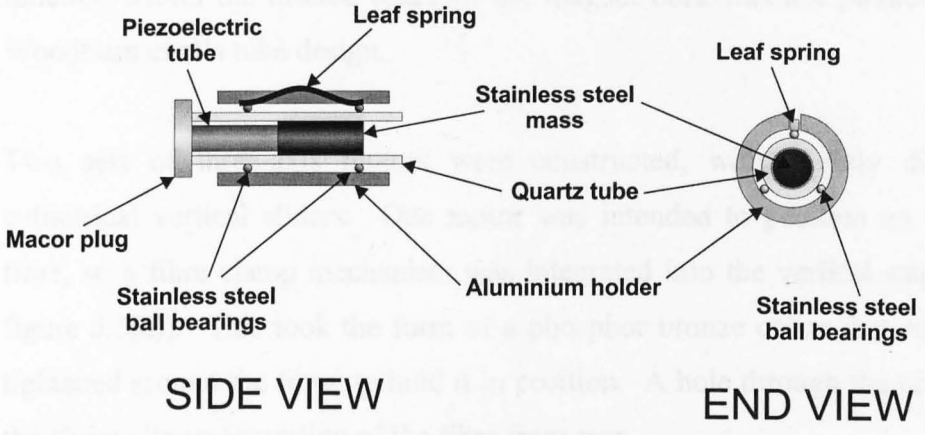

Figure 5.3 *Single axis cylindrical inertial sliding motor. Actuator is a piezoelectric tube connected to a stainless steel mass. Original design proposed by Woodburn et al.*

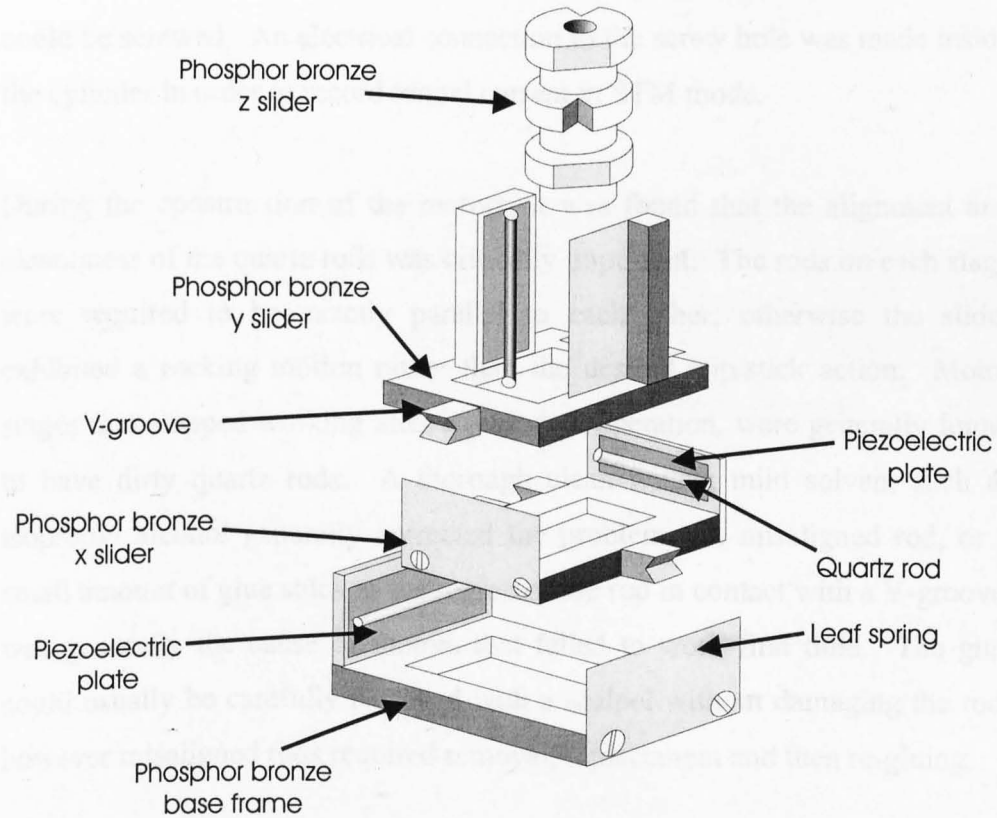

Figure 5.4 Three-*axis inertial sliding motor. Actuator are shear piezoelectric plates with quartz rods attached. Original design proposed by S. Kleindiek et al.*

environment of a magnet bore. An equivalent three-axis system that could function within the limited space of the magnet bore was not possible with Woodburn et al's tube design.

Two sets of three-axis motors were constructed, with slightly different cylindrical vertical sliders. One motor was intended to position an optical fibre, so a fibre clamp mechanism was integrated into the vertical stage (see figure 5.5(a)). This took the form of a phosphor bronze collar that could be tightened around the fibre, to hold it in position. A hole through the centre of the slider allowed insertion of the fibre from rear.

The second motor was used as a coarse positioning mechanism for a tube scanner, mounted on the vertical stage (see figure 5.5(b)). An additional cylinder of machinable glass was glued onto the end of the scan tube to electrically isolate it from any additional attachments. A metal screw hole was located at the end of the cylinder, into which an STM tip or sample mount could be screwed. An electrical connection to the screw hole was made inside the cylinder in order to record tunnel current in STM mode.

During the construction of the motors, it was found that the alignment and cleanliness of the quartz rods was critically important. The rods on each stage were required to be exactly parallel to each other; otherwise the slider exhibited a rocking motion rather than the desired slip/stick action. Motor stages that stopped working after a period of operation, were generally found to have dirty quartz rods. A thorough clean with a mild solvent such as isopropyl alcohol generally corrected the problem. A misaligned rod, or a small amount of glue stuck to the region of the rod in contact with a V-groove, was generally the cause of motors that failed to work first time. The glue could usually be carefully removed with a scalpel without damaging the rod; however misaligned rods required removal, replacement and then re-gluing.

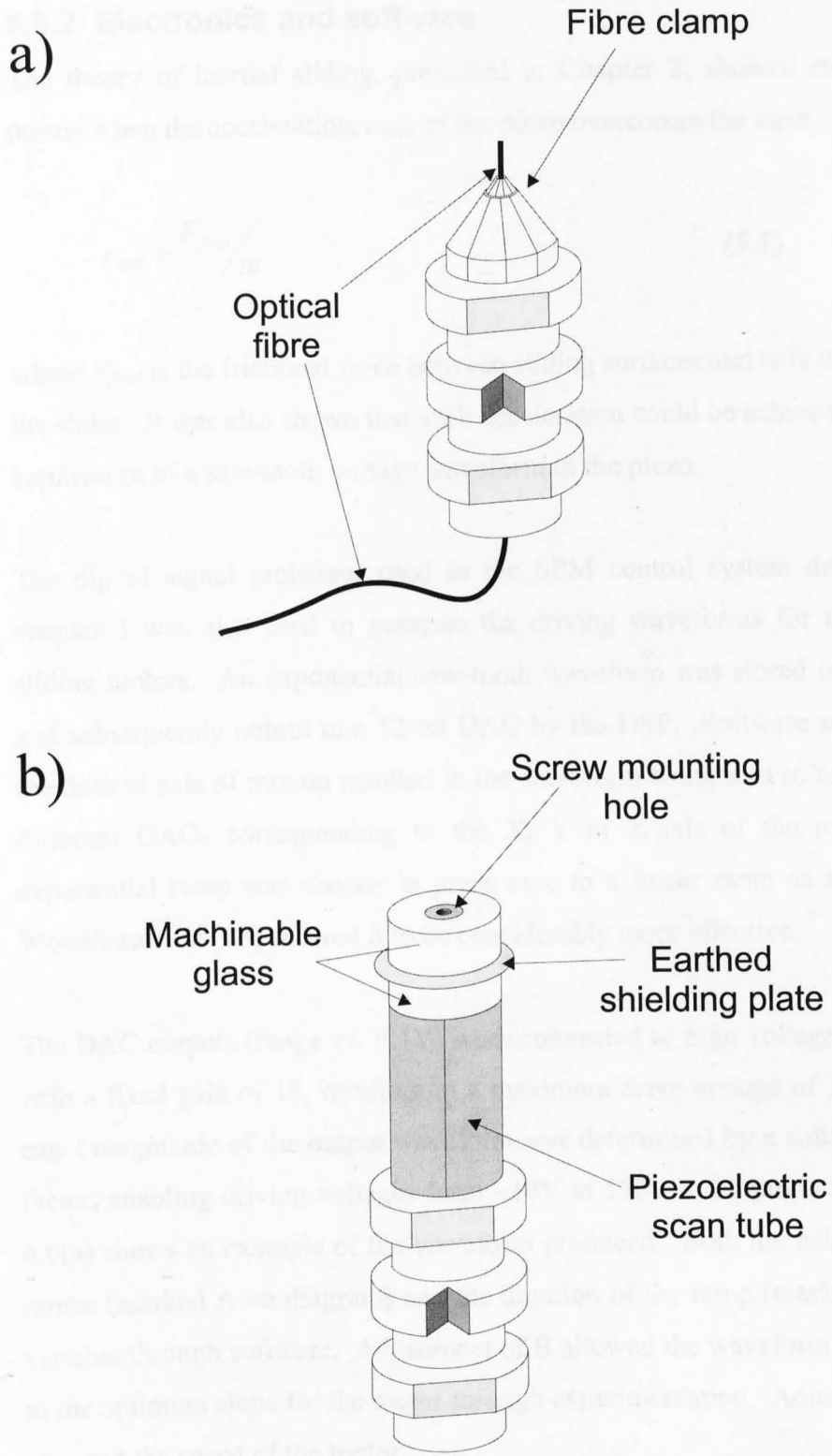

Figure 5.5 *Vertical slider attachments. a) Optical fibre clamp mechanism, used to position optical fibre interferometer. b) Piezoelectric tube scanner attached to vertical slider. Mounting hole used to attach a sample or STM tip to scanner.*

5.3.2 Electronics and software

The theory of inertial sliding, presented in Chapter 2, showed that sliding occurs when the acceleration, a_{crit}, of the piezo overcomes the ratio

$$a_{crit} > {}^{F_{fricf}}\!/_{m} \qquad (5.1)$$

where F_{fricf} is the frictional force between sliding surfaces and m is the mass of the slider. It was also shown that such acceleration could be achieved with the application of a saw-tooth voltage waveform to the piezo.

The digital signal processor used in the SPM control system described in chapter 3 was also used to generate the driving waveforms for the inertial sliding motors. An exponential saw-tooth waveform was stored in an array, and subsequently output to a 12-bit DAC by the DSP. Software selection of the desired axis of motion resulted in the waveform being sent to one of three different DACs corresponding to the X, Y or Z-axis of the motor. An exponential ramp was chosen in preference to a linear ramp as analysis by Woodburn et al [13] showed it to be considerably more effective.

The DAC outputs (range +/- 8.1V) were connected to high voltage amplifiers with a fixed gain of 18, resulting in a maximum drive voltage of 150V. The exact magnitude of the output waveform was determined by a software scale-factor, enabling driving voltages from ~10V to 150V to be produced. Figure 4.6(a) shows an example of the waveform produced. Both the delay between ramps (marked A on diagram) and the duration of the ramp (marked B) were variable through software. Adjustment of B allowed the waveform to be tuned to the optimum slope for the motor through experimentation. Adjustment of A changed the speed of the motor.

Whilst developing the motor driving electronics, it was found that the slew rate of the high voltage amplifiers was not sufficient to produce the acceleration required to initiate sliding. To overcome this, a second stage was added to the electronics to rapidly short the output voltage to ground, therefore

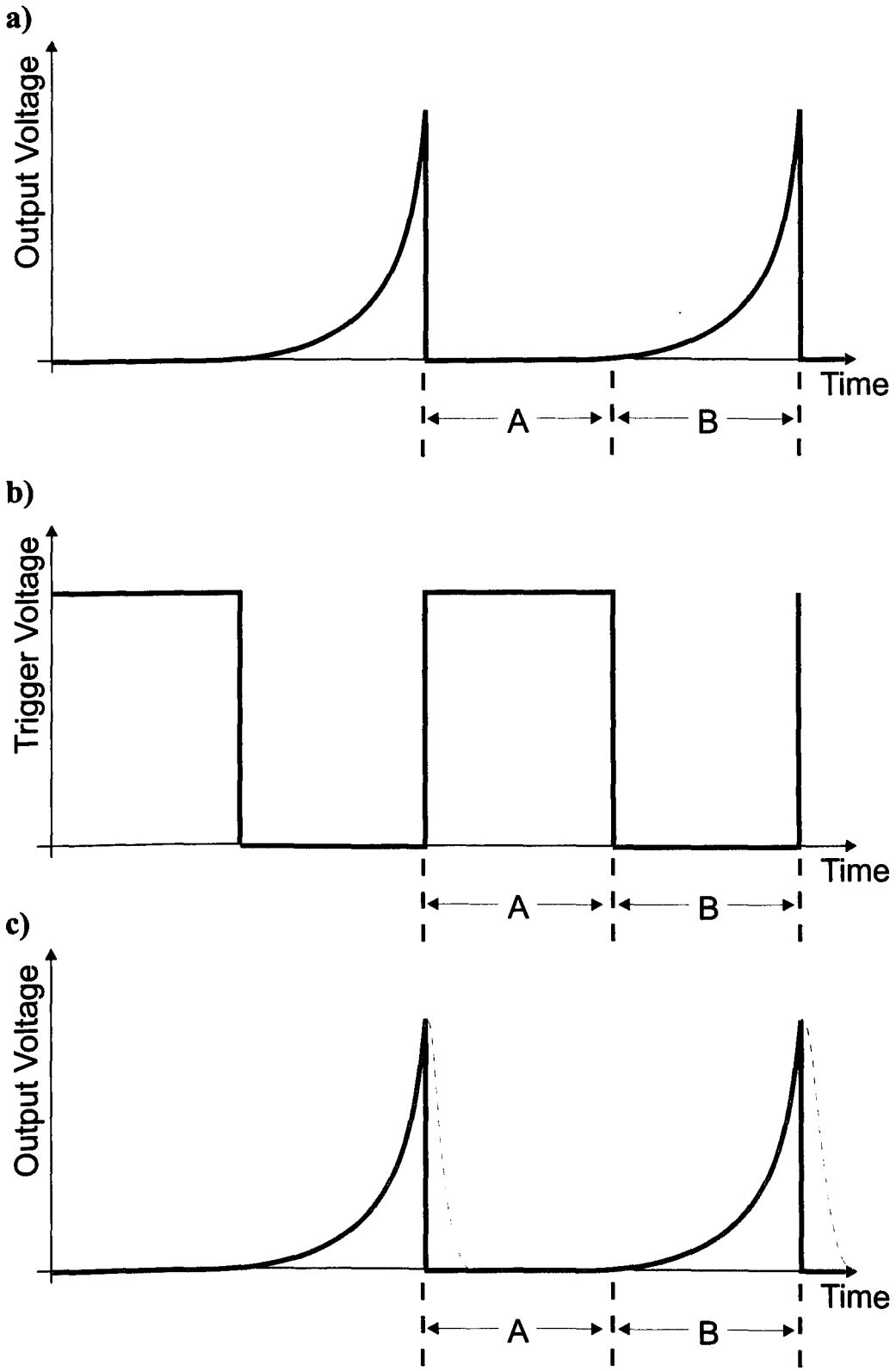

Figure 5.6 *Driving waveform applied to inertial sliding motors. a) Waveform output from DSP card. b) Trigger signal to shorting circuit. c) Result of shorting circuit on output signal. Dotted line shows output without shorting circuit, solid red line shows output with short. Period marked A= delay between ramps, B=period of ramp.*

creating the required acceleration. This second stage consisted of a fast field effect transistor that shorted the output from the high voltage amplifier to ground when a trigger signal was applied. Figure 5.6(b) shows the timing of the trigger signal relative to the waveform. This trigger signal was also produced by the DSP.

Figure 5.6(c) shows a schematic of the effect of the addition of the shorting circuit. The dotted blue line represents the slow response of the high voltage amplifiers, while the solid red line represents the output when the shorting circuit is used. Addition of the circuit reduced the total time for the signal to decay to zero from ~100μs to <500ns.

It is important to note that it is not the rate of decay of the signal that is critical to the operation of the motors. The critical feature of the waveform is actually the rate of change of the gradient, as this is equivalent to acceleration of the piezo. To clarify, figure 5.7 shows the position, velocity and acceleration of an ideal piezo (i.e. applied voltage equates directly to position, with zero response time) when the waveform in figure 5.6 is applied.

Graphs a, b and c show an expansion of the region marked with a green circle on the inset. The three coloured lines show the effect of different shorting transistor response times. The black line represents the ideal response; there is an immediate change at the moment the trigger is applied (marked P in graph a). There is a discontinuity in the velocity as it changes from positive to negative (graph b), and an infinite spike in the acceleration.

The red line represents a fast transistor in the shorting circuit. There is a slight delay in the positional response to the trigger as the transistor switches on. There is no longer a discontinuity in the velocity graph (b), and the acceleration has a finite peak, reaching a value of a_{max}. The blue line demonstrates the response of a slow transistor; the acceleration is now a broad, low peak whose maximum does not exceed a_{crit}, the acceleration required to initiate sliding.

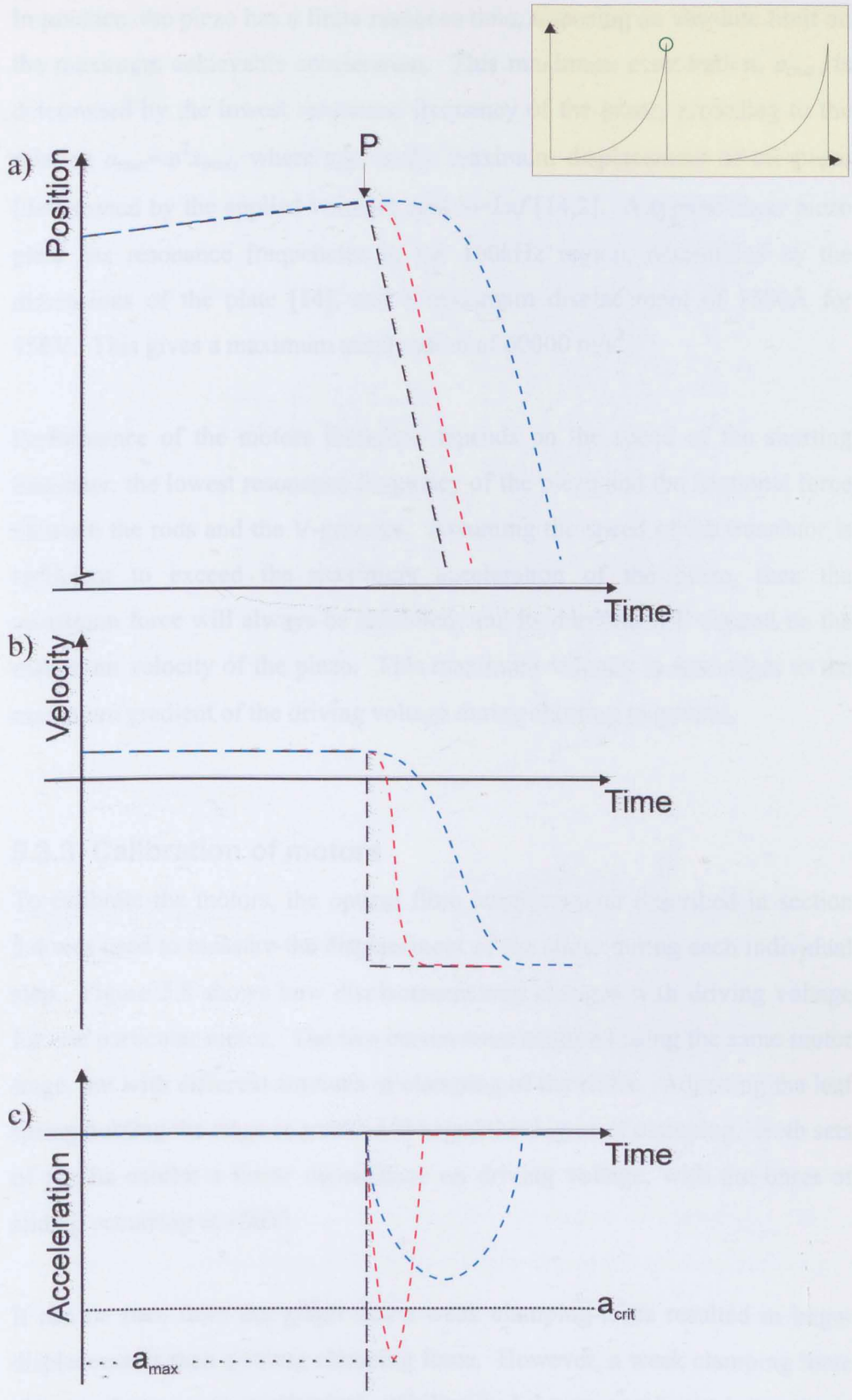

Figure 5.7 *Graphs showing the variation of position, velocity and acceleration of the surface of a shear piezo plate during the period marked by a green circle on the insert*

In practice, the piezo has a finite response time, imposing an absolute limit on the maximum achievable acceleration. This maximum acceleration, a_{max}, is determined by the lowest resonance frequency of the piezo, according to the relation $a_{max}=\omega^2 x_{max}$, where x_{max} is the maximum displacement of the piezo (determined by the applied voltage), and $\omega=2\pi f$ [14,2]. A typical shear piezo plate has resonance frequencies in the 100kHz region, determined by the dimensions of the plate [14], and a maximum displacement of 1500Å for 150V. This gives a maximum acceleration of 60000 m/s^2.

Performance of the motors therefore depends on the speed of the shorting transistor, the lowest resonance frequency of the piezo and the frictional force between the rods and the V-grooves. Assuming the speed of the transistor is sufficient to exceed the maximum acceleration of the piezo, then the maximum force will always be exhibited, and its duration will depend on the maximum velocity of the piezo. This maximum velocity is equivalent to the maximum gradient of the driving voltage during shorting to ground.

5.3.3 Calibration of motors

To calibrate the motors, the optical fibre interferometer described in section 5.4 was used to measure the displacement of the slider during each individual step. Figure 5.8 shows how displacement/step changes with driving voltage for one particular motor. The two curves were acquired using the same motor stage, but with different amounts of clamping of the slider. Adjusting the leaf spring holding the stage in position changed the degree of clamping. Both sets of results exhibit a linear dependence on driving voltage, with the onset of sliding occurring at ~50V.

It can be seen from the graph that a weak clamping-force resulted in larger displacements than a strong clamping force. However, a weak clamping force also produces poor mechanical stability and lower mechanical resonance frequencies. Therefore, the maximum clamping possible without preventing sliding motion was used for all axes of the motor. Kleindiek et al [14]

estimated this force from the maximum acceleration of the piezo (60000 m/s^2 from the previous calculation). Assuming a co-efficient of friction of 1, at the point of slipping, $a_{max} = f_{clamp}/m$, where f_{clamp} is the clamping force, and m is the mass of the slider (~2 grams). So the clamping force exerted by the leaf spring must not exceed 60000m/s^2 x 0.002kg = 120N. In practice the maximum force is considerably less than 120N as imperfections in the sliding surfaces increase the coefficient of friction, preventing sliding.

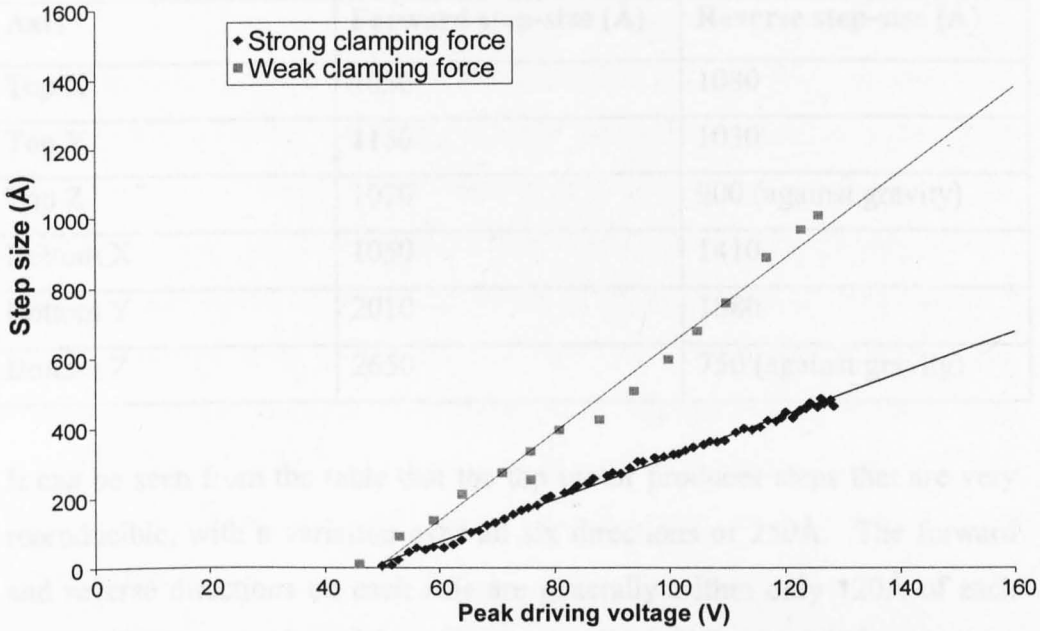

Figure 5.8 *Graph of step-size versus driving voltage for two different clamping forces.*

The vertical axis of each motor must also overcome the effects of gravity on the slider. An additional downward force due to gravity acting on the slider modifies the distance moved per step for a given driving voltage. Steps in the upward direction (against gravity) are smaller than those in the downward direction, with the difference determined by the degree of clamping. This is because the clamping force also plays a more important role on the vertical axis than on the other two axes, as it must be sufficient to prevent gravity alone initiating sliding motion. If too little clamping force is applied, vibrations caused by the motion of the driving piezo result in a downward motion of the slider, independent of the sign of the driving voltage.

The average step-size for each axis of motion was measured with the motors in their final configuration, mounted on the SPM head. A series of 1000 steps was applied to each axis, in both directions, and the distance travelled was recorded. The drive waveform was identical to that used during operation of the microscope, with an amplitude of 150V, and timings as shown in figure 5.6(b). This was repeated several times to ensure reproducibility. The table below summarises the results obtained:

Axis	**Forward step-size (Å)**	**Reverse step-size (Å)**
Top X	1050	1080
Top Y	1150	1030
Top Z	1070	900 (against gravity)
Bottom X	1050	1410
Bottom Y	2010	1880
Bottom Z	2650	750 (against gravity)

It can be seen from the table that the top motor produces steps that are very reproducible, with a variation over all six directions of 250Å. The forward and reverse directions on each axis are generally within only 120Å of each other, with the exception of the vertical axis, which differs by 170Å.

The bottom motor does not perform quite as well. Here, there is a range of nearly 2000Å between all six directions, considerably more than for the top motor. It is thought that the poor performance is a result of inadequate repairs made to the motor, which may have resulted in poor alignment of the rods and insufficient clamping. In particular, the vertical axis was found to have a range of step sizes, dependent on the position of the slider along the rods. This suggests that one end of the rods is closer together than the other, producing an uneven clamping force. Further repairs to the bottom motor should produce step-sizes similar to those observed for the top stage.

Due to the success of the motors, a further set has been made for a photon emission STM being developed within our group by P. Moriarty. This new set

of motors is routinely operated under UHV conditions with no noticeable decrease in performance. In addition, a further six motors are also in production for various other projects.

5.4 Optical fibre interferometer

Scanning force microscopes require a method of displacement detection with a resolution of <1Å to monitor the position of a cantilever probe. Early AFMs used a tunnelling sensor to detect displacement [17], however this proved to be non-ideal as interactions between the tunnelling sensor and cantilever caused anomalous results. More recently, two optical methods have become commonly used. The first technique uses a position sensitive photo-detector, such as a quadranted photodiode or bicell, to detect changes in the position of a laser beam reflected off a cantilever [see figure 5.9(a) and ref. 18]. The second technique employs heterodyne (dual frequency) [19] or homodyne (single frequency) [20,21,22] laser interferometry, the most recent of which [22] utilises a diode laser and optical fibre arrangement as described in the next section.

Provided that the amplitude of cantilever motion is much less than the wavelength of laser light, homodyne interferometry provides an excellent method of displacement sensing. In such an interferometer, light from a single wavelength laser is split into two coherent beams. The two beams of light interfere with each other either constructively or destructively, depending on the optical path difference between them. Changes in optical path difference result in changes in detected intensity; therefore displacements can be measured as variations in intensity.

5.4.1 Description of system

Early interferometer arrangements for AFM used a He-Ne laser and standard optical components to split the laser beam and to focus it onto the cantilever [20]. This arrangement was susceptible to any vibrations and air currents

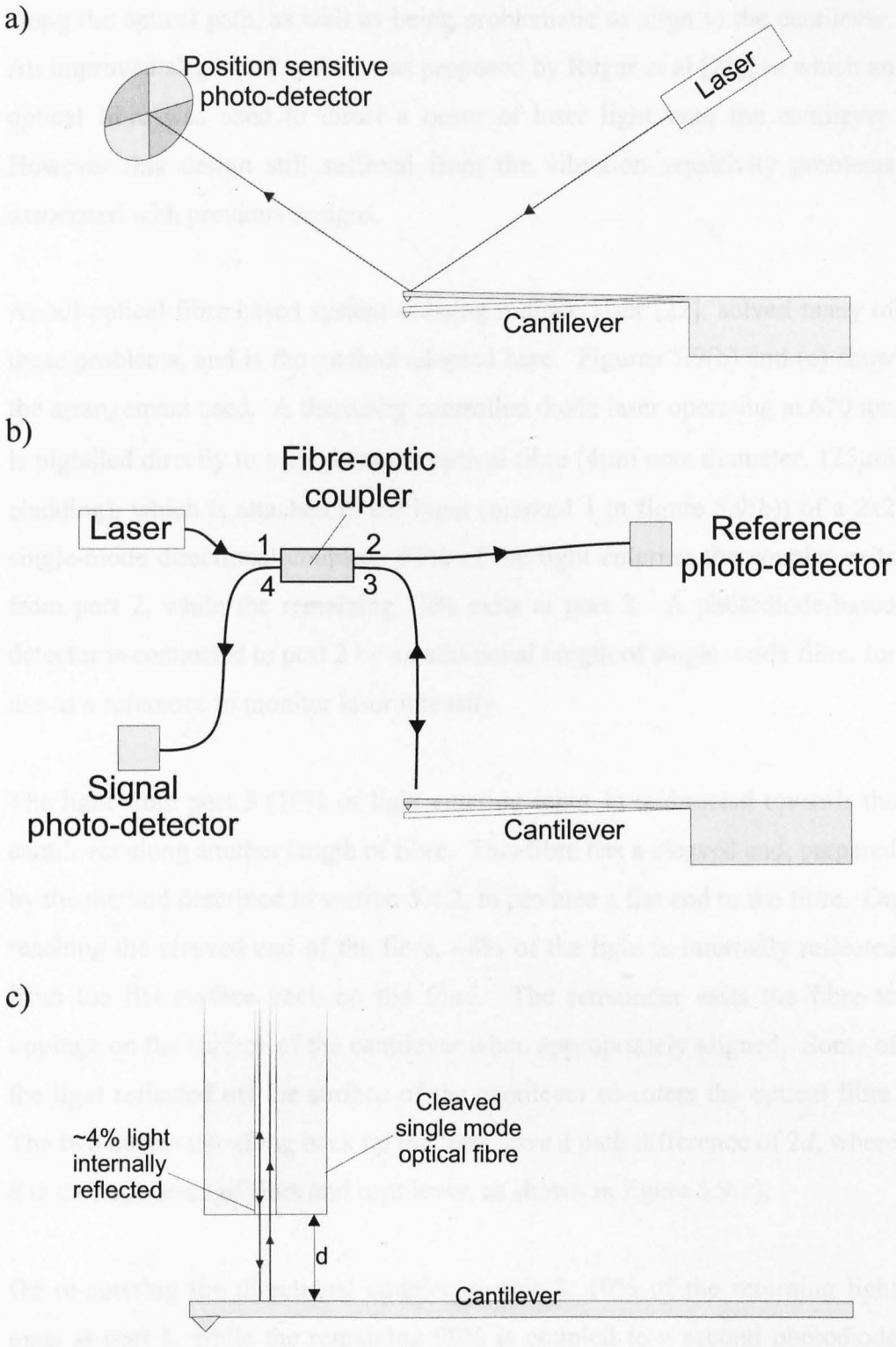

Figure 5.9 *Methods used for detection of cantilever motion in AFM. a) Position sensitive photo-detector used to sense deflection of laser beam. b) Optical fibre-based interferometer sensor. c) Close-up of optical fibre interferometer. ~4% of light is reflected back from the end of the fibre, the remainder exits fibre to illuminate cantilever. Some light is reflected back into fibre and interferes with internally reflected beam.*

along the optical path, as well as being problematic to align to the cantilever. An improved alignment system was proposed by Rugar et al [21], in which an optical fibre was used to direct a beam of laser light onto the cantilever. However this design still suffered from the vibration sensitivity problems associated with previous designs.

An all-optical fibre based system utilising a diode laser [22], solved many of these problems, and is the method adopted here. Figures 5.9(b) and (c) show the arrangement used. A thermally controlled diode laser operating at 670 nm is pigtailed directly to a single mode optical fibre (4μm core diameter, 125μm cladding), which is attached to the input (marked 1 in figure 5.9(b)) of a 2x2 single-mode directional coupler. 90% of the light entering the coupler exits from port 2, while the remaining 10% exits at port 3. A photodiode-based detector is connected to port 2 by an additional length of single mode fibre, for use as a reference to monitor laser intensity.

The light from port 3 (10% of light entering input 1) is directed towards the cantilever along another length of fibre. This fibre has a cleaved end, prepared by the method described in section 5.4.2, to produce a flat end to the fibre. On reaching the cleaved end of the fibre, ~4% of the light is internally reflected from the flat surface back up the fibre. The remainder exits the fibre to impinge on the surface of the cantilever when appropriately aligned. Some of the light reflected off the surface of the cantilever re-enters the optical fibre. The two beams travelling back up the fibre have a path difference of $2d$, where d is the separation of fibre and cantilever, as shown in figure 5.9(c).

On re-entering the directional coupler at port 3, 10% of the returning light exits at port 1, while the remaining 90% is coupled to a second photodiode detector via port 4. At the photodiode, the two beams interfere causing variations in photodiode current, i, according to:

$$i = i_0 (1 - V\cos(4\pi d / \lambda)) \qquad (5.2)$$

where λ is the laser wavelength, d is the fibre-cantilever separation, V is the fringe visibility, given by $V = (i_{max} - i_{min}) / (i_{max} + i_{min})$, and i_0 is the midpoint current, given by $i_0 = (i_{max} + i_{min}) / 2$. The values i_{max} and i_{min} are the currents corresponding to maximum constructive and destructive interference respectively.

The system is operated at a point where d = $\lambda/8$, $3\lambda/8$, $5\lambda/8$... At this point, the phases of the two interfering beams are in quadrature, i.e. there is $\pi/2$ phase difference between them. At quadrature, small changes in distance, Δd, wavelength $\Delta\lambda$ and midpoint current Δi_0 (caused by fluctuations in laser intensity) result in a change in photodiode current according to:

$$\Delta i = i_0\left(4\pi V\frac{\Delta d}{\lambda} - 4\pi dV\frac{\Delta\lambda}{\lambda^2}\right) + \Delta i_0 \qquad (5.3)$$

Assuming $\Delta\lambda$ and Δi_0 are small, this can be re-arranged to give:

$$\frac{\lambda\Delta i}{4\pi V i_0} = \Delta d + \delta \qquad \text{where the noise, } \delta = \frac{\lambda\Delta i_0}{4\pi V i_0} - \frac{d\Delta\lambda}{\lambda} \qquad (5.4)$$

5.4.2 Interferometer sensitivity and noise sources

It can be seen from equation 5.4 that wavelength noise increases linearly with cantilever-fibre separation, so operation as close to the cantilever as possible produces the optimum signal to noise ratio. This has been confirmed experimentally by Rugar et al [22]. Typically a fibre-cantilever spacing of <4μm is used. The effect of intensity variations, Δi_0, can be significantly reduced by subtracting the reference photocurrent (from port 2 of the coupler) from the signal photocurrent. This effectively cancels the Δi_0 term in equation 5.4, leaving wavelength noise as the dominant noise source.

Light emitted from a diode laser has a short (~mm) coherence length, whereas He-Ne laser light has a much longer (~m) coherence length. This means that

the optical fibre interferometer does not suffer from low frequency instability caused by stray reflections within the optical fibre observe with HeNe systems [21]. The lack of air paths within the instrument (apart from the gap fibre-cantilever gap) also reduces its sensitivity to acoustic vibrations and air currents, a further improvement on previous open-air designs.

The photodiode current (~1nA) is converted to a voltage and amplified using a two-stage operational amplifier arrangement similar to that used in the tunnel current amplifier described in chapter 3. Large gains (~10^9) are required due to the very low light levels at the signal photodiode. It was found that higher laser intensities resulted in instability and mode hopping due to back-reflected light entering the laser. Therefore, the laser intensity was reduced to a point just above the onset of lasing to minimise the level of light re-entering the laser.

More recent papers in which an optical fibre interferometer is used have added a solid state Faraday optical isolator between the diode laser and optical fibre system [24,25]. This component reduces back-reflection into the laser without significantly reducing the intensity of light emitted from the laser, solving the problem of laser instability due to back-reflection. However, the present arrangement of laser, optical fibre, and operating wavelength (670nm) prevent such a component from being added to our system. Thus the only option was to reduce laser power.

To measure the noise level of the interferometer system, the cleaved fibre was positioned <4μm away from a silicon wafer. The wafer was driven to oscillate with an rms amplitude of 1.1Å at a frequency of 1kHz. Using a lock-in amplifier, the output from the signal photodiode amplifier was measured. With a 1 second time constant, the rms noise level on the signal was 0.1Å. Measurement bandwidth, $\Delta\nu$, is given by $1/(4T_L)$, where T_L is the lock-in time constant [23,41]. For T_L = 1s, $\Delta\nu$ = 0.25Hz, which leads to an interferometer sensitivity of $0.2\,\text{Å}/\sqrt{Hz}$ at 1kHz. Other examples of optical fibre interferometers have exhibited noise levels of typically 10^{-2}-$10^{-3}\,\text{Å}/\sqrt{Hz}$

[41,42] with levels as low as $5.5x10^{-4} \mathring{A}/\sqrt{Hz}$ reported at higher frequencies [22], indicating that our system has significantly poorer sensitivity.

Replacement of the diode laser with an integrated diode laser and Faraday isolator is likely to improve the stability of the system and therefore increase the sensitivity. In addition, use of higher intensity light will decrease the level of photocurrent amplification required, improving signal to noise ratios

5.5 Sample/cantilever stage

Each mode of SPM utilises a different interaction between probe and surface. Most SFM modes, such as AFM and MFM measure cantilever motion, whereas STM measures tunnel currents. In order to function as a STM, SFM, and eventually a MRFM without major modifications, the central stage (stage 2 in figure 5.2) on the SPM head must be capable of performing several different tasks. To facilitate this, the design shown in figure 4.10 has been produced. A removable holder has been machined to slide into V-grooved tracks attached to the Al stage. This holder can be used to as a mount for a cantilever or an STM sample without modification. Different holders can be produced if required for other, as yet untested, modes of operation.

In AFM mode, the holder contains a cantilever, whose displacement is monitored by the optical fibre interferometer (described in the previous section) controlled by the motors on stage 1. The sample is mounted on the scan tube controlled by the second set of motors on stage 3. See section 5.7 for results obtained in this mode.

In STM mode, the holder contains the sample rather than a cantilever, and the STM tip is mounted on the scan tube on stage 3. Stage 1 is unused in STM mode. A bias can be applied to the sample by utilising the spare connector on the connection block mounted on stage 2. Connection to the STM tip is made

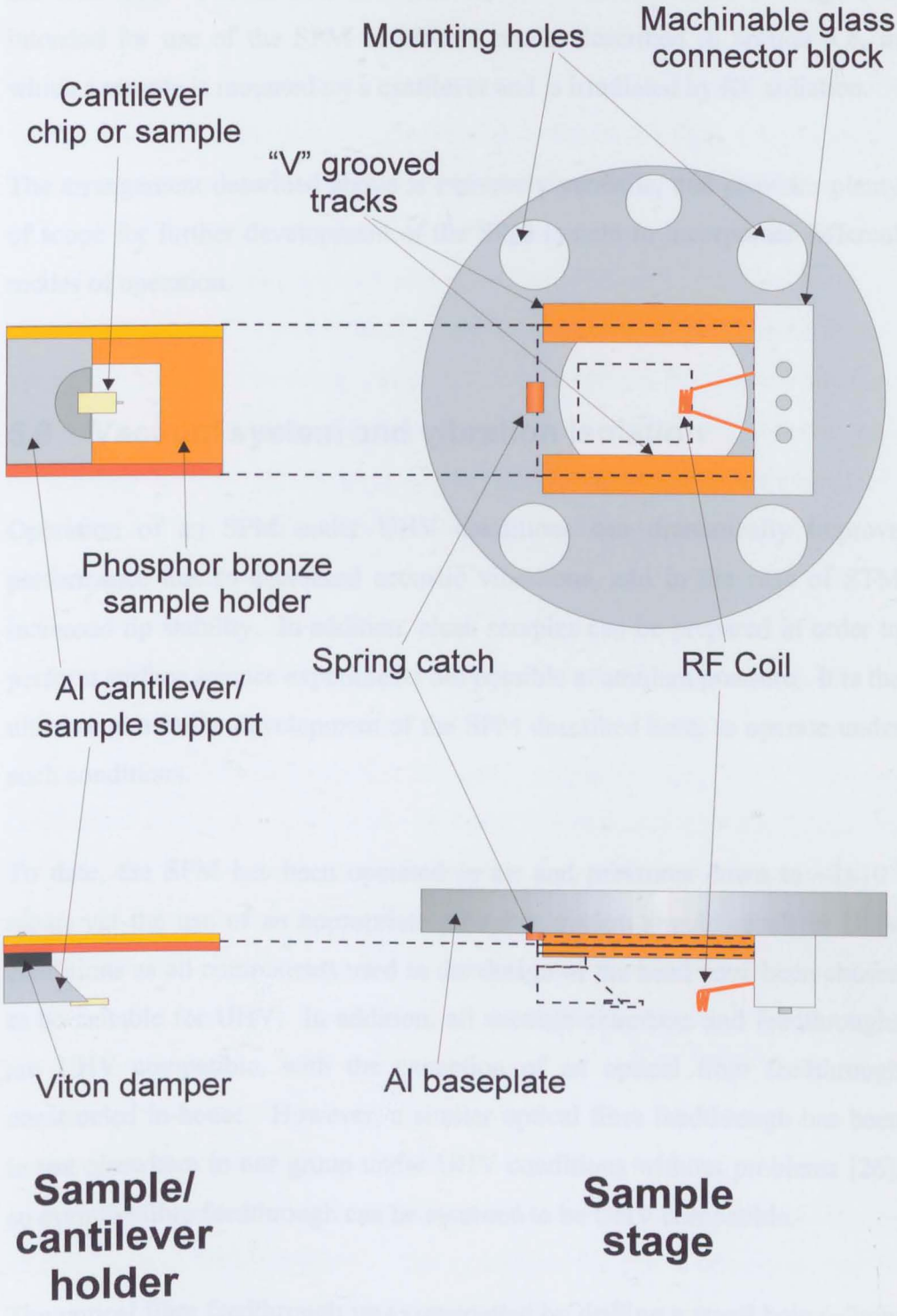

Figure 5.10 *Schematic of sample/cantilever stage and holder. The holder can be removed for easy sample exchange. RF coil is used in MRFM experiments (see section 5.8)*

via the mounting screw that has a wire attached, running along the inside of the scan tube. The RF coil connected to the connector block on stage 2 is intended for use of the SPM in MRFM mode, described in section 5.8, in which a sample is mounted *on* a cantilever and is irradiated by RF radiation.

The arrangement described above is extremely versatile, and provides plenty of scope for further development of the SPM system to incorporate different modes of operation.

5.6 Vacuum system and vibration isolation

Operation of an SPM under UHV conditions can dramatically improve performance due to decreased acoustic vibrations, and in the case of STM increased tip stability. In addition, clean samples can be prepared in order to perform surface science experiments not possible at ambient pressure. It is the ultimate aim in the development of the SPM described here, to operate under such conditions.

To date, the SPM has been operated in air and pressures down to ~$1x10^{-3}$ mbar, yet the use of an appropriate pumping system should result in UHV conditions as all components used in the design of the head have been chosen to be suitable for UHV. In addition, all vacuum chambers and feedthroughs are UHV compatible, with the exception of an optical fibre feedthrough constructed in-house. However, a similar optical fibre feedthrough has been in use elsewhere in our group under UHV conditions without problems [26], so even the fibre feedthrough can be assumed to be UHV compatible.

The optical fibre feedthrough was constructed by drilling a small hole (~2mm diameter) through a blank stainless steel UHV flange. After removal of the layers of plastic cladding from an optical fibre, it was inserted through the hole and glued with vacuum compatible epoxy. A small mechanical support was attached to the outside of the flange to prevent damage to the glued region

through movement of the fibre. The flange was then attached to the UHV chamber as normal.

The layout of the vacuum system was shown in figure 5.1 (in section 5.2), and so will not be reproduced here. Please refer to figure 5.1 during the following description of the system. Three feedthroughs are mounted on a six-port chamber. The first is a 50-way multi-pin feedthrough used to provide electrical connections to the two sets of motors, plus any additional electrical signals required. The second feedthrough is coaxial and can be used for low strength signals such as tunnel current. It is also used to provide a connection to the RF coil for MRFM experiments. A UHV compatible 50Ω coaxial cable is attached to the vacuum side of the feedthrough to provide impedance matched path for the RF signal. The third feedthrough is the optical fibre feedthrough described above.

The remaining horizontal port contains a reduction flange connected to a screw valve and then to a set of sorption pumps. The top port currently contains a set of edge-welded bellows, originally part of a clamping mechanism that is no longer used. This port is effectively now blank, with the SPM head support rods screwed into it. A winch hook is mounted on extended bolts clamping the flange to the chamber. The hook allows connection of the whole vacuum system to a ceiling-mounted winch system in order to raise or lower the system into or out of the magnet.

The final port on the six-port chamber connects to the 50mm diameter vacuum can that fits down the bore of the magnet. A viton gasket is used to seal the joint between the vacuum can and chamber rather than the oxygen free copper gaskets used in the other joints. This is because the can is often removed for sample exchange, cantilever alignment etc. When removed from the can, the SPM head can be viewed using a CCD camera system with a magnification of ~80x to allow easy alignment of the optical fibre and cantilever.

The whole vacuum system is mounted on a platform supported by pneumatic legs to provide vibration isolation. The legs have a resonant frequency of ~1Hz therefore providing effective isolation from vibrations at frequencies above this (see chapter 2 for discussion of vibration isolation).

An additional stage of vibration isolation was originally included in the system. A set of viton-damped springs was used to isolate the head from the support rods, but this resulted in the introduction of a swinging mode of oscillation that was poorly damped. In addition, it was found that the very small tolerances between the diameter of the SPM head and the inside of the vacuum can resulted in the head touching the sides of the can at certain points. The overall result was that the second stage of vibration isolation was ineffective, and could even introduce vibration if the swinging mode was excited. The results in the next section show that the single stage of vibration isolation employed is sufficient for most SPM applications.

5.7 Results

In this section a selection of results obtained using the SPM head are presented. The measurements are intended to demonstrate the initial functionality of the SPM. Simple modifications to the head could be made to enable the use of numerous alternative SPM techniques, such as MFM, EFM etc. However these results show that the mechanical and electronic design of the head is fully functional.

5.7.1 Contact mode AFM

To operate as a contact mode AFM, a microfabricated cantilever probe with a spring constant of ~0.1N/m and sharp tip must be positioned in physical contact with the surface of interest (see chapter 1 for a detailed description of AFM). The deflection of the cantilever is then monitored as it is scanned across the surface. In constant force mode (the most common mode of operation), a feedback loop is used to maintain a constant deflection of the

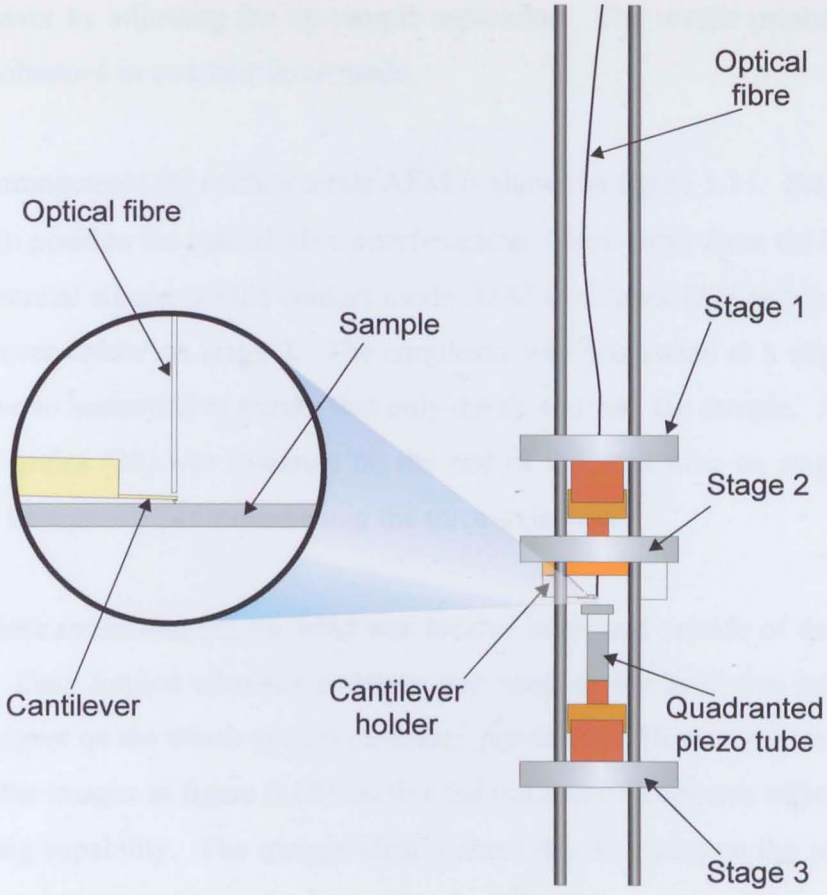

Figure 5.11 *Arrangement for contact mode AFM. Interferometer is mounted on stage 1, cantilever is mounted on stage 2 and sample is mounted on scan tube on stage 3.*

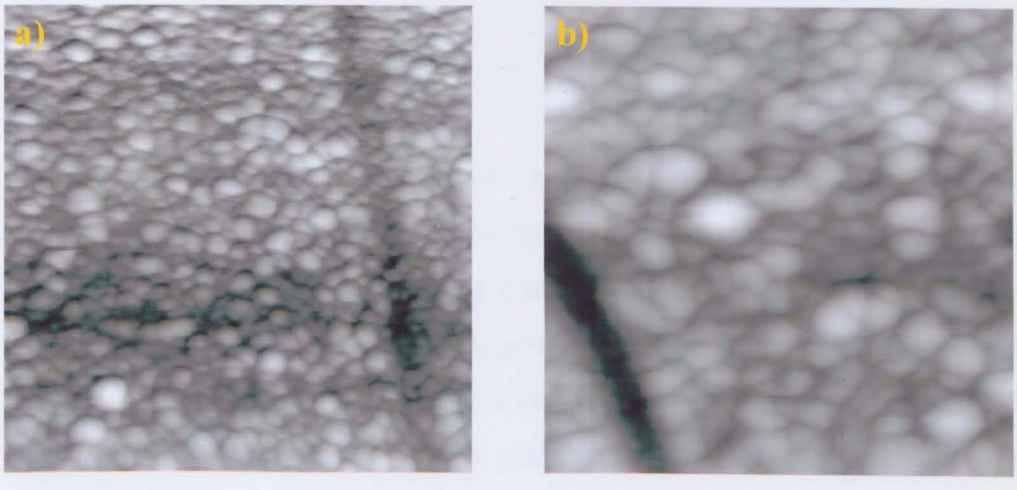

Figure 5.12 *Images of Al grains obtained using the arrangement in figure 5.11. Dark lines are scratches on sample, small bumps are grains of Al.Image dimensions: a) 3x3*μm, b)1x1μm.

cantilever by adjusting the tip-sample separation. The results presented here were obtained in constant force mode.

The arrangement for contact mode AFM is shown in figure 5.11. Stage 1 was used to position the optical fibre interferometer <4μm away from the back of a commercial silicon nitride contact mode AFM cantilever [27] attached to the cantilever holder on stage 2. The cantilever was positioned at a slight angle relative to horizontal to ensure that only the tip touched the sample. A sample of Al grains [28] was mounted on the end of the scan tube on stage 3, and could be coarsely positioned using the three-axis motor.

For these measurements the head was located in air and outside of the magnet bore. Only limited vibration isolation was used, as the head was held above the magnet on the winch system described previously. However it can be seen from the images in figure 5.12 that this did not result in adverse effects on the imaging capability. The images clearly show the Al grains on the surface of the sample. Image a) is of an area ~3 x 3 μm^2 and image b) is of an area ~1 x 1 μm^2. The dark line observed in both images is thought to be a small scratch on the surface. For smaller scale scans, it is anticipated that vibrational noise will become significant, so the system will need to be supported by the pneumatic legs to ensure adequate isolation.

5.7.2 STM mode

To operate in STM mode, only two of the three stages in the head are required. Figure 5.13 shows a schematic of the arrangement. Stage 1 is unused, so the optical fibre is retracted as far as possible. The sample is mounted on a holder inserted into stage 2, with a bias connection made via the connection block on the stage. A PtIr tip is mounted in a stainless steel tip nut screwed into the scan tube situated on stage 3. A wire connected to the metal screw hole makes electrical contact to the tip to measure tunnel current. This signal is then carried along a 50Ω co-axial cable to the co-axial feedthrough. The tunnel current pre-amplifier is connected to the air side of the feedthrough.

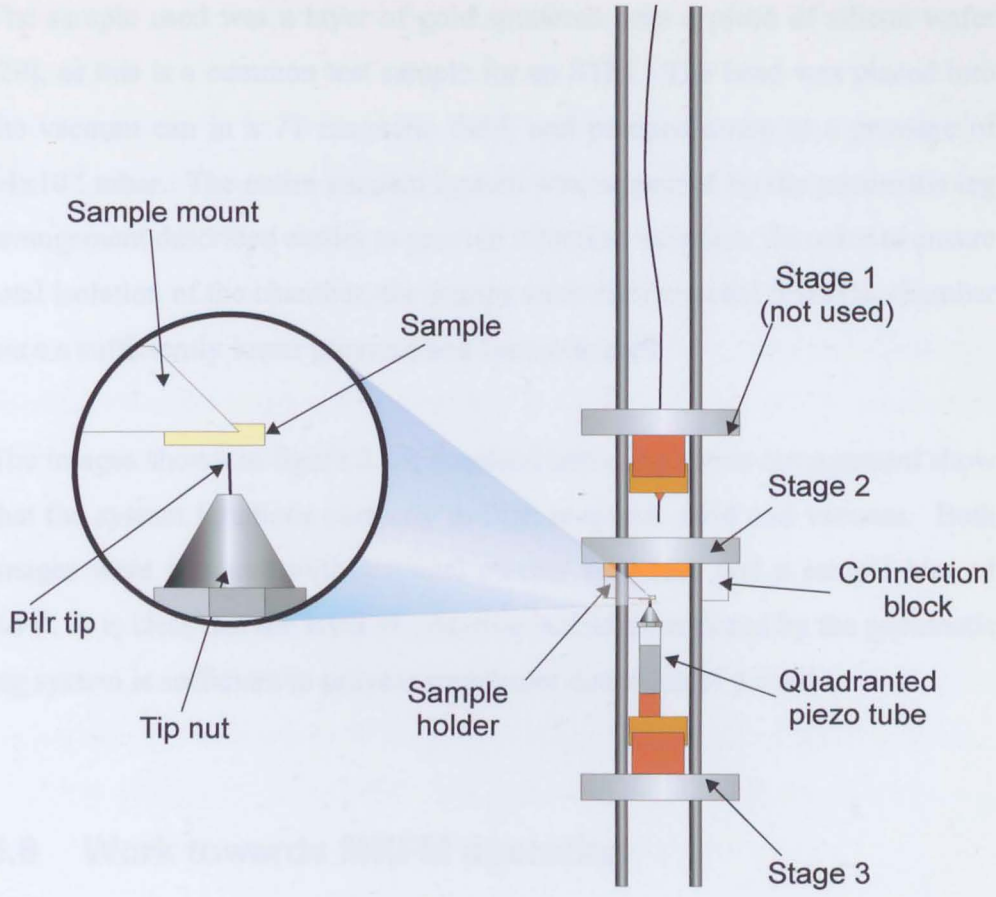

Figure 5.13 *Arrangement for STM mode. Stage 1 is not used, stage 2 contains sample, and a PtIr tip is mounted on the scan tube on stage 3.*

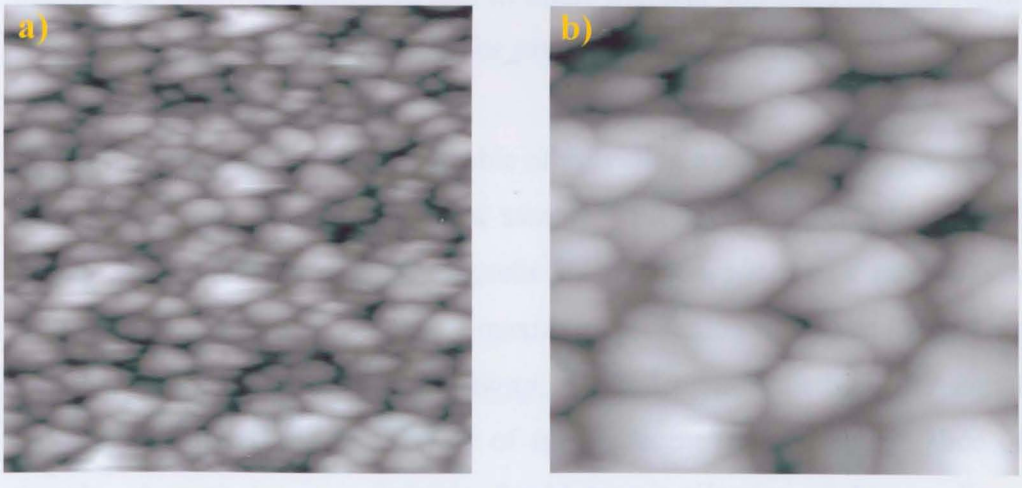

Figure 5.14 *Images of Au sputter-deposited on Si. Images acquired using STM arrangement in figure 4.13. Image dimensions: a) 1x1*μm, b)0.5x0.5μm.

The sample used was a layer of gold sputtered onto a piece of silicon wafer [29], as this is a common test sample for an STM. The head was placed into the vacuum can in a 7T magnetic field, and pumped down to a pressure of $\sim 1 \times 10^{-3}$ mbar. The entire vacuum system was supported by the pneumatic leg arrangement described earlier to provide vibration isolation. In order to ensure total isolation of the chamber, the pumps were disconnected from the chamber once a sufficiently lower pressure had been obtained.

The images shown in figure 5.14, acquired using the above arrangement show that the system functions correctly in high magnetic field and vacuum. Both images were acquired with a tunnel current of 0.1nA and a sample bias of 0.4V. It is clear that the level of vibration isolation produced by the pneumatic leg system is sufficient to prevent significant distortion of a scan.

5.8 Work towards MRFM operation

The principle of nuclear magnetic resonance (NMR) has been employed in experimental techniques for over fifty years [30,31], and has been the basis for a range of imaging methods (magnetic resonance imaging) since the early 1970s [32,33]. During this time, magnetic resonance imaging (MRI) has become an essential diagnostic tool in many medical applications, and NMR spectroscopy an indispensable tool for structural analysis in chemistry.

Magnetic resonance imaging is capable of providing a non-invasive, full three-dimensional map of spins within a sample. Produced by recording NMR signals from a number of thin, magnetically selected, *slices* of a sample (see section 5.8.1), MRI currently has a maximum resolution of $\sim 4\mu m^3$ [34]. This is largely determined by the sensitivity of the detection method; the signal level is determined by the number of spins present in the selected slice of sample. A more sensitive detector should permit selection of thinner slices, and therefore higher resolution spin maps.

A new SPM technique called Magnetic Resonance Force Microscopy has the potential to be sensitive to *individual* proton spins using a combination of NMR and SPM technology. Proposed by Sidles in 1991 [32], the technique has the potential to produce fully three-dimensional non-invasive images on a molecular scale of a huge range of samples from protein molecules to semiconductor dopants. The unprecedented resolution of the technique is due to the use of a micromechanical detector instead of the conventional inductive detection, and the extremely high magnetic field gradients used to select slices of the sample, as discussed in the next section.

5.8.1 Principles of a MRFM

In order to describe the principles of a magnetic resonance force microscope, it is first necessary to summarise the fundamental theory of nuclear magnetic resonance. The following section provides a simple review of NMR principles and their application to MRFM. For a more detailed analysis of NMR, see reference 35, and for a recent review of MRFM see reference 37.

Any nucleus possessing angular momentum, **J**, has a magnetic moment, μ, given by:

$$\mu = \gamma \mathbf{J} \tag{5.4}$$

Where γ is the *gyromagnetic ratio*, and μ and **J** are vectors. Quantum theory states that **J** must be quantised, with a magnitude given by:

$$J = \hbar [\, I (I + 1) \,]^{1/2} \tag{5.5}$$

Where I is either integer or half-integer and is referred to as the spin quantum number, and $\hbar$ is Planck's constant divided by 2π. The component of **J** in the z direction, J_z, is defined as:

$$J_z = \hbar \; m_I \tag{5.6}$$

Where m_I can take values I, I-1,...,-I.

In the presence of a magnetic field, **B**, along the z direction, there will be an interaction between the magnetic moment, μ, and the magnetic field, with an energy, U:

$$U = -\mu.\mathbf{B} = -\mu_z B_0 \qquad (5.7)$$

Where μ_z is the component of the magnetic moment in the z direction, and B_0 is the magnitude of the magnetic field. From equations 5.4 and 5.6, this can be expressed as:

$$U = -\gamma \hbar m_I B_0 \qquad (5.8)$$

The result of equation 5.8 is a series of 2I+1 energy levels, with a separation $\gamma \hbar B_0$, as shown in figure 5.15 for I=3/2.

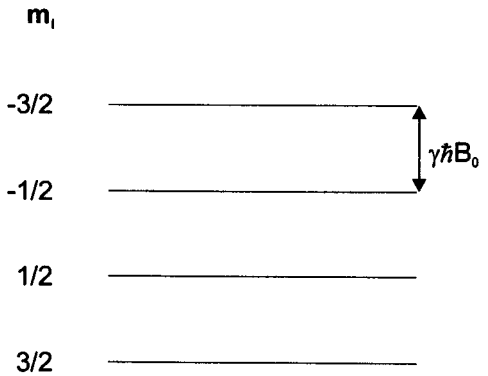

Figure 5.15 *Energy levels for a nucleus with spin 3/2 in a magnetic field B_0 in the z direction.*

Selection rules permit transitions in which $\Delta m_I = +/-1$. So absorption of electromagnetic radiation with energy $\gamma \hbar B_0$ will result in a transition. If the radiation has frequency ω_0, then:

$$\hbar \omega_0 = \Delta U = \hbar \gamma B_0 \quad \text{or}$$

$$\omega_0 = \gamma B_0 \qquad (5.9)$$

Equation 5.9 is the condition for resonance, and is the basis for all NMR experiments.

Any macroscopic sample consists of an ensemble of nuclei, each with a magnetic moment. Consider an ensemble of protons with I = ½, and m_I = +½ or –½. The number of protons in each state, M_I = +½ or -½, is N_+ and N_- respectively, and the total number of protons in the ensemble is constant with a value $N = N_+ + N_-$. At equilibrium, in the presence of a magnetic field, there will be a population difference between the two states, such that:

$$\frac{N_-}{N_+} = e^{-\Delta U / k_B T} = e^{-\gamma \hbar B_0 / k_B T} \qquad (5.10)$$

Where k_B is Boltzmann's constant, T is temperature and ΔU is the energy difference between the levels. This equation suggests that at absolute zero, the sample would be perfectly polarised, with all protons in the m_I = +½ state, and that as temperature is increased, the population difference decreases. At room temperature $\Delta U << k_B T$, so the equilibrium population difference, $n_0 = N_+ - N_-$, can be approximated by:

$$n_0 = N\Delta U/2k_B T = \gamma \hbar N B_0/2k_B T \qquad (5.11)$$

It can be shown that any perturbation from equilibrium will be restored according to:

$$n(t) = n_0 + Ae^{-t/T_1} \qquad (5.12)$$

Where $n(t)$ is the population difference at time t, A is the deviation from equilibrium given by $A = n(0) - n_0$, and T_1 is a constant referred to as the spin-lattice relaxation time.

NMR experiments measure the changes in the magnetisation, **M**, of a sample, which is simply the sum of all the magnetic moments contained within it. So,

an ensemble of protons in a static magnetic field along the z direction has a magnetizastion:

$$\mathbf{M} = N_+\mu_+ + N_-\mu_- \qquad (5.13)$$

Where μ_+ and μ_- are the magnetic moments of the $m_I = +1/2$ and $-1/2$ states respectively. At equilibrium, $\mu_{z+} = -\mu_{z-} = 1/2\gamma\hbar$ (from equations 5.4 and 5.6), and $n = N_+ - N_-$, equation 5.13 can be simplified to:

$$M_0 = \tfrac{1}{2}\gamma\hbar n \qquad (5.14)$$

It is also useful to consider a classical model of magnetic resonance. A magnetic moment, μ, in a magnetic field, **B**, will experience a torque given by $\mu \times \mathbf{B}$. In other words, the magnetic moment will tend to rotate to be aligned with the magnetic field. If the magnetic moment also possesses angular momentum, **J**, then the rate of change of angular momentum is:

$$d\mathbf{J}/dt = \mu \times \mathbf{B} \qquad (5.15)$$

Substituting for **J** using equation 5.4 gives:

$$d\mu/dt = \mu \times (\gamma\mathbf{B}) \qquad (5.16)$$

This represents a precession of the magnetic moment around **B**. To analyse the motion further, it is helpful to change to a rotating frame of reference.

Consider a rotating co-ordinate system, rotating with angular velocity Ω. It can be shown [35] that equation 5.16 holds in the rotating reference frame if **B** is replaced by an effective field, $\mathbf{B}_{eff}$, given by:

$$\mathbf{B}_{eff} = \mathbf{B} + \Omega/\gamma \qquad (5.17)$$

If **B** is chosen to be along the z-axis, with a magnitude B_0, as before, and Ω is chosen to be parallel to **B**, μ will be stationary in the rotating reference frame when $\mathbf{B}_{eff} = 0$. This occurs when $\Omega = -\gamma B_0 \mathbf{k}$, where **k** is a unit vector in the z direction. This result is identical in magnitude to the condition for resonant absorption, given in equation 5.9. The negative sign simply indicates the direction of rotation, and for convenience the z component of Ω, Ω_z is often replaced by ω, where $\Omega_z = -\omega$.

The rotating frame of reference is particularly useful in analysis of the effect of an oscillating magnetic field. Consider a field, $\mathbf{B_1}$, rotating at a rate ω. In the laboratory reference frame, the x component of such field has the form $B_{1x}(t) = B_{1x}(0) \cos \omega t$. However, in a reference frame rotating at ω, the field is static along the x-axis, with a magnitude B_1.

If this alternating magnetic field is applied in addition to B_0, the effective field in the rotating frame now becomes:

$$\mathbf{B}_{eff} = B_1\mathbf{i} + (B_0 - \omega/\gamma)\mathbf{k} \qquad (5.18)$$

Where **i** and **k** are unit vectors along the x and z-axes respectively. The magnetic moment, μ, now precesses around the effective field with angular frequency $\gamma\mathbf{B}_{eff}$. At resonance, $\omega = \omega_0$, therefore $\mathbf{B}_{eff}$ is static along the x-axis, with magnitude B_1. As a result, μ rotates around the x-axis in the y-z plane with angular frequency γB_1, as shown in figure 5.16(b).

μ can be rotated by any chosen angle, θ, with the application of B_1 for a duration t_w, such that:

$$\theta = \gamma B_1 t_w \qquad (5.19)$$

After the application of B_1, $\mathbf{B}_{eff} = \mathbf{B_0}$, and so μ precesses around the z-axis at a rate γB_0, tracing out a cone with half-angle θ.

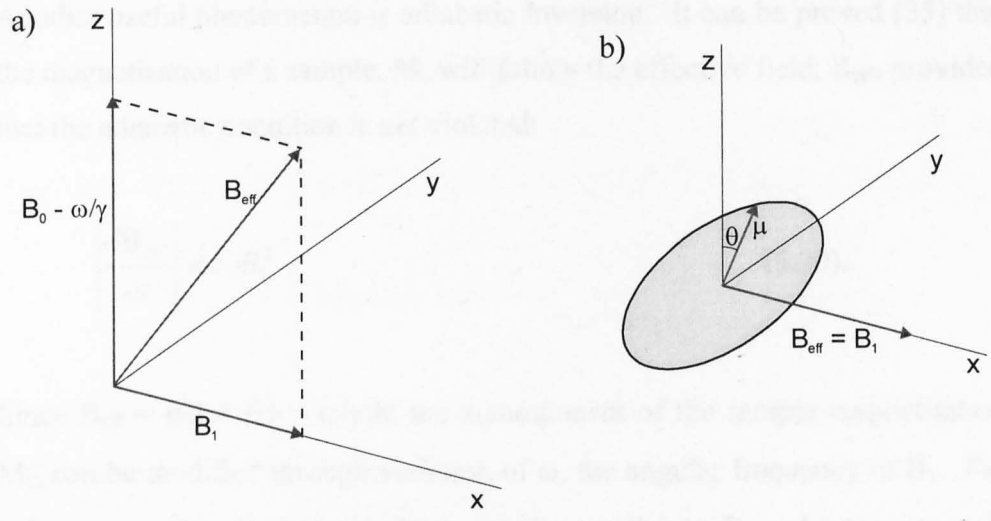

Figure 5.16 *a) Effective field in a rotating frame of reference, rotating with angular velocity ω. b) Precession of magnetic moment, μ, at resonance. $B_0 - \omega/\gamma = 0$, so $B_{eff} = B_1$. Moment precesses around the x-axis, in the y-z plane at a rate γB_1.*

Since the magnetisation of a sample is the sum of its constituent magnetic moments, as discussed earlier, **M** will also precess around $\mathbf{B_0}$. This can be utilised to observe magnetic resonance. If a B_1 pulse of length t_w, chosen such that $\theta = \pi/2$ after application (referred to as a $\pi/2$ pulse), the magnetisation of the sample will precess in the x-y plane, perpendicular to B_0.

If a sample is located in the centre of a coil aligned perpendicular to B_0, such an alternating field (B_1) can be applied to the sample. After a $\pi/2$ pulse, the precession of **M** will result in an induced emf in the coil, which can subsequently be measured.

It was discussed earlier that the population difference in a sample relaxes back to equilibrium after a perturbation, with a characteristic time T_1. The result of this is that **M** also relaxes back to an equilibrium value with the same characteristic time. So, after a $\pi/2$ pulse, **M** initially precesses around B_0 in the x-y plane, but relaxation causes θ to decrease. M_x, the component of magnetisation inducing an emf in the coil, decays with θ, resulting in a decaying signal in the coil. The NMR signal measured in this way is termed the free induction decay.

Another useful phenomenon is adiabatic inversion. It can be proved [35] that the magnetisation of a sample, **M**, will follow the effective field, $\mathbf{B}_{eff}$, provided that the adiabatic condition is not violated:

$$\left|\frac{d\mathbf{B}_{eff}}{dt}\right| << \gamma B_1^2 \qquad (5.20)$$

Since $\mathbf{B}_{eff} = B_1\mathbf{i} + (B_0 - \omega/\gamma)\mathbf{k}$, the z component of the sample magnetisation M_z, can be modified through variation of ω, the angular frequency of B_1. Far below resonance ($\omega << \omega_0$), **M** is nearly parallel to B_0. As resonance is approached, **M** rotates towards the x-axis, and M_z decreases. At resonance $M_z = 0$, and **M** lies perpendicular to $\mathbf{B}_0$. Continuing through resonance causes M_z to become negative, until it is nearly antiparallel to $\mathbf{B}_0$ far above resonance.

Now consider a mechanical oscillator such as a microfabricated cantilever with a magnetic particle attached to the end, positioned close to the sample as shown in figure 5.17. This is the arrangement in a MRFM. The cantilever experiences a force caused by the interaction of the field gradient around the magnetic particle with the magnetisation of the sample. The force, **F**(t) is given by:

$$\mathbf{F}(t) = \nabla[\mathbf{M}(t)\cdot\mathbf{B}] \qquad (5.21)$$

Where **M**(t) is the time-varying magnetisation of the sample, and **B** is the total magnetic field from $\mathbf{B}_0$, $\mathbf{B}_1$ and the magnetic particle. The orientation of the cantilever means that only the z component of the force is significant. Therefore equation 5.21 can be simplified to:

$$F_z(t) = \frac{\partial}{\partial z}[M_z(t)B_z] \qquad (5.22)$$

The cantilever can be resonantly driven, if M_z is modulated periodically at the cantilever resonant frequency, ω_c. Such an excitation causes an oscillation of

the cantilever of amplitude A = FQ/k, where F is the driving force, Q is the quality factor and k is the spring constant of the cantilever. This can be achieved by a number of techniques, including adiabatic inversion. If ω_1, the frequency of the applied magnetic field, is frequency modulated such that:

$$\omega_1(t) = \omega_0 + \Delta\omega(t), \text{ where } \Delta\omega(t) = \Omega \sin(\omega_c t) \qquad (5.23)$$

where $\omega_0 = \gamma B_0$ and Ω is the modulation depth. The effective field now becomes:

$$\mathbf{B_{eff}}(t) = B_1\mathbf{i} + [\Delta\omega(t)/\gamma]\mathbf{k} \qquad (5.24)$$

The sample magnetisation, **M**, follows $\mathbf{B_{eff}}$ provided the adiabatic condition (equation 5.20) is satisfied, resulting in a periodic force on the cantilever at a frequency, ω_0, and therefore an excitation of the cantilever.

The discussion above explains the source of a MRFM signal, however it does not show how a map of nuclear spins can be created. The spatial resolution of MRFM is a result of the field gradient surrounding the magnetic particle. The magnetic field at the sample is now a sum of $\mathbf{B_0}$ and the field from the magnetic particle, which varies with position. So different locations within the sample experience different magnetic fields, and therefore precess at different rates. The resonance condition ($\omega = \gamma B_0$) is only satisfied for thin *slices* within the sample, as shown in figure 5.18. This is analogous to the applied field gradients in MRI, however the gradient from a magnetic particle generally produces parabolic slices, rather than the planar slices in MRI.

The location of the resonant slice is determined by the location of the magnetic particle, and the applied RF frequency, ω_1. Therefore, variation of ω combined with SPM scanning techniques to vary the position of the magnetic particle relative to the sample can produce a NMR signal from many different slices through the sample. Deconvolution of the data results in a three-dimensional map of spins.

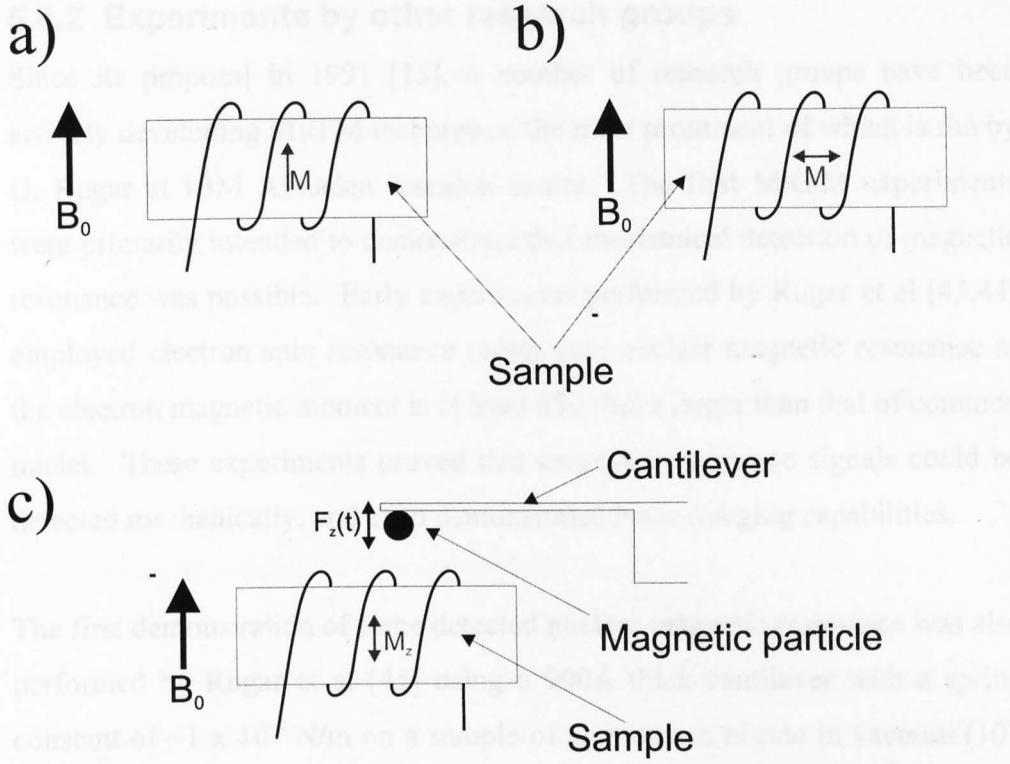

Figure 5.17 *Comparison of conventional NMR detection and MRFM. a) Conventional NMR arrangement. RF coil used for excitation and signal detection. b) After excitation, free inductive decay measured with coil. c) MRFM arrangement. Spins excited with RF coil, signal detected as motion of cantilever caused by spins interacting with field gradient.*

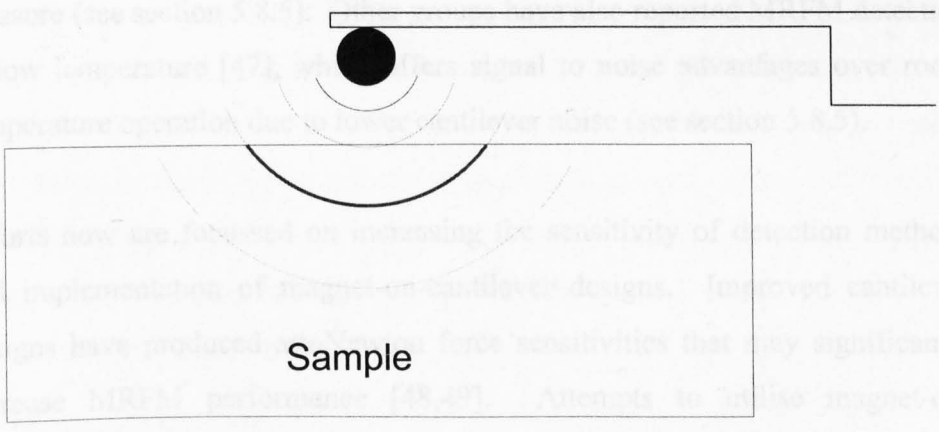

Figure 5.18 *Slices of excitation within a MRFM sample. The curved lines represent surfaces of constant field, and the slice on resonance is highlighted in red.*

5.8.2 Experiments by other research groups

Since its proposal in 1991 [15], a number of research groups have been actively developing MRFM techniques, the most prominent of which is run by D. Rugar at IBM Almaden research centre. The first MRFM experiments were primarily intended to demonstrate that mechanical detection of magnetic resonance was possible. Early experiments performed by Rugar et al [43,44] employed electron spin resonance rather than nuclear magnetic resonance as the electron magnetic moment is at least 650 times larger than that of common nuclei. These experiments proved that magnetic resonance signals could be detected mechanically, and even demonstrated basic imaging capabilities.

The first demonstration of force detected nuclear magnetic resonance was also performed by Rugar et al [45] using a 900Å thick cantilever with a spring constant of ~1 x 10^{-3} N/m on a sample of ammonium nitrate in vacuum (10^{-3} Torr). Even this first experiment produced a spatial resolution nearly an order of magnitude better than conventional magnetic resonance imaging techniques.

More recently, Schaff and Veeman demonstrated that it was possible to detect an NMR signal at atmospheric pressure [46] – a significant achievement, as cantilever Q is typically several orders of magnitude smaller at atmospheric pressure (see section 5.8.5). Other groups have also reported MRFM detection at low temperature [47], which offers signal to noise advantages over room temperature operation due to lower cantilever noise (see section 5.8.5).

Efforts now are focussed on increasing the sensitivity of detection methods and implementation of magnet-on-cantilever designs. Improved cantilever designs have produced attoNewton force sensitivities that may significantly increase MRFM performance [48,49]. Attempts to utilise magnet-on-cantilever designs have encountered problems with parasitic coupling of the magnet to the RF signal [50,51,52]. Novel modulation techniques have been implemented to reduce this coupling, in which both the RF signal and the magnetic field are modulated [41,51].

The sensitivity of MRFM apparatus is clearly improving, as a recent paper by Bruland et al [52] demonstrates. In their experiments, a micron-sized particle was mounted on a cantilever, generating a 250,000 T/m field gradient. Electron spin resonance experiments were performed on a sample of DPPH, with a sensitivity of less than 200 electron moments and a slice thickness estimated to be ~10Å. Although parasitic coupling was observed between the RF signal and the cantilever, it was opposite in phase to the MRFM signal and could therefore distinguished from the measured signal.

The experiments described above show that MRFM is a feasible new imaging technique that is developing rapidly. In the following sections a description of how the SPM head described earlier has been modified to incorporate MRFM functionality is presented. Experiments designed to test the operation of the MFRM components and to determine the likelihood of success are also given.

5.8.3 Configuration of SPM head

In order to function as a MRFM, the SPM head described in previous sections was modified as shown by the photograph in figure 5.19. Stage 1 was used to position the optical fibre as described for AFM operation. A connection to the RF coil (tuned to 300MHz) mounted on stage 2 was made using the 50Ω coaxial cable used in STM mode to carry the tunnel current. The coil had a radius of 0.57mm and 2 turns. A cantilever with sample attached to the end (see next section) was mounted on the removable cantilever holder in such a way that when the holder was inserted on stage 2, the end of the cantilever was located ~100μm from the RF coil. Stage 3 was used to position a 0.25mm diameter Fe wire mounted in a stainless steel tip nut, in a similar manner to the PtIr STM tip described previously.

The optical fibre was positioned <4μm from the cantilever surface (it is shown further away in figure 5.19 for clarity), and as close to the end of the cantilever as possible. The end of the magnetic Fe wire was cut flat and perpendicular to its length to produce a well-defined cylindrical shape. This flat surface was

positioned <100μm away from the sample (mounted on the end of the cantilever). Overall, no major modifications were required to change the SPM head to an arrangement suitable for MRFM experiments, proving that it is extremely versatile.

5.8.4 Sample preparation

Unlike AFM, in most MRFM experiments the sample has been mounted on the cantilever. This is not an essential aspect of MRFM, the fundamental physics is equally applicable to a magnetic particle attached to a cantilever, but experiments have shown this to produce spurious excitation of the cantilever (as discussed in section 5.8.2) [38]. In addition, at this early stage of development of our MRFM, a magnetic particle small enough to be mounted on a cantilever would not excite a large enough volume in the sample to produce a measurable signal. So the sample was mounted on the cantilever for all MRFM experiments described here.

A sample of ammonium nitrate was chosen because of its abundance of protons (5.1×10^{28} per m^3) and suitable NMR relaxation times. It occurs in a crystalline form at room temperature and pressure, and is dissolved easily in water. In order to attach a sample of ammonium nitrate to a cantilever with dimensions 450μm x 50μm x 2μm [39], the crystals were ground into a fine powder. With the aid of an optical microscope, a suitable grain of ammonium nitrate with dimensions of ~50μm was selected using a fine piece of wire.

The cantilever was then prepared by touching a wire coated in two-part quick-dry epoxy onto its underside near the end. Positioning the cantilever under an optical microscope and resting the wire on a support close to the cantilever stabilised the wire and allowed enough control to prevent damage to the cantilever. The process was then immediately repeated with the chosen grain of ammonium nitrate. The combination of sample and cantilever was then left to dry for several hours before use. Figure 5.20 shows a typical sample mounted on a cantilever.

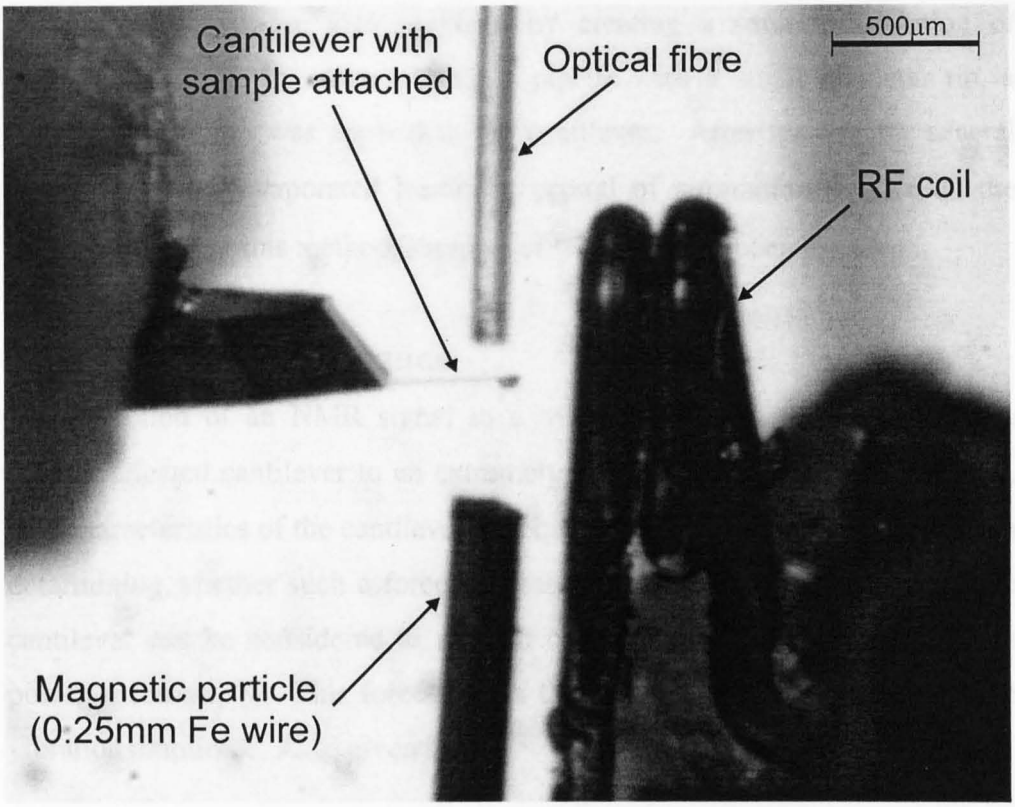

Figure 5.19 *Photograph of MRFM apparatus. Picture acquired by capturing the output from the CCD camera used for alignment of fibre and magnet.*

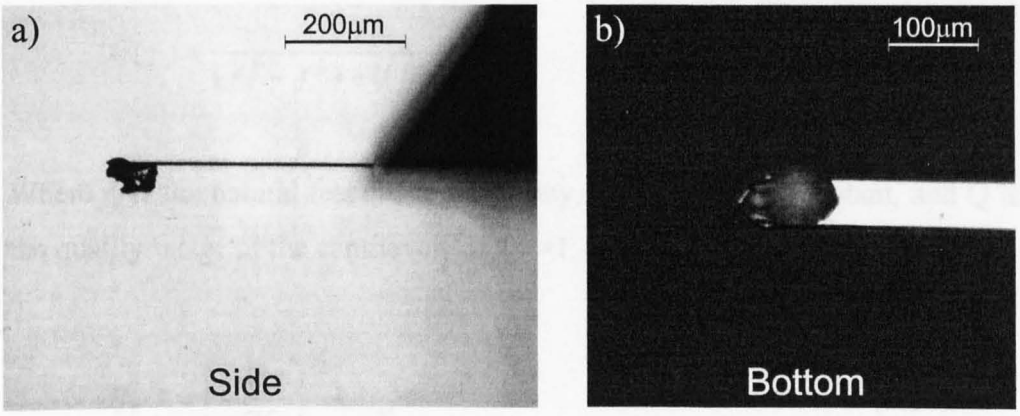

Figure 5.20 *Magnified view of cantilever with ammonium nitrate sample attached.*

Smaller samples were also prepared by creating a saturated solution of ammonium nitrate in water. Using a pipette with a small diameter tip, a droplet of solution was applied to the cantilever. After leaving for several hours, the water evaporated leaving a crystal of ammonium nitrate on the cantilever. Using this method, samples of $<10\mu m^3$ have been produced.

5.8.5 Cantilever resonance

The detection of an NMR signal in a MRFM relies on the response of a microfabricated cantilever to an extremely small ($<10^{-15}$ N) oscillatory force. The characteristics of the cantilever's frequency response are a major factor in determining whether such a force is measurable. The thermal motion of the cantilever can be considered as a result of a random force, F(t), with a flat power spectrum, S_F. This force excites the cantilever to a root mean square vibration amplitude, A_{rms}, given by

$$A_{rms}^2 = \int_0^\infty S_F |G(f)|^2 df \tag{5.25}$$

Where *G(f)* is the transfer function of the cantilever. If modelled as a simple harmonic oscillator, *G(f)* is:

$$G(f) = \frac{f_0^2 / k}{(f_0^2 - f^2) + i(ff_0 / Q)} \tag{5.26}$$

Where f_0 is the natural resonance frequency, k is the spring constant, and Q is the quality factor of the cantilever. If Q>>1, then equation 5.25 becomes

$$S_F{}^{1/2} = \left(\frac{2}{\pi Q f_0}\right)^{1/2} kA_{rms} \tag{5.27}$$

Note that $S_F{}^{1/2}$ has units of $N/\sqrt{Hz}$. The equipartition theorem predicts that the energy per degree of freedom of the system is $1/2k_BT$ at thermal equilibrium, so with only one degree of freedom $A_{rms}=(k_BT/k)^{1/2}$. This gives

$$S_F^{1/2} = \left(\frac{2kk_B T}{\pi Q f_0} \right)^{1/2} \tag{5.28}$$

Where k_B is Boltzmann's constant, and T is the temperature.

In a measurement bandwidth $\Delta\nu$, the minimum detectable force (corresponding to a signal to noise ratio of 1) is $F_{min} = (S_F \Delta\nu)^{1/2}$, or:

$$F_{\min} = \left(\frac{2kk_B T \Delta \nu}{\pi Q f_0} \right)^{\frac{1}{2}} \tag{5.29}$$

It is clear from equation 5.29 that the physical properties of the cantilever (Q, k, and f_0) are the main parameters that determine the minimum detectable force.

Data provided with the cantilever used in our experiments [39] gave its spring constant as typically in the range 0.07-0.4 N/m. The cantilever Q and resonant frequency were determined experimentally by driving the cantilever with a sinusoidal signal applied to a piezoelectric plate. The amplitude of oscillation of an unloaded cantilever was monitored with a lock-in amplifier for a sequence of frequencies. A clear peak was observed in the frequency versus excitation amplitude graph at ~15kHz, as shown in figure 5.20. This peak shifted down when a sample was attached to the cantilever to a frequency determined by the mass of the sample (typically ~7kHz).

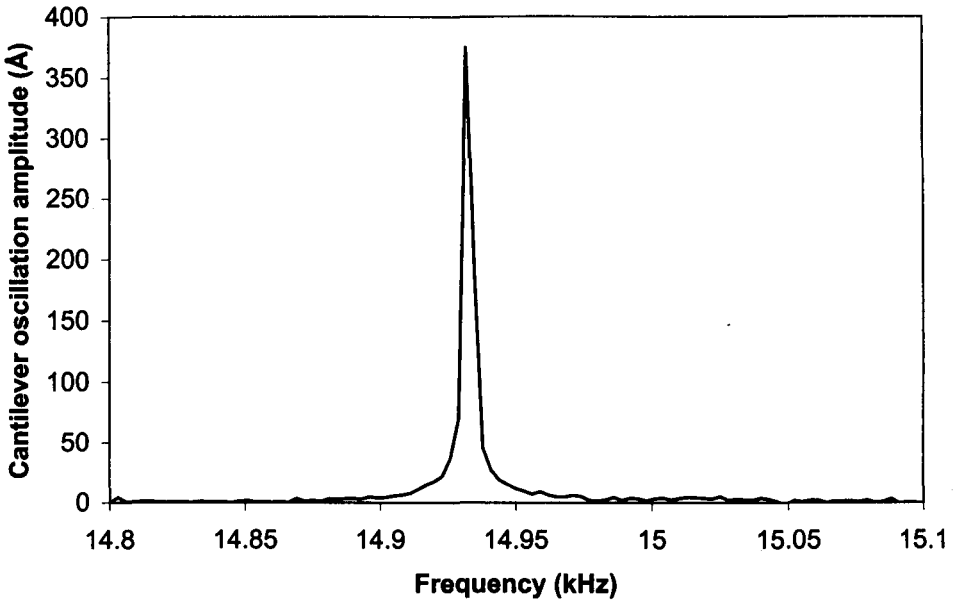

Figure 5.20 *Resonance curve for an unloaded cantilever*

The Q of the cantilever was calculated as the central frequency of the observed peak divided by the width of the peak at $1/\sqrt{2}$ of the maximum amplitude. Values of ~30 were observed in air, which increased to ~20000 at a pressure, P = ~0.05mbar. It was found that Q was approximately proportional to $1/P^{½}$, as shown by the ln Q versus ln P graph in figure 5.21. A reported Q of an identical cantilever at a pressure of $\sim 10^{-5}$mbar was 4×10^5 [40]. This value does not exactly fit the observed relationship, but the discrepancy could be due to inaccurate measurement of P. It could also be an indication that the relationship breaks down at lower pressures due to a physical limit of the cantilever. However, it is clear that a decrease in pressure significantly increases the quality factor of a cantilever, and therefore its force sensitivity (from equation 5.26).

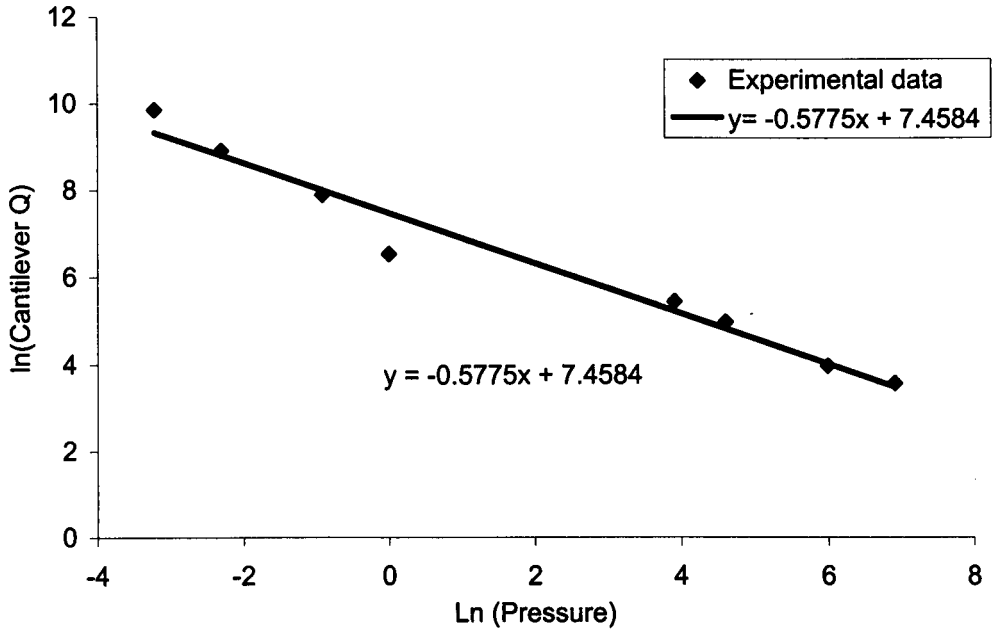

Figure 5.21 *Graph showing dependence of cantilever Q with pressure*

The spring constant of a cantilever can be estimated using $k = k_B T/(A_{rms})^2$, where A_{rms} is the root mean square amplitude of the thermal vibration [48]. Using a lock-in amplifier with a time-constant of 100ms (Δv=2.5Hz), the vibration amplitude of the cantilever was recorded for frequencies around the cantilever resonance frequency. The results are shown in figure 5.22. A clear increase in vibration amplitude up to a maximum value of ~16Å is observed at the resonance frequency. Since the transfer function of the cantilever results in the majority of noise concentrated around the cantilever resonance, integration of figure 5.22 should give a reasonable estimate of A_{rms}. Taking the measurement bandwidth into account, A_{rms} was found to be ~23Å, giving k <0.001N/m, well below the specified range of the cantilever. This discrepancy is most likely to be due to some external vibration source, as observed by other groups [47]. Therefore the minimum detectable force is limited by this vibrational noise. Assuming k ~0.1 N/m, and Q ~2000 (estimated from figure 5.22), the vibration-limited force limit is 5.0×10^{-14} $N/\sqrt{Hz}$. This is approximately an order of magnitude greater than the thermally limited force of 4.3×10^{-15} $N/\sqrt{Hz}$, given by equation 5.29.

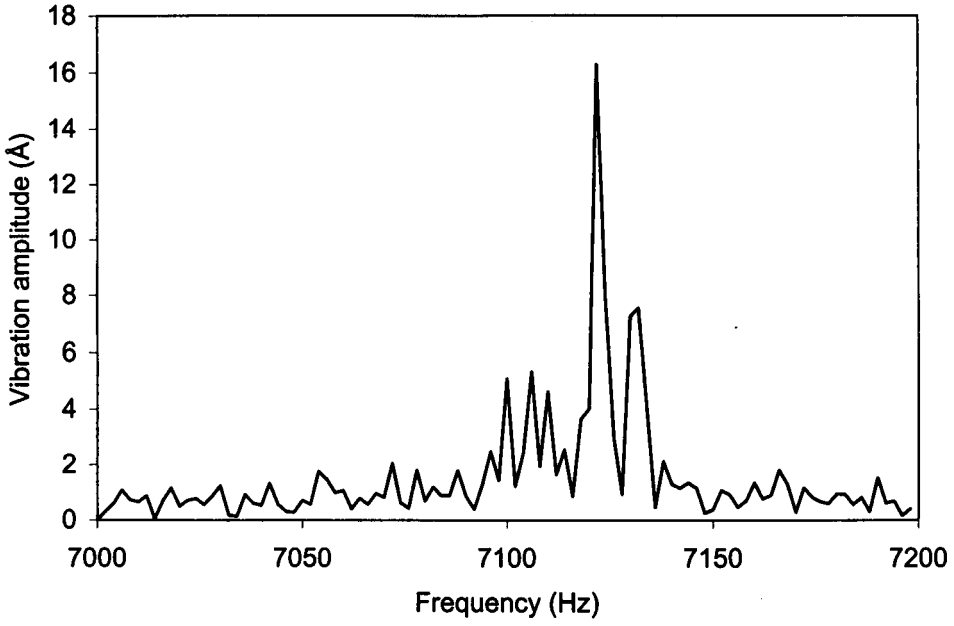

Figure 5.22 *Noise spectrum of a cantilever with sample attached. Measurement bandwidth $\Delta\nu$=2.5Hz*

5.8.6 Direct mechanical coupling of RF

It was mentioned in section 5.8.2 that several groups had observed parasitic coupling of the modulated RF signal to the cantilever when mounted with a magnetic particle. It has also been observed that similar coupling can occur with the sample on the cantilever [161,162], and is commonly large enough to completely obscure the desired NMR signal. Such coupling has been observed in our MRFM system, causing cantilever vibration amplitudes over 100Å in some circumstances.

An attempt to characterise this noise source has been made, by investigating its dependence on RF power, modulation type and depth, RF frequency, and static magnetic field strength. It was found that excitation amplitude was approximately linear in both RF power and frequency modulation depth. It was also ~5x larger for amplitude modulation compared to frequency modulation. These observations are in agreement with those observed by other groups [51,41].

It has been suggested that this modulation noise can be ignored to a certain extent, as it is constant throughout a MRFM experiment [52]. Any additional signal caused by NMR will result in changes to the observed excitation amplitude. Since the phase of the modulation noise is generally different to that of the MRFM signal, the two can be distinguished from each other using a lock-in amplifier. However, an anharmonic modulation technique has been proposed that completely removes modulation noise [41,51]. To avoid direct excitation of the cantilever, both B_0 and the RF signal (B_1) are modulated at anharmonic fractions of the cantilever resonance frequency such that $f_c=f_0+/-f_1$ where f_c is the cantilever resonance frequency, and f_0 and f_1 are the modulation frequencies of B_0 and B_1 respectively. The induced magnetisation of the sample contains a component at f_c, resulting in excitation of the cantilever. So far this technique has only been applied to electron spin resonance, but the principle is equally applicable to NMR.

5.8.7 Measurement of B_1

Knowledge of the RF magnetic field, B_1, is important when estimating the level of signal expected from a MRFM experiment. It determines the useable level of modulation without breaking the adiabatic condition $|dB_{eff}/dt| << \gamma B_1^2$, as discussed in section 5.8.1.

Recent experiments by a summer student in our group have used a conventional NMR arrangement to measure B_1. A sample of glycerol was inserted into the RF coil and basic free induction decay measurements were performed to determine the value of B_1. For a power of 500mW, the field at the centre of the coil was 3mT. This gives the B_1 field at the cantilever to be ~0.3mT.

5.8.8 Feasibility of MRFM operation

The feasibility of operating the SPM in MRFM mode will now be discussed. Using the experimentally determined properties of the system, a value for the expected signal level can be obtained. If this level is within the detectable

limits of the interferometer it can be concluded that it should be possible to detect an NMR signal with the current arrangement.

The force exerted on the cantilever is given by $F_z(t) = M_z(t)\delta B_z/\delta z$, where M_z is the magnetisation of the sample in the z direction (i.e. parallel to B_0) and $\delta B_z/\delta z$ is the field gradient created by the magnetic particle. The cyclic adiabatic modulation scheme causes the magnetisation to vary according to $M_z = AM_z(0)\cos(\omega_c t)$ where A is a constant 1, $M_z(0)$ is the equilibrium magnetisation of the sample, given by the Curie law:

$$M_z(0) = \frac{n\mu_p{}^2 B_z}{2k_B T} \qquad (5.27)$$

where n is the number of protons, μ_p is the proton magnetic moment, and B_z is the field in the z direction. Therefore the maximum root mean square value of M_z is $M_z(0)/\sqrt{2}$.

The largest signal will be obtained when the entire sample (50 x 50 x 50 μm^3) is excited. This gives an rms value of M_z of 1.3 x 10^{-15} J/T for a 7.2T field in z (7T from superconducting magnet, 0.2T from magnetic particle). In order to excite the entire sample, the effective line width and field gradient must produce an actual width of ~50μm. For a B_1 of 0.3mT, a modulation depth,Ω, of ~2π x 100kHz is suitable to ensure the adiabatic condition is satisfied. This results in an effective linewidth of $\sim 2\Omega/\gamma$ = 4.6mT. Therefore, to excite the entire sample, the field gradient, $\delta B_z/\delta z$, must be ≤ 100T/m.

The resulting rms force, F_z is 1.1 x 10^{-13}N, similar to that observed elsewhere [47,45]. Such a signal level compares favourably with the vibration-limited minimum force, giving a signal to noise ratio of ~2 in a 1Hz bandwidth, and a ratio of 20 if thermally limited. These calculations show that the current arrangement for MRFM experiments should allow mechanical detection of an

NMR signal with a signal to noise ratio of at least 2 in vacuum when the entire 50 x 50 x 50 μm^3 sample is excited.

5.9 Summary

The SPM system presented in this chapter has been demonstrated to operate in both air and vacuum, and in magnetic fields of zero and 7T. Operation in UHV should also be possible with a suitable pumping arrangement. Two 3-axis inertial sliding motors have been constructed with controllable step sizes up to 1000Å for coarse positioning. An optical fibre based interferometer with a sensitivity of $0.2\,\mathring{A}/\sqrt{Hz}$ has also been developed tip monitor cantilever displacements.

Work towards a fully functioning magnetic resonance force microscope (MRFM) has produced promising results. Future development of the SPM system should focus on improvements to the interferometer sensitivity and measurement bandwidth, operation under UHV conditions, and acquisition of a force detected NMR signal.

5.10 References

1. G. Binnig, H. Rohrer, Ch. Gerber and E. Weibel, Phys. Rev. Lett. **49** 57 (1982)
2. D. W. Pohl (1982)
3. G Binnig, C. F. Quate and Ch. Gerber, Phys. Rev. Lett., **56**, 930 (1986)
4. For example Park Scientific Instruments provide several SFM models capable of a range of SPM techniques.
5. O. Marti, B. Drake and P. K. Hansma, Appl. Phys. Lett. **51** 484 (1987)
6. R. M. Feenstra, W. A. Thompson and A. P. Fein, J. Vac. Sci. Technol. A **4** 1315 (1986)

7. M. H. Jerico, D. C. Dahn and B. L. Blackford, Rev. Sci. Instrum. **58** 1349 (1987)
8. H. J. Mamin, D. W. Abraham, E. Ganz and J. Clark, Rev. Sci. Instrum. **56** 11 (1985)
9. S. Gregory and C. T. Rogers, J. Vac. Sci. Technol. A **6** 390 (1988)
10. D. W. Pohl, Rev. Sci. Instrum. **58** 54 (1987)
11. Ph. Niederman, R. Emch and P. Descouts, Rev. Sci. Instrum. **59** 368 (1988)
12. J. W. Lyding, S. Skala, J. S. Hubacek, R. Brockenbrough and G. Gammie, Rev. Sci. Instrum. **59** 1897 (1988)
13. C. N. Woodburn, A. W. McKinnon, D. A. Roberts, M. E. Taylor and M. E. Welland, Meas. Sci. Technol. **4** 535 (1993)
14. S. Kleindiek, H. S. Kim, E. Kratschmer and T. H. P. Chang, J. Vac. Sci. Technol. B **13** 2653 (1995)
15. J. A. Sidles, Appl. Phys. Lett., **58**, 2854 (1991)
16. Epotek provide a range of UHV compatible epoxies that require baking to cure. Both conducting and non-conducting products are available.
17. G. Binnig, C. F. Quate, Ch. Gerber, Phys. Rev. Lett., **56**, 930 (1986)
18. G. Meyer and N. M. Amer, Appl. Phys. Lett., **53**, 1045 (1988)
19. Y. Martin, C. C. Williams and H. K. Wickramasinghe, J. Appl. Phys., **61**, 4723 (1987)
20. R. Erlandsson, G. M. McClelland, C. M. Mate, S. Chiang, J. Vac. Sci. Technol. A, **6**, 266 (1988)
21. D. Rugar, H. J. Mamin, R. Erlandsson, J. E. Stern and B. D. Terris, Rev. Sci. Instrum., **59**, 2337 (1988)
22. D. Rugar, H. J. Mamin and P. Guethner, Appl. Phys. Lett., **55**, 2588 (1989)
23. D. Rugar, O. Züger, S. Hoen, C. S. Yannoni, H.-M. Vieth, R. D. Kendrick, Science, **264**, 1560 (1994)
24. B. Kracke and B. Damaschke, Rev. Sci. Instrum., **67**, 2957 (1996)
25. A. Moser, H. J. Hug, Th. Jung, U. D. Schwarz and H-J. Güntherodt, Meas. Sci. Technol., **4**, 769 (1993)

26. M. D. R. Taylor and P. Moriarty, use an optical fibre feedthrough constructed in-house similar to that described in the text in a photon emission STM system.
27. Topometrix contact mode cantilever, for use in their "Explorer" AFM.
28. Al grain sample provided as a test sample with the Topometrix "Explorer" AFM.
29. Gold sample kindly prepared by M. Taylor.
30. E. M. Purcell, H. C. Torrey and R. V. Pound, Phys. Rev., **69**, 37 (1946)
31. F. Bloch, W. W. Hansen and M. E. Packard, Phys. Rev., **69**, 127 (1946)
32. P. C. Lauterbur, Nature, **242**, 190 (1973)
33. P. Mansfield, P. K. Grannell, J. Phys. **C 6**, L422 (1973)
34. P. M. Glover, R. W. Bowtell, G. D. Brown, P. Mansfield, Mag. Res. Med., **31**, 423 (1994)
35. C. P. Slichter "Principles of magnetic resonance" 3rd Edition Springer-Verlag publishing (1990)
36. J. A. Sidles, Appl. Phys. Lett., **58**, 2854 (1991)
37. J. A. Sidles, J. L. Garbini, K. J. Bruland, D. Rugar, O. Züger, S. Hoen and C. S. Yannoni, Rev. Mod. Phys. **67**, 249 (1995)
38. Z. Zhang, P. C. Hammel, P. E. Wigen, Appl. Phys. Lett., **68**, 2005
39. Nanosensors tipless single crystal Si contact mode AFM cantilever, purchased through Park Scientific Instruments.
40. K. Wago, O. Züger, R. Kendrick and D. Rugar, J. Vac. Sci. Technol. B., **14**, 1197 (1996)
41. K. J. Bruland, J. Krzystek, J. L. Garbini, J. A. Sidles, Rev. Sci. Instrum., **66**, 2853 (1995)
42. M. Binggeli, G. Kotrotsios, R. Christoph and H. E. Hintermann, Rev. Sci. Instrum., **64**, 2888 (1993)
43. D. Rugar, C. S. Yannoni, and J. A. Sidles, Nature, **360**, 563 (1992)
44. O. Züger and D. Rugar, Appl. Phys. Lett., **63**, 2496 (1993)
45. D. Rugar, O. Züger, S. Hoen, C. S. Yannoni, H.-M. Vieth, R. D. Kendrick, Science, **264**, 1560 (1994)
46. A. Schaff and W. S. Veeman, Appl. Phys. Lett., **70**, 2598 (1997)
47. K. Wago, O. Züger, R. Kendrick, C. S. Yannoni and D. Rugar, J. Vac. Sci. Technol. B, **14**, 1197 (1996)

48. T. D. Stowe, K. Yasumura, T. W. Kenny, D. Botkin, K. Wago and D. Rugar, App. Phys. Lett. **71**, 288 (1997)
49. P. Streckeisen, S. Rast, C. Wattinger, E. Meyer, P. Vettiger, Ch. Gerber, H.-J. Güntherodt, Appl. Phys. A., **66**, S341 (1998)
50. Z. Zhang and P. C. Hammel, IEEE Transactions on magnetics, **33**, 4047 (1997)
51. J. A. Marohn, R. Fainchtein, D. D. Smith, J. Appl. Phys., **86**, 4619 (1999)
52. K. J. Bruland, W. M. Dougherty, J. L. Garbini, J. A. Sidles and S. H. Chao, Appl. Phys. Lett., **73**, 3159 (1998)